EXPERIMENTAL STUDIES ON THERMAL BEHAVIOR OF 6T CRYOGEN-FREE SUPERCONDUCTING MAGNET SYSTEM

Thesis submitted in partial fulfillment of the requirements for the degree of

Master of Technology (M.Tech.)

in

MECHANICAL ENGINEERING

(Cryogenic & Vacuum Technology)

by

Vijay Kumar Soni

Roll No. 213ME5458

Under the guidance of

Prof. Sunil Kumar Sarangi

NIT, Rourkela

Mr. Soumen Kar

IUAC, New Delhi

Department of Mechanical Engineering

National Institute of Technology, Rourkela

May, 2015

National Institute of Technology, Rourkela

Department of Mechanical Engineering

Certificate

This is to certify that the thesis entitled "**Experimental studies on thermal behavior of 6T cryogen-free superconducting magnet system**", being submitted by Shri Vijay Kumar Soni, for the award of the degree of Master of Technology in Mechanical Engineering, is a record of bonafide research carried out by him. Mr. Vijay Kumar Soni has worked for a year on the above mentioned problem at the Department of Mechanical Engineering, National Institute of Technology, Rourkela and Cryogenic and Applied Superconductivity Group, Inter University Accelerator Center, New Delhi, under our guidance and supervision. This work has reached the standard fulfilling the requirements and the regulation relating to the degree. The work incorporated in this thesis has not been, to the best of our knowledge submitted to any other University or Institution for the award of any degree or diploma.

Prof. Sunil Kumar Sarangi
Director
NIT, Rourkela
Date-

Mr. Soumen Kar
Scientist-F
IUAC, New Delhi
Date-

CONTENTS

CERTIFICATE I

CONTENTS II

ACKNOWLEDGEMENT IV

ABSTRACT V

LIST OF FIGURES VI

LIST OF TABLES X

1. INTRODUCTION **1**

2. LITERATURE REVIEW **4**

3. 6T CONDUCTION COOLED NbTi SOLENOID MAGNET SYSTEM **6**

3.1. Introduction 7

3.1.1. Components of the 6T cryogen free superconducting magnet system 7

3.2. Design of the NbTi solenoid magnet 8

3.3. NbTi superconductor characteristics 14

3.4. Current sharing temperature and temperature margin 15

3.5. Operating load line curve for 6T NbTi solenoid magnet 17

3.6. Thermal load curves for GM cryocooler 20

3.7. Finite element magnetostatic analysis 22

3.8. 6T solenoid magnet operation 25

4. CONDUCTION COOLED HYBRID CURRENT LEAD **27**

4.1. Introduction 28

4.1.1. Types of current leads 28

4.2. Optimization of metallic/ alloy current lead 32

4.3. Thermal impedance measurement of inter-lead joint of hybrid lead 36

4.3.1. Test of thermal properties at the joint with different interlayer material 37

4.3.2. Measurement and analysis 41

4.4. ANSYS heat flow analysis of hybrid current lead 44

4.4.1. Thermal profile of the optimized phosphor de-oxidized copper current lead 44

5. QUENCH ANALYSIS OF 6T CONDUCTION COOLED NbTi MAGNET **50**

5.1. Introduction 51

5.2. Temperature and current margin for quench 53

5.3. Classification of quench 54

5.4. Causes of quench 55

5.4.1. Mechanical events 55

5.4.2. Electromagnetic events 56
5.4.3. Thermal events 56
5.4.4. Concept of minimum propagating zone (MPZ) 57
5.5. Quench protection 57
5.5.1. External dump resistor 57
5.6. Finite element quench analysis using OPERA 58
5.6.1. Definition 58
5.6.2. Physical model 59
5.6.3. Material property data 61
5.6.1. Boundary conditions and protection circuit 63
5.6.2. Quench simulation environment 64
5.6.3. QUENCH program post processor, results and discussion 65
5.6.4. Quench Simulation 70
5.7. Experimental quench study of 6T NbTi solenoid magnet 78
5.7.1. Experimental results of quench for 6T NbTi solenoid magnet 79

6. VARIABLE TEMPERATURE INSERT FOR 6T CFMS 80
6.1. Introduction 81
6.1.1. Types of the variable temperature inserts (VTI) 81
6.2. VTI using gas gap heat switch 82
6.2.1. Gas gap heat switch (GGHS) 82
6.2.2. Solid and gas conduction 84
6.2.3. Heat flow mechanism for the GGHS 85
6.2.4. Testing of GGHS in Cryogen Free Superconducting Magnet System 86

7. CONCLUSION 92

REFERENCES 94

Acknowledgement

In every good work there are so many minds behind the screen, for that I would like to pay their credits forever. First, I am grateful to Dr. D. Kanjilal (Director, IUAC), who has given me the permission to carry out the project work at IUAC. I would like to express my deep sense of respect and gratitude to my supervisors Mr. Soumen Kar (Scientist-F, IUAC) and Prof. Sunil Kumar Sarangi (Director, NIT Rourkela) for their excellent guidance, intelligent suggestions and endless efforts which leads to my successful project work. I consider myself extremely lucky working under guidance of such a dynamic, laborious and genius personalities.

I would also express my sincere gratitude to Dr. R.G. Sharma (Ex. NPL), Dr. T. S. Datta (Scientist-H), Prof. R. K. Sahoo (NITR) and Dr. Anup Choudhury (Scientist-F) for their continuous encouragement, support and understanding, without which, this project work would not have been possible.

I record my deepest gratitude to Mr. Manoj Kumar (JE), Mr. Rajesh Kumar (Engineer-E), Mr. Suresh Babu (JE), Mr. Phaneendra Konduru (PhD scholar) and Mr. Santosh Sahu (Engineer-C) for their valuable suggestions and encouragement for the accomplishment of my project work.

I also owe to the technical assistant staff of cryogenic group, IUAC for their constant working efforts. I would like thanks to all my friends and well-wishers.

Vijay Kumar Soni

Roll No- 213ME5458

Abstract

The main aim of this thesis is to report very comprehensive studies and analysis that I have carried out on different thermal aspects of a 6T Cryogen-free Superconducting Magnet System (CFMS) which is designed and built at IUAC. One of important parameter for any superconducting magnet is to achieve the desired field homogeneity by choosing proper dimensional parameter. The role dimensional parameters for the 6T NbTi magnet have been studied to achieve 0.07% field homogeneity at 10mm diametrical spherical volume at the magnetic center. The stability of the 6T NbTi magnet is greatly dependent by its operational margin which is determined by the current sharing temperature of the NbTi. The role of the operational load line has been discussed in determining the stability of the 6T NbTi magnet. The current sharing temperature of the 6T magnet has also been estimated. Two stage GM cryocooler is one of the critical components of the CFMS. The refrigeration load curves for both stages of SRDK-415 GM cryocooler have been generated in a cryocooler based test rig. The refrigeration load curves for the 1^{st} stage of the cryocooler have been generated between 25K and 65K with 0-1.5W of load at the 2^{nd} stage of the cryocooler. Similarly, the refrigeration load curves for the 2^{nd} stage have been generated between 2.4K and 4.4K with 0-47.5W load at 1^{st} stage of the cryocooler. The magnetic field profile for 6T solenoid magnet has been generated with the use of finite element magnetostatic simulation software (OPERA/TOSCA). Hybrid current lead is one of the crucial components of the CFMS. Thermal performance of inter-lead joint between hybrid lead and cold heads of the cryocooler plays a significant role in determining the stability of the NbTi magnet in the CFMS. A prototype lead joint has been characterized in the temperature range of 4-40K in a test rig with different interfacial material (Aluminium nitride/ Kapton) to achieve thermally conducting and electrically isolated joint. The extensive FEM analysis has also done using ANSYS for different types of conduction-cooled leads, optimized for 102A. Quenching is one of the important phenomenon for a superconducting magnet. The protection system for a superconducting magnet needs to be designed ingeniously. In this report, extensive FEM analysis has been done, using OPERA-3D/QUENCH for the 6T NbTi magnet. The analysis has shown the hot spot temperature of the 6T NbTi magnet would be 65-80K, if quenched at 102A. It has been compared with the experimental result. A detailed comparative studies have been done between different types of quench situation. Variable temperature inserts (VTI) is one of common feature integrated with each commercial CFMS to vary temperature on the sample space. The experimental studies have been performed on the gas gap heat switch (GGHS) integrated with CFMS. The feasibility of using GGHS as VTI has been studied up to 3T magnetic field.

List of Figures

Figure 3.1. Schematic representation of 6T CFMS 8
Figure 3.2. Magnetic field around conductor C 9
Figure 3.3. Schematic representation of Ampere's right hand rule 9
Figure 3.4. Schematic of Solenoid coil 9
Figure 3.5. Current carrying loop of radius a 10
Figure 3.6. Dimensional cross section view of solenoid coil 11
Figure 3.7. Field factor, $F(\alpha, \beta)$ as a function of α and β 12
Figure 3.8. Maximum field B_m v/s β graph for different values of α 13
Figure 3.9. Critical surface of the NbTi superconductor 14
Figure 3.10. (a) Current sharing model for composite superconductor wires, (b) Current distribution in composite superconductor at different temperature regimes 15
Figure 3.11. Load line curve at 4.2K for the 6T conduction cooled magnet 18
Figure 3.12. SRDK-415D GM cryocooler (SHI Cryogenics Group) 19
Figure 3.13. Refrigeration capacity v/s temperature curve for the 2nd stage at different thermal loads on 1st stage 20
Figure 3.14. Refrigeration capacity v/s temperature curve for the 1st stage at different thermal loads on 2nd stage 20
Figure 3.15. Practical load map of SRDK-415D GM cryocooler 21
Figure 3.16. The histogram (a) and plane (b) representation of the magnetic field profile of 6T solenoid magnet 22
Figure 3.17. The line representation of the magnetic field profile of 6T solenoid magnet 22
Figure 3.18. Magnetic field profile of 6T solenoid magnet with in the Coil 23
Figure 3.19. Magnetic field distribution along the X-axis of the solenoid coil i.e. transverse magnetic field 23
Figure 3.20. Magnetic field distribution along the Y-axis of the solenoid coil i.e. axial magnetic field 24
Figure 3.21. Magnetic field distribution along the Y-axis of the solenoid coil for 10mm DSV 24
Figure 3.22. 3-D representation of 10mm radius sphere which resembles DSV 24
Figure 3.23. CFMS cool down curve 25
Figure 3.24. Magnetic field v/s current curve 25
Figure 3.25. Temperature profile of magnet and 2nd stage cooling attachments, during magnet charging 26

Figure 4.1. Thermal conductivity of different metals, alloys and BSCCO (HTS) material 30
Figure 4.2. Electrical resistivity of different metals and alloys 30
Figure 4.3. Heat flow scheme of hybrid current lead system 31
Figure 4.4. 1-dimensional heat flow model for a conduction-cooled current lead 32

Figure 4.5. Shape parameter $\left({}^{IL}/_{A}\right)_{opt}$ of the optimized current leads for the different cold end temperature of the current lead when hot end temperature is fixed at 300K 34
Figure 4.6. The optimized current leads lengths for the different cold end temperature of the current lead when hot end temperature is fixed at 300K at operating current of 102A and 15mm^2 cross section area 35
Figure 4.7. Surface contact irregularities with vacuum voids 36
Figure 4.8. Schematic diagram of test setup 38
Figure 4.9. Block diagram of test setup 39
Figure 4.10. Internal view of test set up 39
Figure 4.11. Thermal anchoring block and base plate (a) Cu-Kapton -Cu joint, (b) Cu-AlN-Cu joint 40
Figure 4.12. Thermal impedance v/s temperature of Cu-Kapton-Cu and Cu-AlN-Cu interface 41
Figure 4.13. Thermal resistance v/s temperature of Cu-Kapton-Cu and Cu-AlN-Cu interface joint 42
Figure 4.14. Thermal resistance v/s temperature of Cu-Kapton-Cu for two different contact area 42
Figure 4.15. Temperature difference (T_{S1}-T_{S2}) v/s heat load of Cu-Kapton-Cu and Cu-AlN-Cu interface at 4K temperature 43
Figure 4.16. Temperature difference (T_{S1}-T_{S2}) v/s heat load of Cu-Kapton-Cu and Cu-AlN-Cu interface at 40K temperature 43
Figure 4.17. Thermal profile of the optimized phosphor de-oxidized copper lead for under-current, optimized current and over-current operation 45
Figure 4.18. ANSYS 3D graphics of optimized current lead operating at under, over and optimized current (a) represent heat flux graphics and (b) represent temperature distribution graphics 47
Figure 4.19. Thermal profile of the current leads made with different materials with respect to their optimized length at operating current (I_{op} = 102A) 48
Figure 4.20. Maximum temperature as a function of over- current for different materials for current lead 49

Figure 5.1. Flow chart of quench 51
Figure 5.2. (a) Burnt HTS current lead of superconducting quadrupole magnet system (IUAC, New Delhi) due to quench. (b) Arcing at the current lead terminals of superconducting quadrupole magnet system (IUAC, New Delhi) due to high voltage during quench 52
Figure 5.3. Temperature margin to quench 53
Figure 5.4. Current margin for quench 54
Figure 5.5. Schematic representation of various types of quench 55

Figure 5.6. A single turn of solenoid magnet with a current density J exposed to the field B of the magnet. The resulting Lorentz force F, is directed outward 55
Figure 5.7. Filaments of superconductor are embedded in matrix of normal metal 56
Figure 5.8. A current carrying conductor heated at small length ℓ 57
Figure 5.9. Magnet coil with parallel external dump resistor 58
Figure 5.10. Back to back diode scheme 58
Figure 5.11. (a) Solenoid conductor dimensions, (b) Circuit element definition with co-ordinate system and advance mesh options, (c) 6T solenoid magnet coil 60
Figure 5.12. Coil model body with symmetry at XY and ZX co-ordinate 61
Figure 5.13. Quench material properties for the conductor 63
Figure 5.14. Quench heat source definition in *OPERA* 63
Figure 5.15. Quench protection circuit -CKT1 64
Figure 5.16. Quench analysis data definition with adaptive time stepping 64
Figure 5.17. Quench analysis database 65
Figure 5.18. Window for the quench result data presentation through graphs 65
Figure 5.19. 3-D representation of growing normal zone 66
Figure 5.20. (a) Temperature rise curve, (b) Resistance growth curve, (c) Current decay curve, (d) Internal voltage curve, (e) Quench volume curve and (f) Joule heating curve 68
Figure 5.21. 3-Dimentional temperature rise graphics of quenched solenoid magnet coil 69
Figure 5.22. Resistance, temperature, current and internal voltage of the magnet coil v/s time curve for case-1 71
Figure 5.23. Resistance, temperature, current and internal voltage of the magnet coil v/s time curve for case-2 71
Figure 5.24. Resistance, temperature, current and internal voltage of the magnet coil v/s time curve for case-3 72
Figure 5.25. Resistance, temperature, current and internal voltage of the magnet coil v/s time curve for case-4 72
Figure 5.26. Resistance, temperature, current and internal voltage of the magnet coil v/s time curve for case-5 73
Figure 5.27. Resistance, temperature, current and internal voltage of the magnet coil v/s time curve for case-6 74
Figure 5.28. Resistance, temperature, current and internal voltage of the magnet coil v/s time curve for case-7 75
Figure 5.29. Quench protection circuit -CKT2 76
Figure 5.30. Resistance, temperature, current and internal voltage of the magnet coil v/s time curve for case-8 76
Figure 5.31. Quench protection circuit -CKT3 77
Figure 5.32. Resistance, temperature, current and internal voltage of the magnet coil v/s time curve for case-9 77
Figure 5.33. Quench protection circuit for 6T cryogen free superconducting magnet system 78

Figure 5.34. (a) Temperature characteristic of different parts of the magnet system with respect to time, during quench of magnet at 6T magnetic field and (b) Enlarge time section view of the Figure 5.34 (a) 79

Figure 6.1. Schematic diagram of the gas gap heat switch 83
Figure 6.2. Gas gap heat switch design (Solid Works) 83
Figure 6.3. Two copper blocks with thin SS tube 84
Figure 6.4. Thermal conductance v/s pressure in different gas flow regimes 85
Figure 6.5. Heat flow mechanism of gas gap heat switch 86
Figure 6.6. Schematic representation of integrated gas gap heat switch with CFMS 87
Figure 6.7. Test setup for the GGHS based VTI operation in CFMS 87
Figure 6.8. The cool down curve for CFMS with ON and OFF state of GGHS 88
Figure 6.9. Temperature profile of different above mentioned parts during magnetic field variation when gas gap heat switch is in ON state 89
Figure 6.10. Sample space temperature variation up to 300K at 1T magnetic field 90

List of Tables

Table 3.1.	NbTi wire specification (Supercon incorporation)	17
Table 3.2.	Load line parameters at 4.2K for the above specified NbTi wire	17
Table 3.3.	6T solenoid magnet design specifications	19
Table 4.1.	Shape parameter of current lead for the different material with optimized length	48
Table 5.1.	Solenoid coil parameter	59
Table 5.2.	User defined functions	61
Table 5.3.	User defined variables	62
Table 5.4.	Quench protection circuit (CKT1) parameters for the magnet coil	64
Table 5.5.	Quench analysis data for case-1 to case- 4	73
Table 5.6.	Quench analysis data for case-5 to case- 6	75
Table 5.7.	Quench analysis data for case-7	76
Table 5.8.	Quench analysis data for case-8 to case- 9	77

1.

INTRODUCTION

Introduction

Any research problem in condensed matter physics requires high field measurement to study physical properties of the potential materials and specially the magnetic materials which are of great technological importance. High magnetic fields are produced by the superconducting (SC) magnets which obviously require liquid helium at 4.2 K for operation and thus their use remained confine to a small number of laboratories, equipped with helium liquefaction facilities. The use of SC magnets in research laboratories spreads far and wide only with the development of SC magnets, cooled by the closed cycle refrigerators (CCR). Physical properties measurement systems based on these, so called, conduction cooled magnets or cryogen-free magnet system (CFMS) are a popular commercial experimental tool to study the physical properties of materials under high magnetic field and at low temperature.

The main aim of this thesis was to report very comprehensive experimental studies that I have carried out on different thermal phenomenon of the 6T Cryogen-free Superconducting Magnet System (CFMS) which was designed and built at IUAC, New Delhi. The superconducting magnet (NbTi) is cooled by the conduction process using the refrigeration capacity (35W@50K and 1.5W@4.2K) of the two stage GM cryocooler (SRDK-415D). A First stage of the cryocooler is thermally integrated with the thermal radiation shield and 2nd stage of the cryocooler is integrated with the NbTi magnet. One of major components of the CFMS is hybrid or binary current lead. The hybrid current lead consists of a thermally optimized metallic lead and a high temperature superconducting (HTS) lead. The metallic lead is connected between the ambient and 1st stage of the cryocooler and the HTS lead is connected between 1st stage and 2nd stage of the cryocooler, where finally the magnet is integrated.

One of the main objectives to study the designing aspects of the 6T NbTi magnet. The design of the solenoid coil with its dimensional description, is discussed in details in chapter-3. The load line, for magnet operation for the specific composite conductor (Cu:NbTi), provides the base for the design initiation. The critical surface characteristic of the NbTi superconductor with its thermal margin ensures stable magnet operation. The magnetostatic analysis with the use of finite element simulation software (OPERA-3D/TOSCA) is explained. This magnetostatic analysis gives the magnetic field profile of the 6T magnet and also able to explain the axial magnetic field distribution. The magnetic field homogeneity is the main point of concern of the magnet design with the help of this analysis, this feature is explained briefly. The cryogen-free magnet system is purely dependent over the close cycle refrigeration (CCR) for the cooling purpose. Each GM cryocoolers have their own thermal load characteristic. In this report the practical load curves for the GM cryocooler has been generated to correlate with the thermal performance of the magnet.

The performance of the CFMS greatly depends on the hybrid current lead. One of the objectives of the thesis is to do FEA analysis using ANSYS for different types of conduction-cooled metallic current lead which is discussed in chapter- 4. Current lead is thermally anchored with the cooling stages of the cryocooler. These thermal anchoring points are electrically insulated and thermally conductive with the different stages. During magnet operation, to ensure the higher thermal conductance for the heat loads dissipation coming from current leads, and simultaneously electrical insulation, a thermal anchoring scheme is experimentally studied in details. A thermal anchoring block is developed and with the use of different thermally conductive but electrically insulated materials, thermal contact resistance characteristic is found out for the operating temperature range of the system. A finite element

analysis has been done for the conduction cooled current lead, to find out thermal behavior of optimized current lead during under, over and operating current operation.

The operation of the superconducting magnet is dependent over the critical parameters of the superconductor. During magnet operation any small thermal perturbation can cause the instable magnet operation and if designed operating parameters cross the critical values then superconducting magnet become normal, this irreversible thermal process is known as quench. The quench process, types, causes and quench protection systems are discussed in details in chapter- 5. A finite element quench analysis (OPERA/QUENCH) for the 6T NbTi solenoid magnet is discussed with different operating conditions and with different types of quench protection circuits. The experimental quench thermal profile has been also presented in this report.

Most of the commercial CFMS comes with integrated variable temperature insert (VTI). The commercial VTI is based on the helium gas circulation through heat exchanger and condenser. Hence the commercial VTI systems, integrated with CFMS, are not actually cryogen-free in true sense. I have studied the feasibility of using a gas gap heat switch (GGHS) for VTI application in a CFMS. GGHS integrated VTI will make the system complete cryogen free. The design and development of test facility with measurement results are discussed in details in this report.

2.

LITERATURE REVIEW

Literature review

In 1983, the design concept of the cryogen-free superconducting magnet integrated with 13K at 2.5W two stage close cycle refrigeration system (CTI1020), is given by Hoenig *et al*. According to them the peak magnetic field was achieved 3.3T using low temperature superconductor (LTS) Nb_3Sn. The magnet was operated with 40A operating current with conduction cooled current lead which was incorporated 5W and 1W heat load at 70K and 14K stages of cryocooler [1]. Due to small refrigeration capacity of cryocoolers at 2^{nd} stage this design concept was not fitted with large heat loads embodiment by conduction cooled current lead. Since vapor cooled leads cannot be engaged in vacuum so this limits the maximum current capacity up to 40A only. In 1986, the discovery of HTS material by Bednorz and Mueller, gave the solution for thermal load problem [2]. The critical temperature of the high temperature superconductors (HTS) is gone up to 110 K in Bismuth (Bi) based high temperature superconductors discovered by Maeda *et al* (1989) [3]. After the HTS discovery, in 1992 world's first cryogen-free superconducting magnet system (CFMS) was practically developed by K Watanabe *et al* in High Field Laboratory for Superconducting Materials, Japan. This CFMS was designed to operate at 4.6K at 5T magnetic field with 465A operating current. They used Nb_3Sn material for coil formation and BSCCO-2223 (HTS) material for current lead [4]. Then after it various types of development are happened in CFMS technology. S. Yokoyama *et al* developed a 6K at 1.1W GM cryocooler based, 190 mm warm bore, and 0.7T rated field conduction-cooled magnet system for X-band klystron. This magnet was made with NbTi wire in three separated part coil format. It was also able to generate 5T field, if 100% operating current of load line at 4.2K was there [5]. In 1996, K Watazawa *et al* developed a cryocooler-cooled 6T NbTi magnet system which had 220 mm warm bore. This system worked at 6T field with 152A operating current at persistent switch mode [6]. In 1996, K Watanabe *et al* developed 11T NbTi/Nb_3Sn magnet system operated at 6K with the use of two 4K cryocoolers [7]. N.H. song *et al* (2000), developed a 5T with 4K close cycle refrigeration (CCR) at 0.5W. In this system they added powdered aluminium nitride (AlN) with the magnet winding insulation material (Epoxy), to raise the thermal conductivity of the insulating material [8]. In 2002, K Watanabe *et al* developed a 23T cryogen free hybrid magnet system worked with GM cryocooler. A 4.59T NbTi outer magnet coil with 3.41T Nb_3Sn inner coil, total 7T field was fixed for 300 mm warm bore. An inner 15.5T water cooled resistive magnet was fixed with the system that allowed 52 mm warm bore [9]. Yinming Dai *et al* (2006) presented a 6T conduction-cooled magnet system which had rotatable cryostat and abled to fix at horizontal and vertical direction easily [10]. In 2008, Berryhill *et al* developed a 6T cryogen-free magneto-optical system with the use of gas-gap heat switch. This system was able to provide variable temperature range of 10K to 300K in variable magnetic field for the material testing. The gas adsorption mechanism was employed in the gas gap heat switch to generate thermal conditioning [11]. In 2010, Yinming Dai *et al* made a conduction cooled split magnet system with 100 mm room temperature bore, which had BSCCO-2223/Ag (HTS) operated at 200A and NbTi operated at 136A [12]. In 2010, E Demikhov *et al* developed 8T magnet system with helium gas-gap heat switch for variable temperature operation. The gas was maintained in the gap by the use of external pumping [13]. K Watanabe *et al* (2013) developed Rutherford cable based (Nb3Sn/CuNb) 20T cryogen-free outsert for the 47T hybrid magnet. In Rutherford cable CuNb used as reinforcement material with Nb3Sn strands [14].

3.

6T CONDUCTION COOLED NbTi SOLENOID MAGNET SYSTEM

3.1 Introduction

3.2 Design of the NbTi solenoid magnet

3.3 NbTi superconductor characteristics

3.4 Current sharing temperature and temperature margin

3.5 Operating load line curve for 6T NbTi solenoid magnet

3.6 Thermal load curves for GM cryocooler

3.7 Finite element magnetostatic analysis

3.8 6T solenoid magnet operation

3.1 Introduction

A superconducting magnet is an electromagnet which is constructed by the use of superconducting materials. Superconducting materials generally in the form of wire or tapes are used for the electromagnet. Superconducting magnets are made in different shapes like solenoid, dipole, quadrupole or toroidal shape. There are thousands of superconductor materials, both high temperature superconductor (HTS) and low temperature superconductor (LTS), available but magnet grade superconductor materials are very few such as NbTi or Nb_3Sn (LTS) and YBCO or BSCCO (HTS). These superconductors are characterized by critical current density (J_c), critical field (B_c) and critical temperature(T_c). Each superconductor has its 3-dimensional critical surface.

The superconducting magnets are generally operated below its critical temperatures. Conventional superconducting magnet are generally bath-cooled. If superconducting magnet is made with HTS material then they are mainly operated at the temperature range of 65-77K in liquid nitrogen (LN2) bath. The LTS magnets are mainly operated at 4.2K in liquid helium (LHe) bath. The development of cryogen-free system is possible due to 4K closed cycle refrigerators (CCR). Cryogen-free or CCR based systems are becoming popular in the low temperature physics laboratory, where the availability of liquid helium is the main concern. This cryogen-free magnet system (CFMS) technology is purely based on using refrigeration capacity of CCR. In a CFMS, the superconducting magnet is cooled only by the conduction process using the cooling capacity of a CCR. The GM cryocooler (GMC) and pulse tube cryocooler (PTC) are the two types 4K CCRs, used for CFMS. For the conduction cooled LTS magnet systems, two stage CCRs are used. CFMS has many components which consume lot of refrigeration power during magnet operation, one of these components is current lead for the magnet charging. A pair of optimized metallic/alloy current lead are used for electrical charging in liquid helium bath cooled magnet. Higher refrigeration capacity, in a bath cooled magnet system, are able to take care the heat loads coming from the conventional metallic current leads. But in case of CFMS, the CCR will not be able to take care the thermal load coming through the conventional current lead because of limited refrigeration capacity of CCR. The discovery of HTS current lead presents the solution regarding this thermal imbalance problem. HTS lead made it possible to develop hybrid lead configuration which is the only solution for LTS based CFMS.

3.1.1 Components of the 6T cryogen free superconducting magnet system

The 6T CFMS, indigenously developed at IUAC, consists of many components. Some of the major components are mentioned below. The schematic of the system is shown in Figure 3.1.

1. *Superconducting magnet*- The main part of any cryogen free superconducting magnet system is superconducting magnet. These magnets are generally made with LTS materials and in solenoid form.

2. *Cryocooler (CCR)* – Two stage GM cryocoolers or two stage pulse tube cryocoolers are used for the cooling purpose of magnet system. These regenerator based heat exchanging systems are based on the Gifford-McMahon cycle.

3. *Hybrid current lead*- Hybrid current lead is the combination of optimized metal/alloy current lead and HTS current lead.

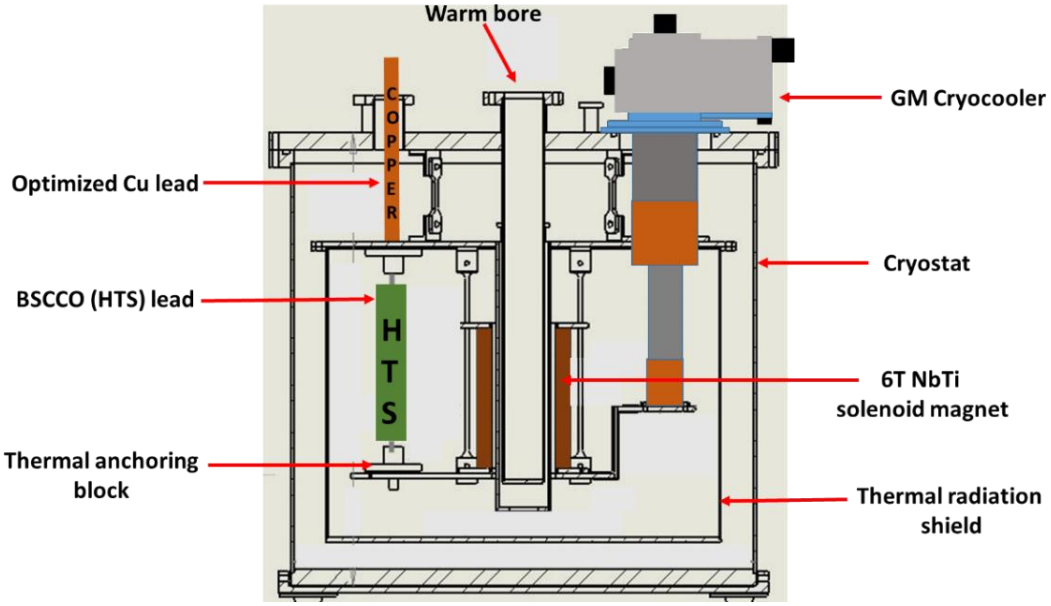

Figure 3.1. Schematic representation of 6T CFMS.

4. *Thermal radiation shield*- Thermal radiation shield is generally made with electrolyte tough pitch copper (ETP Cu) material in highly polished form to reduce radiation heat transfer to the magnet system.

5. *Cryostat*- The cryogen free superconducting magnet system is housed inside a vacuum jacket which is known as cryostat. This is made from stainless steel (SS-304) material.

The cryogen free superconducting magnet system has other accessory components which are used for the magnet operation. A superconducting magnet power source is attached with the magnet. This power source is able to feed high amount of current (~100A) to the magnet. The whole system is operated at vacuum condition so for the vacuum measurement, an ultra-high vacuum gauge is attached with the system with the vacuum gauge monitor. There are many temperature sensors mostly calibrated silicone diode mounted at different position of the CFMS. Cernox sensors are used in the magnetic field region. These calibrated Cernox sensors are capable to read the cryogenic temperature at high magnetic field conditions. These temperatures are read, by using temperature monitor [15].

3.2 Design of the NbTi solenoid magnet

Magnetic field for the electromagnets can be found out with the use of Ampere's law. As the equation of magnetostatics states that,

$$\nabla \times B = \mu_0 J \tag{3.1}$$

Where μ_0 is the magnetic permeability of vacuum, J is current density and B is the magnetic field around circuit.

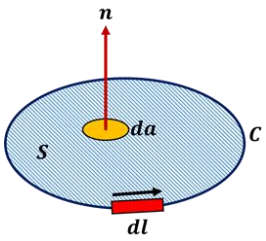

Figure 3.2. Magnetic field around conductor C.

Then a magnetic induction induced around a circuit C by the current density J through the open surface S bounded by C (as shown in Figure 3.2) and if we incorporate integral on the both side of Eq. (3.1) then,

$$\int_S (\nabla \times B)\, nda = \mu_0 \int_S J.nda \tag{3.2}$$

And using stokes theorem,

$$\oint_C B.dl = \mu_0 I \tag{3.3}$$

Where I is the current passing through the conductor. Eq. (3.3) is the mathematical representation of Ampere's circuital law for a current carrying conductor. The Ampere's law states that "*the line integral of magnetic field around any closed path is equals to the μ_0 times of the current in the closed loop conductor*" [16].

The direction of the magnetic field can be found out with the use of Ampere's right hand rule i.e. if current carrying conductor is wrapped by the fingers in such a way that direction of the current is in the direction of right hand's fingers, so thumb is in the direction of the magnetic fields north (shown in Figure 3.3).

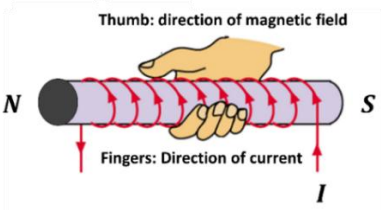

Figure 3.3. Schematic representation of Ampere's right hand rule.

A helical shaped electromagnetic conductor coil which has diameter smaller than its length is known as solenoid, as shown in Figure 3.4. Solenoid magnets are used for the production of uniform magnetic field and direction of this magnetic field can be determined by using Ampere's right hand rule.

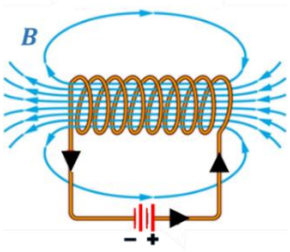

Figure 3.4. Schematic of Solenoid coil.

The magnetic field at the center (B_0) of an infinite long solenoid is given by the relation,

$$B_0 = \mu_0 \lambda N I \tag{3.4}$$

Where N is the turn density i.e. number or turns per unit length (turns/m), I (A) is the current passing through the coil conductor and λ is the packing factor of the solenoid coil. Here the packing factor implies that the actual conductor cross sectional area to the overall cross sectional area of the solenoid coil winding. The packing factor of a solenoid coil is described as,

$$\lambda = \frac{Conductor\ cross\ sectional\ area\ in\ the\ solenoid\ coil}{Over\ all\ cross\ sectional\ area\ of\ the\ solenoid\ coil} \tag{3.5}$$

It can be also represented as,

$$\lambda = \frac{n.N.A_{NbTi}}{(b-a).l} \tag{3.6}$$

Where n is the number of filaments of the NbTi conductor in the wire, N is the total number of turns in the winding, A_{NbTi} is cross sectional area of the NbTi conductor filament, a is the inner radius of winding, b is the outer radius of the winding and l is the full length of the winding.

Generally, the coil winding cross sectional area includes NbTi superconductor, conductor insulation, epoxy, void gaps. So the value of λ is always less than one because actual conductor area is always less than the total winding cross sectional area.

The differential magnetic field dB at particular point by the differential current element and distance between them is r then,

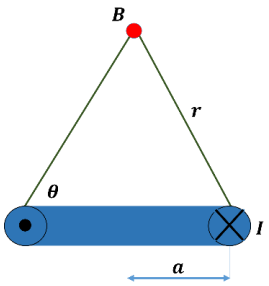

Figure 3.5. Current carrying loop of radius a.

$$dB = \frac{(Ids \times r)}{4\pi r^3} \tag{3.7}$$

If Eq. (3.7) is simplified then,

$$B = \frac{I\,(2\pi a) r.sin\theta}{4\pi r^3} = \frac{Iasin\theta}{2r^2} \tag{3.8}$$

If $sin\theta = \frac{a}{r}$ and $r^2 = a^2 + z^2$ then,

$$B = \frac{a^2 I}{2(a^2+z^2)^{3/2}} \tag{3.9}$$

If the problem related to the uniform current density coil then axial field at the centre of the solenoid coil is,

$$B_{(0,0)} = \frac{r^2 \lambda J dA}{2(r^2+z^2)^{3/2}} \tag{3.10}$$

The axial magnetic field at the centre of the solenoid coil can be found out by integrating the Eq. (3.10).

$$B_{(0,0)} = J\lambda a F(\alpha, \beta) \tag{3.11}$$

Where J (A/m^2) is the current density of the coil and $F(\alpha, \beta)$ is the field factor or fabry factor of the solenoid coil. Field factor is a dimensional parameter which is based on inner radius, outer radius and length of the solenoid coil. Field factor is given by,

$$F(\alpha, \beta) = \frac{4\pi}{10} \beta \log_e \left\{ \frac{\alpha+\sqrt{\alpha^2+\beta^2}}{1+\sqrt{1+\beta^2}} \right\} \times 10^{-6} \tag{3.12}$$

Where

$$\alpha = \frac{b}{a} \tag{3.13}$$

And

$$\beta = \frac{l/2}{a} \tag{3.14}$$

Where $a, b,$ and l are the inner radius, outer radius and full length of the solenoid coil as shown in Figure 3.6.

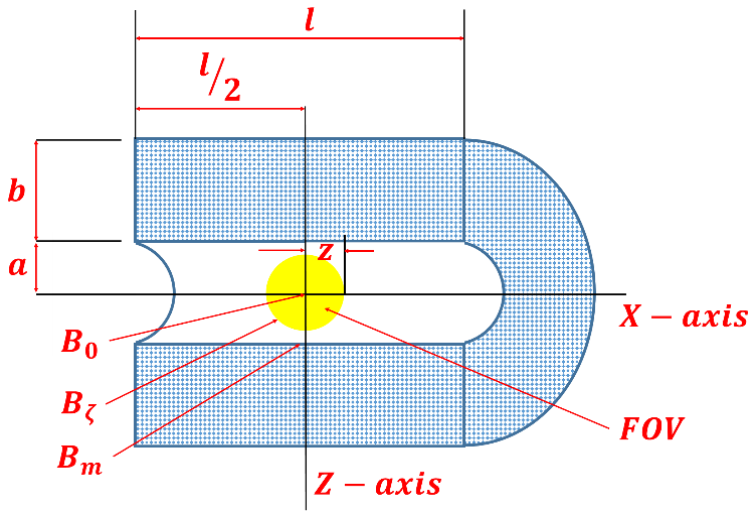

Figure 3.6. Dimensional cross section view of solenoid coil.

These dimensional parameters (α *and* β) are the deciding factors for the coil shape i.e. coil will be thick and short or thin and long. Minimum volume of winding $V = 2\pi a^3 (\alpha^2 - 1) \beta$ for particular α and β, provides solution for this problem. The minimum volume resembles lowest amount of superconductor for the coil winding for the desired field i.e. it reduces the cost of design. Any deviation from the minimum volume point for particular α and β would require more superconducting material for the same solenoid but a problem is there with minimum volume coil design, it does not ensure good field uniformity for the magnet coil [17-19].

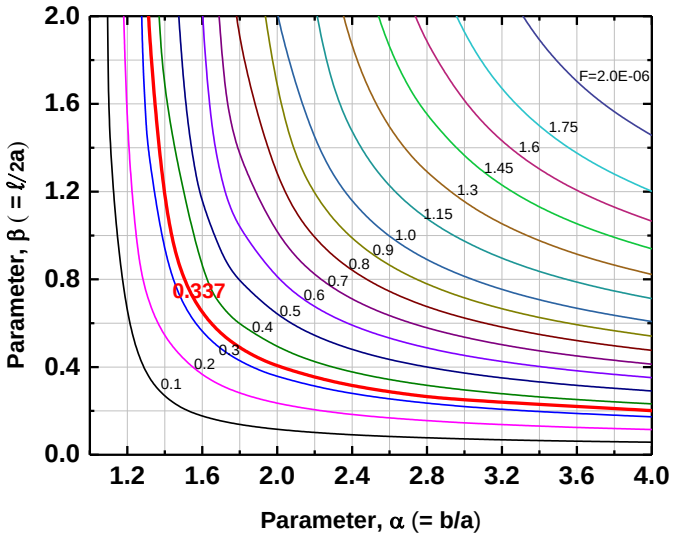

Figure 3.7. Field factor, $F(\alpha, \beta)$ as a function of α and β.

Figure 3.7 shows the field factor as function of α and β. There are several combination of α and β are possible for the single field factor value. If minimum volume consideration is followed then field uniformity will be disturbed and also the coil will be become thicker and shorter i.e. the magnet coil consumes more winding material. So for the high field uniformity and less material consumption point of concern, always select the α and β values in such a way that they able to fulfill the desired one. For this purpose select α and β, away from the minimum volume condition and prefer the larger β value.

Magnetic field homogeneity or uniformity of the coil in a spherical volume which is known as diametrical spherical volume (DSV) or field of interest (FOI) or field of view (FOV), is expressed as $\Delta\zeta$ in the sphere of normalized radius $\zeta = \frac{z}{a}$ which is,

$$\Delta\zeta = \frac{B_0 - B_\zeta}{B_0} \times 100\% = \frac{F_0 - F_\zeta}{F_0} \times 100\% \tag{3.15}$$

Where B_ζ and F_ζ represent the axial magnetic field and the field factor respectively at the point $\zeta = \frac{z}{a}$. The F_ζ is expressed as,

$$F_\zeta = \frac{2\pi}{10}\left[(\beta - \zeta)\ \log_e\left\{\frac{\alpha+\sqrt{\alpha^2+(\beta-\zeta)^2}}{1+\sqrt{1+(\beta-\zeta)^2}}\right\} + (\beta + \zeta)\ \log_e\left\{\frac{\alpha+\sqrt{\alpha^2+(\beta+\zeta)^2}}{1+\sqrt{1+(\beta+\zeta)^2}}\right\}\right] \tag{3.16}$$

The solenoid magnets are designed for the center magnetic field but the maximum magnetic field (B_m) in the winding is generated at the innermost winding layer rather than the magnetic center. The coil operating current density is decided with the center magnetic field but B_m is higher than B_0 which further reduces the critical current value. For an efficient winding design which does not allow to generate magnetic field higher than its desired magnetic field, always keep the ratio B_m/B_0 as small as possible. The B_m/B_0 ratio is also a deciding factor for field homogeneity i.e. if the ratio is small and close to one then field uniformity is high. Figure 3.8

shows the maximum magnetic field at the inner most layer of the winding for the 6T center magnetic field with respect to β value for the different values of α.

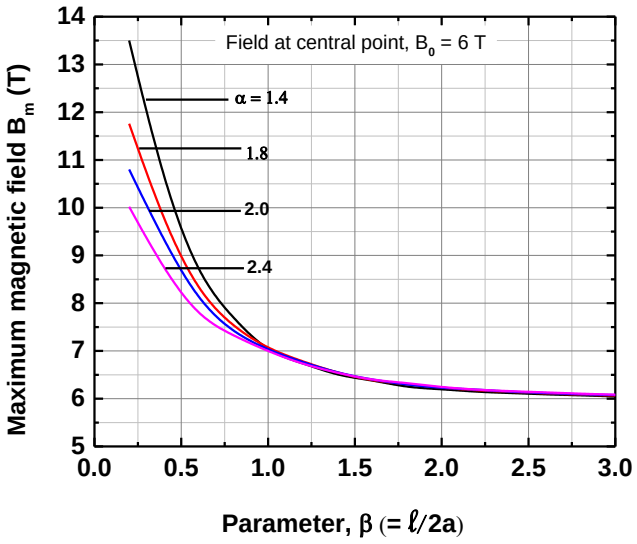

Figure 3.8. Maximum field B_m v/s β graph for different values of α.

It is clear from the Figure 3.8 that if β value is high for the certain desired center magnetic field then the maximum magnetic field value reduces. For 6T center magnetic field if β value is greater than one, so for different values of α, maximum magnetic field almost become similar. If β value further increases beyond two, then the B_m/B_0 ratio becomes smaller and saturates beyond β = 3. So if B_m/B_0 ratio is small then field uniformity is high and also maximum magnetic field reduction allows higher critical current operation and it becomes closer to the critical current density of center magnetic field [19-21].

For designing of the uniform current density coil i.e. solenoid coil first criteria of magnet design is to select the operating current for the desired magnetic field which later implies operating current density of the coil. This operating current density provides desired central magnetic field with the high homogeneity. The operating current parameter is chosen in such a way that it has ability to come under critical surface, i.e. ability to provide current margin and temperature margin for the magnet operation. Once the operating current parameter is decided with the available data of the conductor is using for the coil manufacturing then the next step is to fix the inner diameter of the coil. This dimensional fixing is very important as concern to field homogeneity point of view because field homogeneity depends over the dimensional parameters only which later help to generate uniform magnetic field at the centre of the coil. Inner diameter of the magnet winding gives the dimension of the former or bobbin on which magnet winding will be done. Once the inner diameter is decided, then outer diameter is dependent over the conductor cross sectional area, which afterward decide the number of layers of the conductor in the winding. These number of layers will fix the thickness of the winding. Winding thickness is totally dependent over the operating current which has been fixed in first step of design. If operating current density is less for the desired magnetic field then number of layer in the coil winding is higher that means thick winding is there. On the other side, if operating current density is high then number of layers are less i.e. thin winding.

For the operating current selection always prefer a value which allows moderate thickness to the winding and at the same time also able to fix the thermal margins for the magnet operation.

3.3 NbTi superconductor characteristics

The superconductor properties are described in the form of critical current density (J_C), critical temperature (T_C) and critical magnetic field (B_C). These properties are related to each other and combined to introduce critical surface of the superconductor. The critical surface of the NbTi superconductor is mentioned in Figure 3.9, in which critical magnetic field (B_C) in Tesla is mentioned in X- coordinate, critical current density (J_C) is mentioned in Y- coordinate in kA/mm^2 and critical temperature (T_C) is mentioned in Z- coordinate in Kelvin.

The maximum current carrying capacity of the NbTi superconductor has been determined by the critical temperature (T_C) and second critical magnetic field (B_{C2}) as well as critical current density (J_C) . The base line of critical surface which describes the relation between B_{C2} and T_C at zero current is found out by the intrinsic physical properties of the superconducting material. So according to alloy composition the percentage of Ti (Titanium) varies 45 to 55 % by weight in Nb (Niobium).

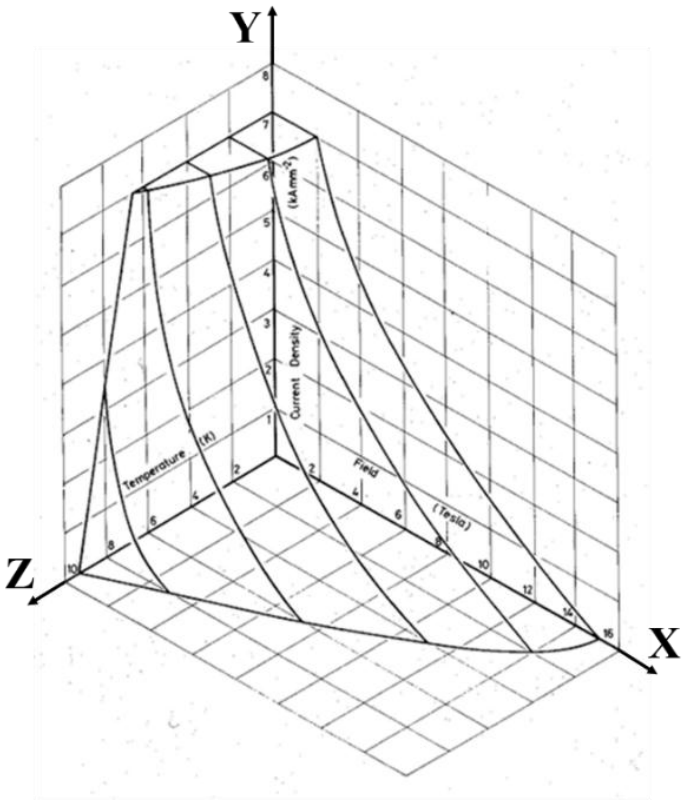

Figure 3.9. Critical surface of the NbTi superconductor.

The critical temperature of the NbTi lies between 9 and 9.3K. So the base line for the NbTi with reasonable accuracy is,

$$B_{C2}(T) = B_{C2}(0)\left\{1 - \left\{\frac{T}{T_{C(0)}}\right\}^{1.7}\right\} \qquad when\ 0 < B < 10Tesla \qquad (3.17)$$

Or

$$T_C(B) = T_C(0)\left[1 - \left\{\frac{B}{B_{C2}(0)}\right\}\right]^{0.59} \quad (3.18)$$

Where $T_C(0) = 9.2\ K,$ $B_{C2}(0) = 14.5\ Tesla,$ $B_{C2(4.2K)} = 10.4\ Tesla$

For 6T magnet $T_C(6) = 6.71$K and $B_{C2}(3.2) = 12.1$ Tesla

The critical current density of the superconductor at known magnetic field and temperature is determined by the use of Lubell's formulae. The value of critical current density is dependent over the critical temperature for the particular magnetic field. The Lubell's formulae is mentioned below,

$$J_C(B,T) = J_C(B,4.2)\left(\frac{T_C(B)-T}{T_C(B)-4.2}\right) \quad (3.19)$$

For 6T magnet operating at 3.2K the value of $J_C(6,3.2) = 2307$ A/mm^2, when $J_C(6,4.2) =$ 1650 A/mm^2 [17, 22, 23].

3.4 Current sharing temperature and temperature margin

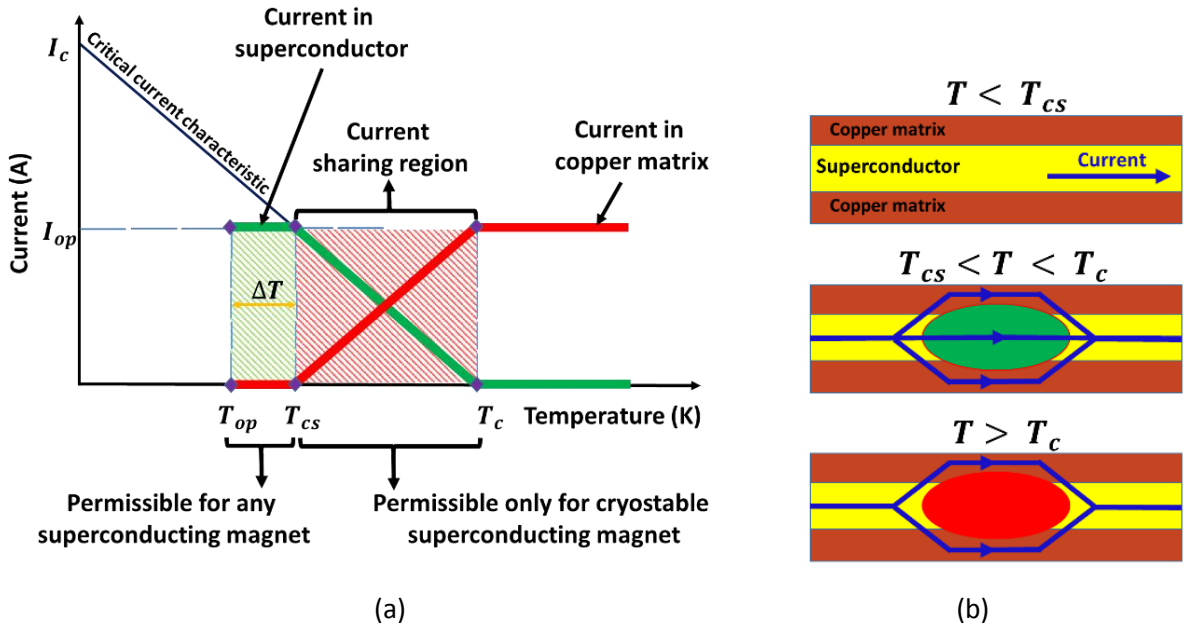

Figure 3.10. (a) Current sharing model for composite superconductor wires.
(b) Current distribution in composite superconductor at different temperature regimes.

Any of the superconductor which is developed in composite form that follows current sharing model. If superconducting magnet is designed to operate at particular magnetic field then for that magnetic field composite superconductor has critical operating surface which shows that if magnet operation within this zone and with designed parameter then there is no problem but

once the operating parameters cross its critical value then they follow sharing pattern of current which causes thermal disturbances. Figure 3.10 shows that if temperature increases and crosses the value of current sharing temperature then current starts to share by superconductor and matrix, and further increment of temperature, beyond critical temperature then all current starts to flow only through matrix metal because of less resistive nature of matrix metal then superconductor, which is normal now.

The critical magnetic field increment causes operating temperature margin reduction but besides magnetic field, the operating current in the superconductor further reduces the allowable temperature in the multi filamentary composite conductor and this temperature is known as current sharing temperature of the conductor. It is described as,

$$T_{CS}(B,J) = T_{OP} + \left\{(T_C(B) - T_{OP})\left(1 - \frac{J_{OP}}{J_C}\right)\right\} \tag{3.20}$$

Where T_{OP} is the reference temperature i.e. 4.2K, J_{OP} is the operating current density and J_C is the critical current density at operating temperature (T_{OP}) and magnetic field (B) of the superconductor. In this formulae, current sharing temperature is in the form of linear approximation with operating temperature and current density. If the superconductor material crosses the current sharing temperature limit then conductor becomes normal and starts to show resistive behaviour. For the stabilized operation of any conduction cooled magnet system temperature margin is important aspect. The current sharing temperature governs the temperature margin of the magnet. The critical temperature of NbTi superconductor is reduced when it operates at particular magnetic field B and current density J , so $T_C(B)$ is always less than $T_C(0)$. The difference between the current sharing temperature (T_{CS}) and the operating temperature (T_{OP}) is known as temperature margin (ΔT) for the stabilize magnet operation. Which is,

$$\Delta T = T_{CS}(B,J) - T_{OP} = \left\{\left(T_C(B) - T_{op}\right)\left(1 - \frac{J_{OP}}{J_C}\right)\right\} \tag{3.21}$$

If the composite superconductor starts operate beyond this temperature margin then superconductor becomes normal. Current starts flowing through both in composite metal (copper) and superconductor and after critical temperature it completely flows through copper matrix metal. Eq. (3.21) states that if the operating current density and operating temperature increase then temperature margin decrease. For the stable operation the only factors to concern about that is J_{OP} and T_{op} because other parameter like $T_C(B)$ and J_C are fixed for the desired magnetic field [23].

For 6T magnet, if the operating temperature T_{OP} is 3.2K and the $\frac{J_{OP}}{J_C} = 0.68$, then current sharing temperature is 4.3K and the temperature margin at this current sharing temperature is 1.1K.

3.5 Operating load line curve for 6T NbTi solenoid magnet

Operating load line curve is important design aspect for the superconducting magnet development. The operating load line curve describes the relation between the desired magnetic field and operating current. Generally, each commercially available wire has its own load line characteristic. The specification of multi-filamentary NbTi wire, used for 6T NbTi magnet, is summarized in Table 3.1. The $I_c - B_c$ data for the NbTi conductor is given in Table 3.2.

Table 3.1. NbTi wire specification (Supercon incorporation) [24].

Model Number	Supercon (54S-33)
Wire insulation	**Formvar (polyvinyl formal)**
Wire Diameter- bare (mm)	**0.5**
Wire diameter- with insulation (mm)	**0.54**
Cu: NbTi ratio	**2.0**
Number of filaments	**54**
Diameter of each filament (µm)	**38**

Table 3.2. Load line parameters at 4.2K for the above specified NbTi wire [24].

Critical current I_C (A)	Critical magnetic field B_C (T)
240	**3**
170	**5**
105	**7**
32	**9**

Figure 3.11 shows the operating load line curve for the 6T solenoid magnet. At 6T magnetic field the critical current of the conductor is around 151A. The thermal margin needs to be increased for the stable operation of the magnet system. To achieve moderate thermal margin, the operating current has been chosen 68 % (~ 102A) of the critical current at the peak field. At this operating current, magnet can generate 6T magnetic field with 32% of the critical current margin and 15% of the critical field margin. As discussed earlier that peak magnetic field is generated at the innermost winding of the coil which is 6.2T. This maximum field restrict the operating current of the magnet to go to the critical current value related to centre field and stop at critical current related to the maximum magnetic field. So for 6.2T the critical current is around 145A, as shown in Figure 3.11 and now operating current is about 71% of the critical current at maximum field. So the selection of the critical current should be as per the peak magnetic field not for the centre magnetic field.

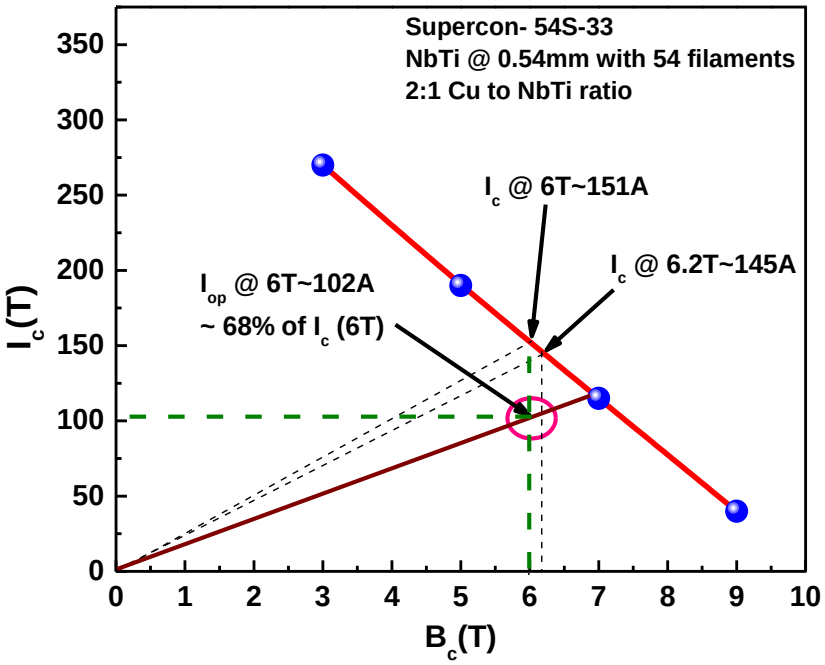

Figure 3.11. Load line curve at 4.2K for the 6T conduction cooled magnet.

First step of magnet design is to select the operating current value with a certain current margin. So 102A operating current has been decided which is ~ 68% of its critical current value i.e. 151A. Packing factor of the magnet winding is around 0.85. The inner diameter of the coil is decided as 104mm with its 200mm winding length.

There are 18.52 number of wires present per cm with wire diameter of 0.54mm. For the 6T magnet according to Eq. (3.4), the value of N is 55070.9 turns/m i.e. 550.71 turns/cm. So the number of layers are, 550.71/18.52, which comes around 30 no of layers. Then from Eq. (3.11) for the 6T magnetic field value the field factor comes around 0.34×10^{-06}. Hence the value of α is 1.31 and β is 1.92. According to α value, outer diameter of the coil is found out which able to compensate the minimum number of wire turns require for the coil. The selected wire diameter is 0.54mm, so the outer diameter of the coil is around 137mm with the 10700 no of turns in the coil winding i.e. thickness of the winding is 16.5mm. The design parameters of the 6T NbTi magnet are given in Table 3.3.

Table 3.3. 6T solenoid magnet design specifications.

Design parameter	Value
Operating current (I_{OP})	**102A**
Packing factor (λ)	**0.85**
Turn density (N)	**550 (turn/cm)**
Total number of layers	**30**
Inner diameter ($2a$)	**104mm**
Outer diameter ($2b$)	**137mm**
Winding Length ($2l$)	**200mm**
Field factor $\{F(\alpha,\beta)\}$	**0.34×10^{-06}**
$\alpha\ (=\ ^{b}/_{a})$	**1.31**
$\beta\ \left(=\ \frac{^{l}/_{2}}{a}\right)$	**1.92**
$^{B_m}/_{B_0}$	**1.03**
Maximum magnetic field (B_m)	**6.2T**
Self-inductance (L)	**5.5H**

3.6 Thermal load curves for GM cryocooler

The 6T NbTi conduction cooled magnet system is integrated with a two stage SRDK-415D GM cryocooler (shown in Figure 3.12) which has refrigeration capacity 1.5W at 4.2K [25]. For the estimation of thermal load profile of the superconducting magnet system load curves for CCR are necessary. In this section practical load curves of GM cryocooler have been discussed. We have generated the refrigeration curves for the both stages of SRDK-415D GM cryocooler in a CCR based test rig [26].

Figure 3.12. SRDK-415D GM cryocooler (SHI Cryogenics Group).

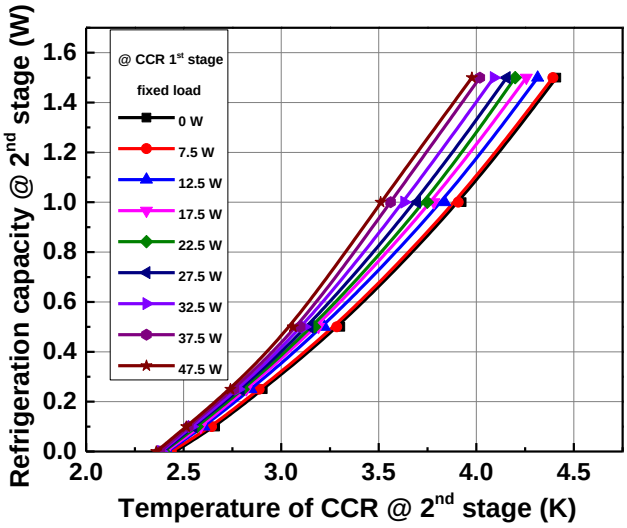

Figure 3.13. Refrigeration capacity v/s temperature curve for the 2nd stage at different thermal loads on 1st stage.

Figure 3.13 shows that the refrigeration capacity of 2nd stage with respect to the temperature of 2nd stage with different thermal loads at the 1st stage. At 6T field, the temperature of the 2nd stage cold head of the CCR is 3.2K which corresponds to the refrigeration capacity of 0.45W and at this condition 1st stage is maintained approximately at zero load. At 3.2K, the refrigeration capacity at 2nd stage raise up to 0.7W when the load at the 1st stage increases to 47.5W.

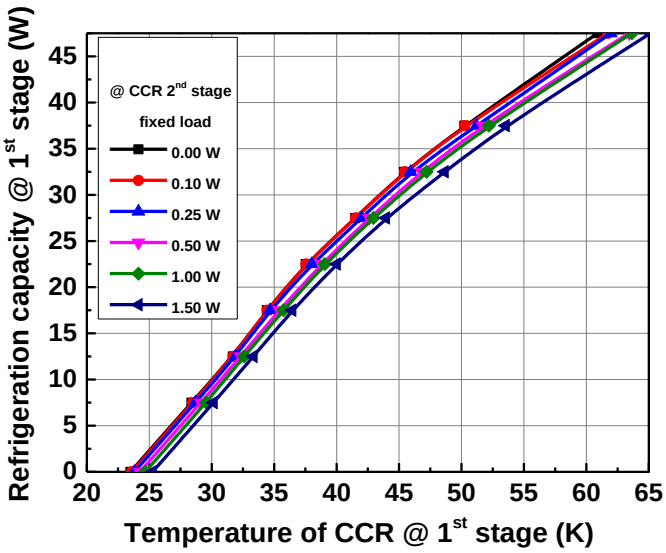

Figure 3.14. Refrigeration capacity v/s temperature curve for the 1st stage at different thermal loads on 2nd stage.

Figure 3.14 shows the refrigeration capacity curves of the 1st stage with respect to its temperature for different thermal loads at 2nd stage of the CCR. During magnet operation 1st stage is maintained around 39.5K so at this temperature range refrigeration capacity at 1st stage is 25W when 2nd stage thermal load is nearby 0W. When thermal loads on 2nd stage become 1.5W then at 39.5K temperature 1st stage refrigeration capacity reduces to 21W.

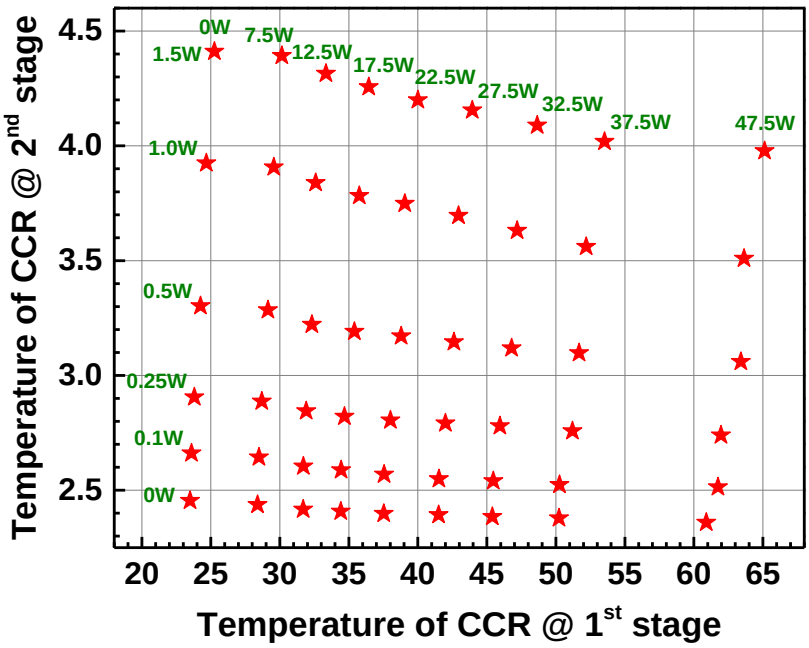

Figure 3.15. Practical load map of SRDK-415D GM cryocooler.

The practical load map of SRDK-415D GM cryocooler has been generated by using different thermal operating conditions mentioned in Figure 3.13 and 3.14. In Figure 3.15, the X-axis represents the temperature of 1st stage and the Y-axis represents the temperature of 2nd stage of the GM cryocooler with different refrigeration capacities.

3.7 Finite element magnetostatic analysis

Finite element magnetostatic analysis has been done for the 6T conduction cooled magnet system using OPERA electromagnetic simulation software [27]. TOSCA magnetostatic program is used for the magnetostatic analysis in OPERA. For this analysis, coil design coordinate parameters are put in to the software that forms a solenoid conductor then using Biot-Savarts current source element, current density is defined for the conductor i.e.

$$J = \frac{I_{op} \times total\ no.of\ turns}{(b-a) \times l} \tag{3.22}$$

Then the solution has come after iterations which represents the magnetostatic profile of the 6T solenoid magnet.

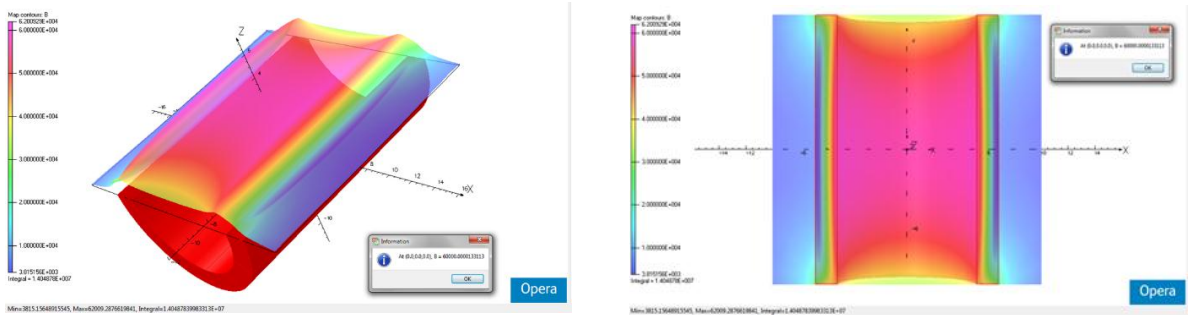

(a) (b)

Figure 3.16. The histogram (a) and plane (b) representation of the magnetic field profile of 6T solenoid magnet.

Figure 3.16 indicates the magnetic field distribution of 6T solenoid magnet in histogram (a) and plane (b) format at XY- surface.

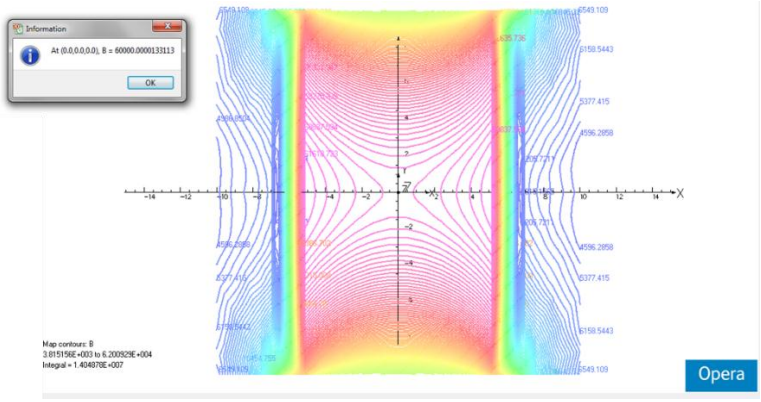

Figure 3.17. The line representation of the magnetic field profile of 6T solenoid magnet.

Figure 3.17 shows that magnetic field line distribution of the 6T solenoid magnet using OPERA. It indicates that the magnetic field lines become dense when go away along X-axis from the magnetic center of the magnet. The density of the magnetic field lines become maximum at the inner most layer of the winding. It is the clear indication that the maximum magnetic field is generated at the inner most winding layer rather than magnetic center.

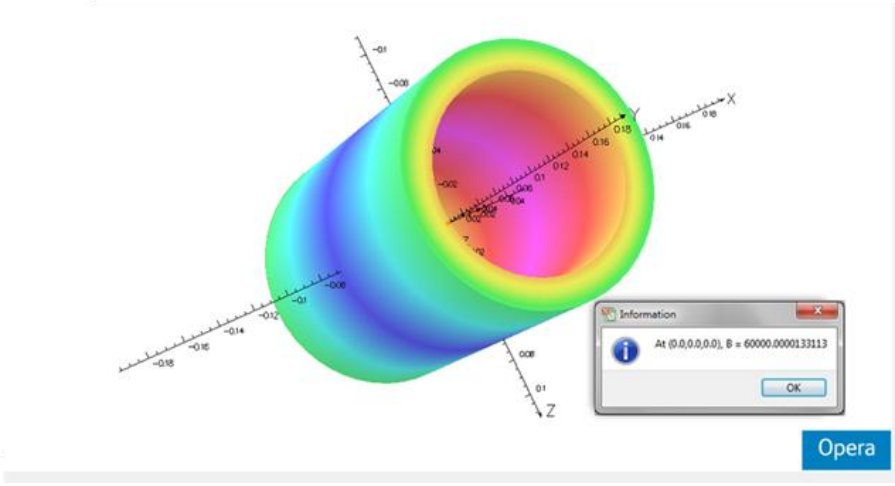

Figure 3.18. Magnetic field profile of 6T solenoid magnet with in the coil.

Figure 3.18 shows that the peak field formation at the innermost layer. After that, the magnetic field starts decreasing along the X-axis within the coil layers and achieves its minimum value.

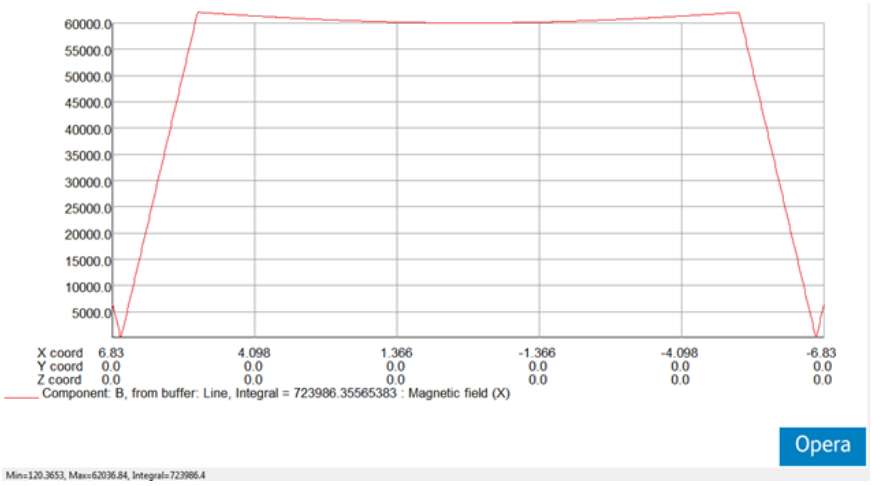

Figure 3.19. Magnetic field distribution along the X-axis of the solenoid coil i.e. transverse magnetic field.

Figure 3.19 shows the magnetic field distribution along the X-axis i.e. along radial direction. It is clear from the Figure 3.18 that at the outer most layer magnetic field distribution is almost zero. At the inner most layer around 62000 gauss i.e. 6.2T maximum magnetic field is there in the magnet.

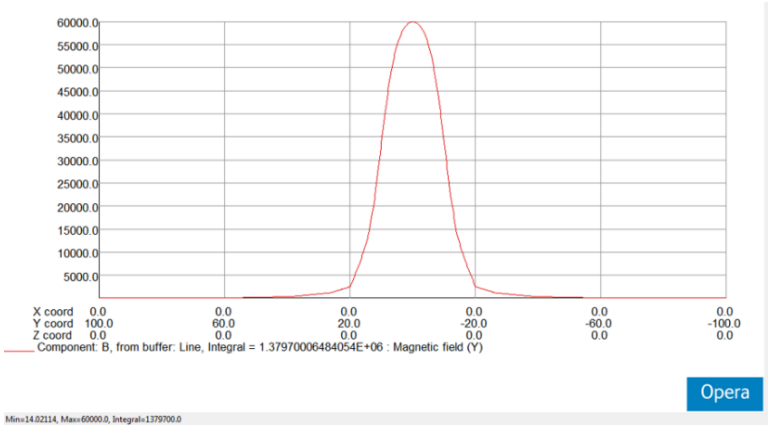

Figure 3.20. Magnetic field distribution along the Y-axis of the solenoid coil i.e. axial magnetic field.

Figure 3.20 shows the axial magnetic field variation (along the Y-axis). The center magnetic field is come 60000 gauss i.e. 6T, which is the desired magnetic field of the system.

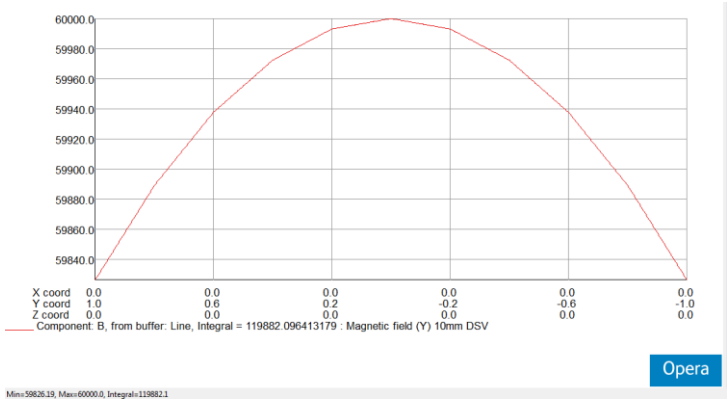

Figure 3.21. Magnetic field distribution along the Y-axis of the solenoid coil for 10mm DSV.

Figure 3.21 indicates the magnetic field along the Y-axis for 10mm DSV (diametrical spherical volume). Figure 3.22 shows magnetic field profile at 10mm DSV of the 6T magnet. The field homogeneity for the 6T magnet system is around 0.07% for 10mm DSV.

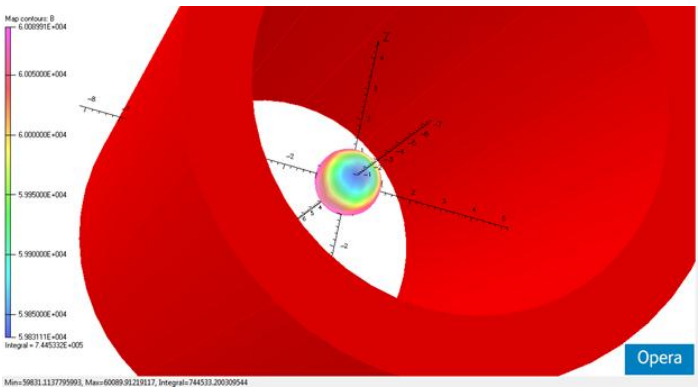

Figure 3.22. 3-D representation of 10mm radius sphere which resembles DSV.

3.8 6T solenoid magnet operation

Magnet cool down-

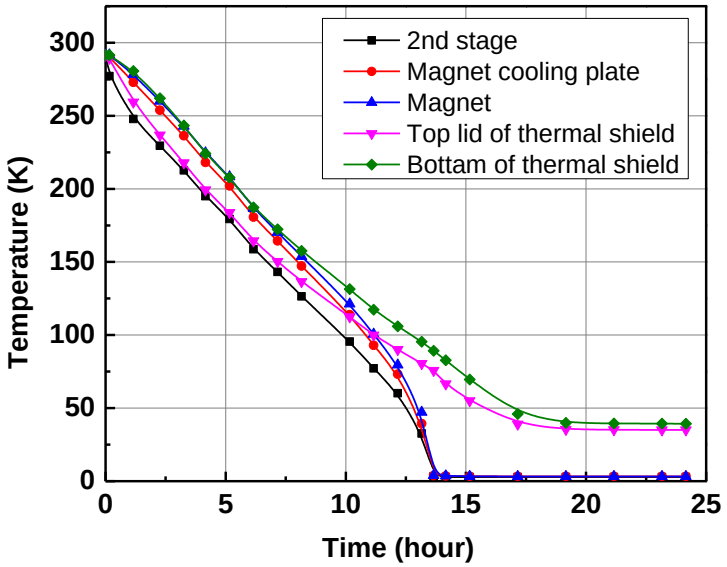

Figure 3.23. CFMS cool down curve.

During cool-down, the CFMS takes approximately 16 hrs to reach the steady state temperature. The steady state temperature of the 2nd stage of the CCR, magnet and top lid of thermal radiation shield are 2.9K, 3.2K and 39K respectively, as shown in Figure 3.23.

Magnet charging

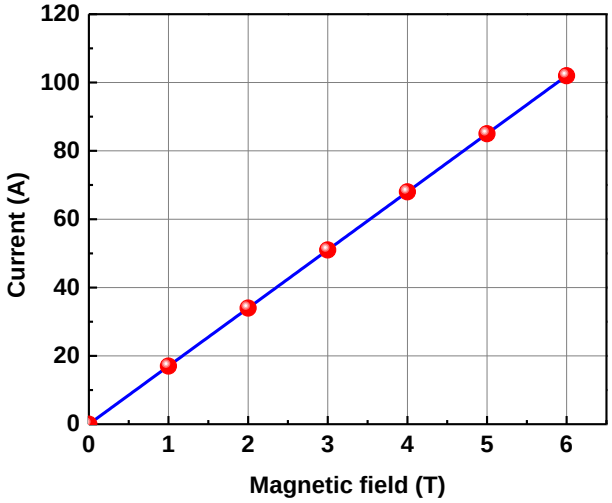

Figure 3.24. Magnetic field v/s current curve.

Figure 3.24 shows that magnet reaches at its 6T magnetic field at 102A current.

CFMS temperature profile during magnet charging

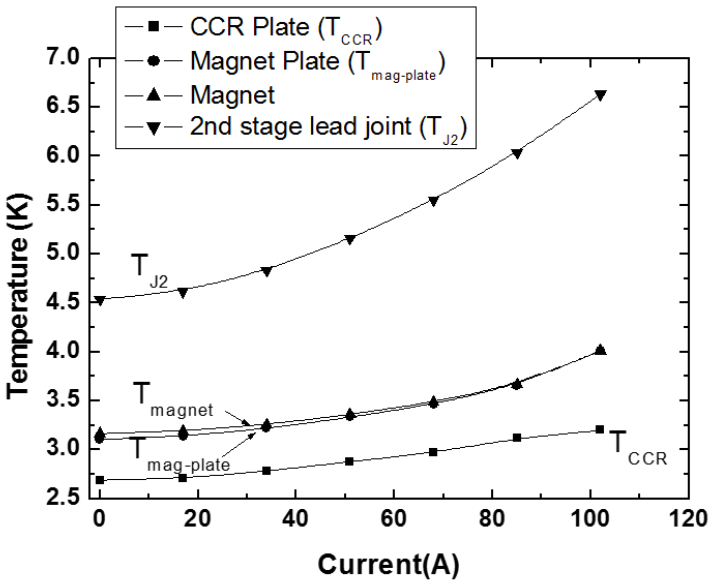

Figure 3.25. Temperature profile of magnet and 2nd stage cooling attachments, during magnet charging.

6T magnet is energized up to its operating current 102A to generate 6T magnetic field. During magnetic charging temperatures of the magnet, magnet cooling plate and 2nd stage inter lead joint increases up to 3.9K, 4K and 6.7K respectively, as shown in Figure 3.25. This temperature increment pattern is happened because of ohmic heat losses at different resistive joints.

4.

CONDUCTION COOLED HYBRID CURRENT LEAD

4.1 Introduction

4.2 Optimization of metallic/ alloy current lead

4.3 Thermal impedance measurement of inter-lead joint of hybrid lead

4.4 ANSYS heat flow analysis of hybrid current lead

4.1 Introduction

Superconducting magnet is generally operated at temperatures much below the critical temperature of superconductor. The superconducting magnet also needs higher current densities to generate higher magnetic field. Current is fed to the superconducting magnet, which is generally at liquid helium temperature (4K), from a power source through current leads which are connected between the magnet and the power supply at ambient. The required current may vary from few amperes for small laboratory scale magnet to thousands of amperes like LHC system. Current leads are major source of heat-inleak to any superconducting magnet system. The heat-inleak through the current lead needs to be minimized in the magnet cryostat. Hence they need cooling. Based on the cooling architecture, mode of connection and material, they are classified in different categories as described below.

4.1.1 Types of current leads

1. *Based on the cooling mode-*

    - *Conduction cooled current leads*- The conduction-cooled current leads are cooled by the conduction using refrigeration capacity of different stages of the close cycle refrigeration (CCR). The conduction-cooled leads can be thermally connected directly or indirectly with the cold heads of the CCR. The conduction-cooled current leads are mainly used for any cryogen-free magnet system (CFMS).

    - *Vapor cooled current leads*- These type of current leads are cooled by the cryogen (liquid or vapor helium and nitrogen).The vapor cooled current leads are mainly used in any bath cooled magnet system

    - *Forced flow cooled current leads*- Cooling of the current leads is done by the forced circulation of the liquid cryogen around or through them.

2. *Based on the method of connection-*

    - *Demountable current leads*- After completion of the magnet energization, these current leads can be detached from the magnet which are then operated in persistent switch mode. The demountable current leads are used in superconducting MRI, NMR systems.

    - *Fixed current leads*- These leads are in continuous use to feed the current to the magnet. They are permanently connected between the superconducting magnet and power source.

3. *Based on material used-*

    - *Metallic/alloy current leads*- These are made with different metals/alloys (Cu, brass and bronze etc.)

- *HTS (high temperature superconductor) current leads*- HTS material like BSCCO/YBCO are used for power supply purpose because of lower thermal conductivity and no joule heating when operate at DC current mode.

Now a days cryogen-free superconducting magnet systems are becoming popular in low temperature physics laboratories where no cryogen is required to cool the magnet. The concept of conduction-cooled hybrid current lead made it possible to develop the cryogen-free magnet system using the limited cooling capacity of CCR. Current leads are one of the dominant sources of heat input to any superconducting magnet systems whether it is bath-cooled or conduction-cooled system. These heat inputs are largely affects the magnet system in terms of liquid helium consumption in case of bath-cooled system and higher steady state temperature in case of conduction-cooled system. In conventional liquid helium based superconducting magnet systems, the higher heat load may be compensated by frequent refilling of liquid helium. But in case of cryogen-free or conduction-cooled system, a small thermal perturbation may cause the failure of the system in terms of quench.

The discovery of HTS materials made it possible to develop hybrid current lead for CFMS. The critical temperature of HTS is much higher than that of conventional low temperature superconductors (LTS). The critical temperature of the HTS materials like BSCCO, YBCO are well high above the boiling point temperature of liquid nitrogen. Hybrid current leads are the combination of optimized metallic (or alloy) lead and high temperature superconductor (HTS) lead. In conduction cooled hybrid current lead, an optimized metallic/alloy current lead is connected between ambient to the 1st stage of the cryocooler and HTS current lead is connected between 1st stage to 2nd stage of the cryocooler, where superconducting magnet is attached. Optimization of the metallic current leads minimize the heat load to the 1st stage of the cryocooler. HTS leads minimizes the heat load to the 2nd stage of the CCR as the HTS leads do not produce any Joule heating. The heat load comes through them is purely based on thermal conduction [17, 18, 28, 29]. The thermal conductivity and electrical resistivity of the different metals/alloys are shown in Figure 4.1 and Figure 4.2 respectively. Data for the different materials are collected from NIST, NTRS (NASA) and CAN superconductors [30-36].

Materials properties [30-36]:-

1. Phosphor de-oxidized copper; 0.027% P, 99% Cu (commercial hard temper).
2. Brass; 30% Zn, 70% Cu.
3. Phosphor bronze-CDA 510; 4.2-5.8% Sn, 0.03-0.35% P, 94-96% Cu (annealed temper).
4. OFHC Cu; 99.95% pure (annealed).
5. BSCCO $Bi_{1.8}Pb_{0.26}Sr_2Ca_2Cu_3O_{10+x}$ (2223 phase), T_c= 110K (CAN Superconductors).

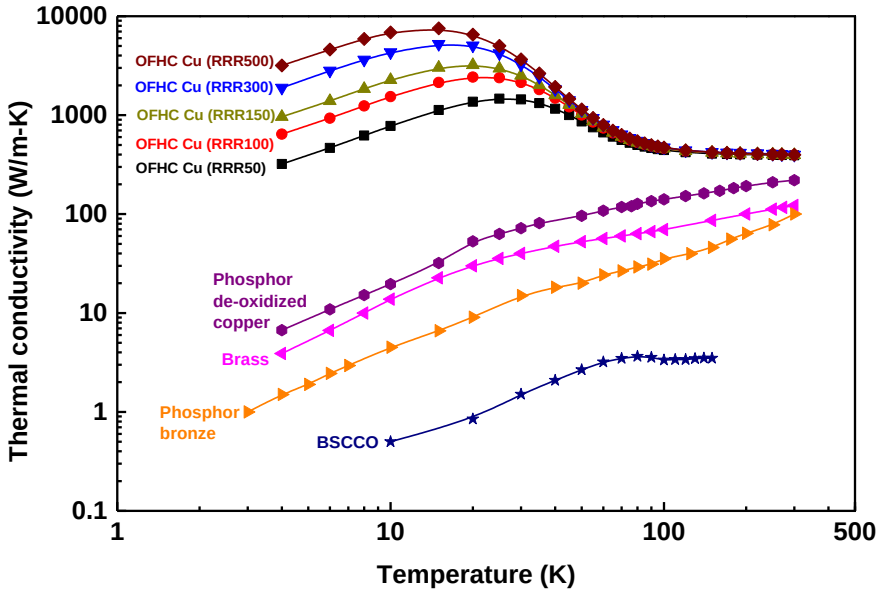

Figure 4.1. Thermal conductivity of different metals, alloys and BSCCO (HTS) material.

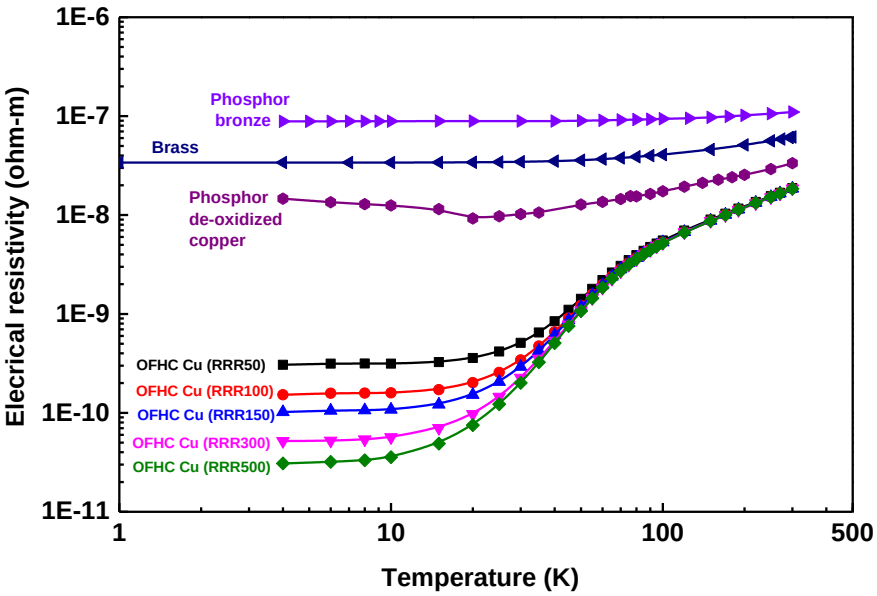

Figure 4.2. Electrical resistivity of different metals and alloys.

Figure 4.1 indicates that the thermal conductivity of the pure materials like oxygen-free high-conductivity (OFHC) copper (Cu) is much higher than the other alloys like phosphor de-oxidized copper, brass and phosphor bronze. Thermal conductivity also depends over residual resistivity ratio (RRR) of the material, which means the ratio of resistivity of material at 273K to the resistivity of material at 4K.

$$RRR = \frac{\rho_{273K}}{\rho_{4K}} \tag{4.1}$$

Higher the RRR value means higher the purity of material, so higher the thermal conductivity. Alloys have lower thermal conductivity especially at the low temperature because of having higher impurity contents. The thermal conductivity of BSCCO (HTS) is much lower than the rest of the material mentioned in the Figure 4.1. Figure 4.2 shows that electrical resistivity of the pure metals are much lower than that of alloys.

The heat flow through the conduction-cooled hybrid current lead system is schematically shown in Figure 4.3. The temperature of the 1st stage of the cryocooler remains in the range of 30-50K and this stage takes care of the heat loads which come through the optimized metallic/alloy leads. Commercial HTS current lead works between 64K to 4K. The 2nd stage of the cryocooler takes care of the conduction heat loads which come through the HTS lead.

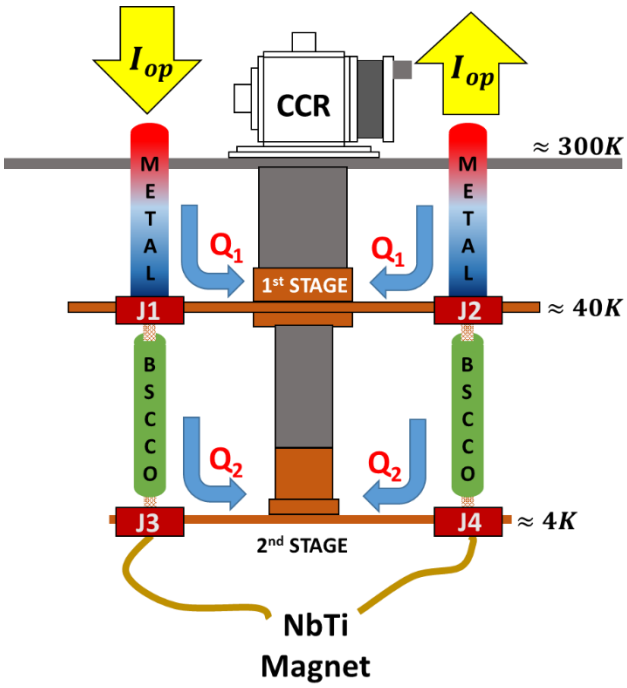

Figure 4.3. Heat flow scheme of hybrid current lead system.

The aim of current leads design is to minimize the heat load to the magnet system. In general, conduction heat load through the metallic lead can be minimized by using material having poor thermal conductivity. Similarly, the ohmic heating can be minimized by using lower resistive material for current leads. If design aspect switch towards dimensional side then lower cross sectional area and higher length of the current leads able to reduce solid conduction but increase ohmic heat loss and larger cross section area and smaller length can able to reduce ohmic heating but conduction loss increases. So the design optimization is the only criteria to select the proper area to length combination for the operating current value. Design optimization ensure minimization in both heat conduction and electrical resistance. The Wiedemenn-Franz law explain the relation between thermal conductivity and electrical resistivity of the material in the form of Eq. (4.2) which shows that thermal conductivity and electrical resistivity of the material are inversely proportional to each other.

$$k(T).\rho(T) = L_0.T \tag{4.2}$$

Where L_0 is the Lorentz number (2.45×10^{-8} WΩ/K^2), $k(T)$ is the temperature dependent thermal conductivity of material and $\rho(T)$ is the temperature dependent electrical resistivity of the material. Most of the metals and alloys obey the Wiedemenn-Franz law with the argument that there is a minimum heat leak related to the operating current, which is nearly independent of material used. So the design optimization of the current leads is not association with the material selection during optimum shape calculation [17, 18, 29].

4.2 Optimization of metallic/alloy current lead

The design optimization of the metallic/ alloy current leads is carried out through the thermal equilibrium scheme between room temperature to the intermediate temperature. The heat transfer to the cryogenic system from the metallic/alloy current leads should be minimized as this energy must be removed by a cryocooler based refrigeration system. There are optimal lead dimensions for given application that minimizes external heat transfer to the device.

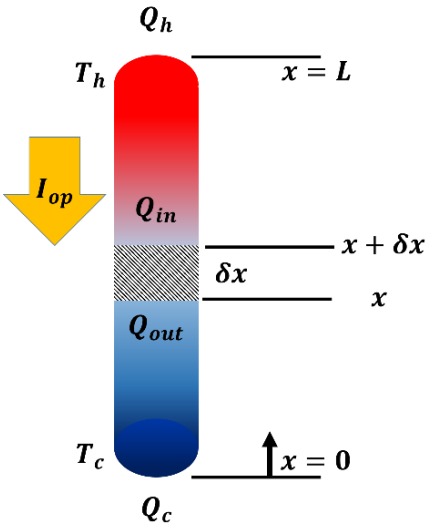

Figure 4.4. 1-dimensional heat flow model for a conduction-cooled current lead.

Figure 4.4 shows the thermal equilibrium condition of the current lead for the δx length. Here one end of the current lead is at room temperature (300K) and another end is at intermediate temperature connected with 1st stage of the cryocooler. For the thermal equilibrium condition the heat balance is given by [28],

$$Q_{in} - Q_{out} + Q_{gen} = 0 \tag{4.3}$$

So for δx length of the current lead

$$\left\{k(T).A.\frac{dT}{dx_{(x+\delta x)}}\right\} - \left\{k(T).A.\frac{dT}{dx_{(x)}}\right\} + \left\{\frac{I^2.\rho(T)}{A}\right\} = 0 \tag{4.4}$$

Here A is the cross sectional area of current lead and I is the operating current.

Eq. (4.4) can be written as,

$$\frac{d}{dx}\left\{k(T).A.\frac{dT}{dx}\right\}+\left\{\frac{I^2.\rho(T)}{\mathrm{A}}\right\}=0 \tag{4.5}$$

Suppose $$k(T).\frac{dT}{dx}=V \quad \text{and} \quad \frac{I}{A}=J \tag{4.6}$$

$$A\frac{dV}{dx}+\frac{\rho.I^2}{A}=0 \tag{4.7}$$

$$\left\{\frac{dV}{dT}.\frac{dT}{dx}\right\}+\ \rho J^2=0 \tag{4.8}$$

$$\frac{V}{k(T)}.\frac{dV}{dx}+\ \rho.J^2=0 \tag{4.9}$$

$$VdV=-k(T).\rho.J^2.dT \tag{4.10}$$

$$V=\frac{Q}{A}\rightarrow dV=\frac{dQ}{A} \tag{4.11}$$

Therefore after changing variables and integration equation becomes,

$$\int_{Q_c}^{Q_h}Q.dQ=\frac{1}{2}|Q^2|_{Q_c}^{Q_h}=-I^2\int_{T_c}^{T_h}k(T).\rho(T).dT \tag{4.12}$$

$$Q_c^2=Q_h^2+2I^2\int_{T_c}^{T_h}k(T)\rho(T)dT \tag{4.13}$$

Here Q_C is minimized when Q_h equal to zero i.e. heat load on the current lead at room temperature side (Q_h) needs to be zero and it is possible when the temperature gradient dT/dx at room temperature end is zero. So the optimum condition for a conduction-cooled current lead is,

$$Q_{c,opt}^2=2I^2\int_{T_c}^{T_h}k(T)\rho(T)dT \tag{4.14}$$

From Eq. (4.2)

$$Q_{opt}=I_{op.}\sqrt{L_0(T_h^2-T_c^2)} \tag{4.15}$$

Eq. (4.15) shows the optimum heat load for the metallic current leads based on the Wiedemenn-Franz approximation. This equation explains that optimized head load is independent of any material and it only depends on the temperatures of the both ends of the current lead. To achieve minimum heat leak per ampere operating current, the dimensional parameter of the lead needs to be optimized. If we consider temperature of the both ends 300K to 40K i.e. room temperature to cryocooler 1st stage temperature, so the optimized heat load comes around 46.5 mW/A for each current lead so for a pair of current lead, it is equal to 93 mW/A, this is the minimum operating load and it is totally independent of the material used for the current lead. The operating current for the 6T conduction cooled superconducting magnet system developed at IUAC is 102A.Hence the minimum heat input through a pair of optimized metallic current lead is about 9.8W.

For the optimized dimension of the current leads,

$$Q_{c,opt} = k(T).A.\frac{dT}{dx} \tag{4.16}$$

From Eq. (4.14)

$$\left\{k(T).A.\frac{dT}{dx}\right\}^2_{c,opt} = 2I^2 \int_{T_c}^{T_h} k(T)\rho(T)dT \tag{4.17}$$

$$dx = \left\{\frac{k(T).A.dT}{I\sqrt{2\int_{T_c}^{T_h} k(T)\rho(T)dT}}\right\} \tag{4.18}$$

If the boundary conditions are, when $x = 0\ then\ T = T_c$ and $x = L\ then\ T = T_h$, and if Eq. (4.18) is solved, using Wiedemenn-Franz approximation then

$$I_{op}.\left\{\frac{L}{A}\right\}_{opt} = \left\{\int_{T_c}^{T_h} \frac{k(T).dT}{\sqrt{L_0({T_h}^2 - {T_c}^2)}}\right\} \tag{4.19}$$

Eq. (4.19) shows that the optimized dimensions of the current leads are totally dependent on the properties of material. The optimized shape parameter $\left({}^{IL}/_{A}\right)_{opt}$ is found out for different metals and alloys using their material property data [30-36]. Figure 4.5 shows $\left({}^{IL}/_{A}\right)_{opt}$ parameters with different cold end temperature for different material.

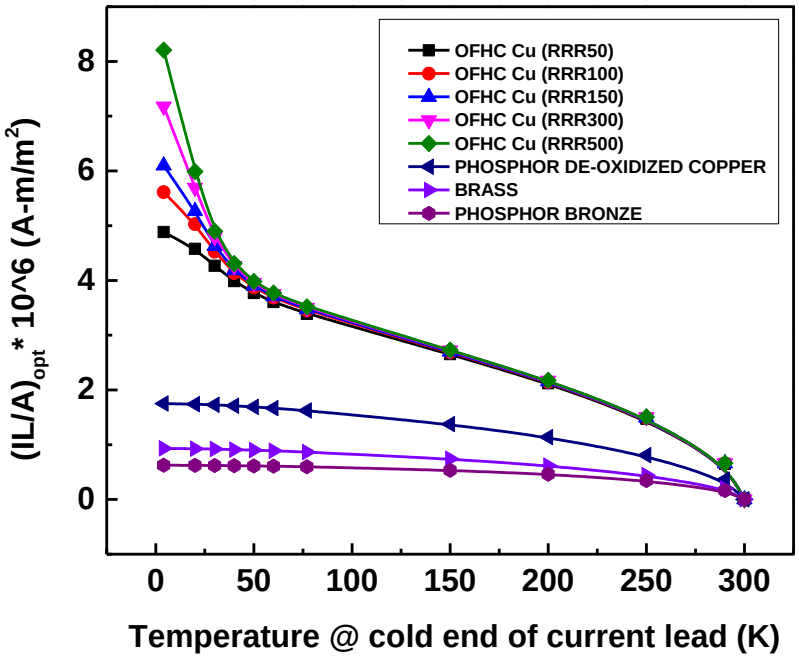

Figure 4.5. Shape parameter $\left({}^{IL}/_{A}\right)_{opt}$ of the optimized current leads for the different cold end temperature of the current lead when hot end temperature is fixed at 300K.

Figure 4.5 shows that the shape parameter for the pure metal material like OFHC copper is higher than the alloys. Shape parameter also vary with the RRR value for OFHC copper and for higher RRR value shape parameter is high. Shape parameter for the OFHC copper does not vary as much up to 50K temperature range as it varies at lower temperature side. Phosphor de-oxidized copper, brass and phosphor bronze show lower shape parameter values and among them phosphor bronze has lowest shape parameter for given temperature range. Figure 4.6 shows that for the fixed operating current 102A and fixed cross section area 15mm^2 alloys require shorter length as compare to the metals for the same cold end temperature (40K) [17, 18, 29, 37-41].

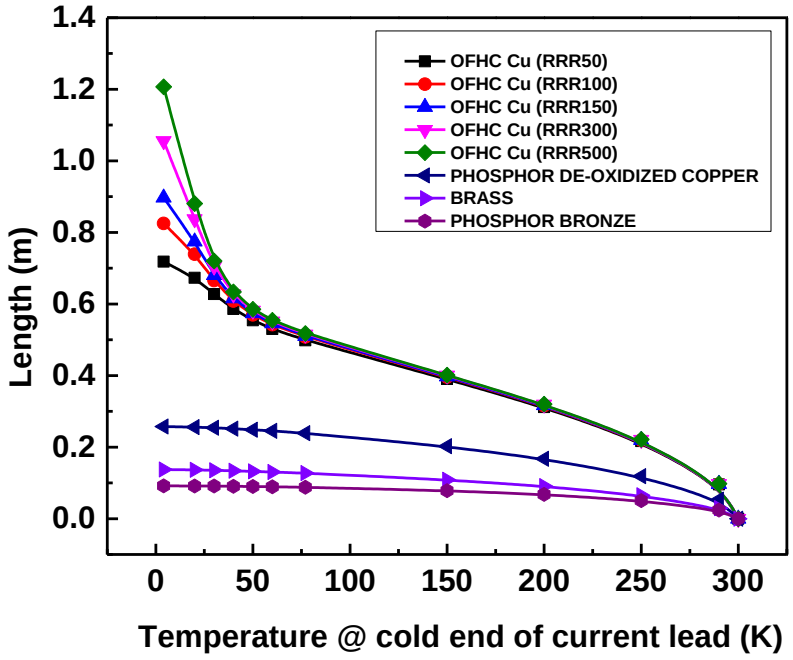

Figure 4.6. The optimized current leads lengths for the different cold end temperature of the current lead when hot end temperature is fixed at 300K at operating current of 102A and 15mm^2 cross section area.

4.3 Thermal impedance measurement of inter-lead joint of hybrid lead

Hybrid current lead is one of the important parts for the development of cryogen-free superconducting magnet system. IUAC, New Delhi has recently developed a conduction cooled 6T NbTi solenoid magnet system using two stage GM cryocooler (SRDK-415D) of refrigeration capacity of 1.5W @ 4.2K and 45W @ 50K [15, 25]. The thermal stability of the NbTi magnet is greatly dependent on the performance of the hybrid current lead. Hybrid current lead has some inter-lead joints which need to be electrically insulating and thermally conducting with the different stages of the cryocooler. Each hybrid current lead has two inter-lead electrical joints; optimized copper current lead to BSCCO (HTS) current lead joint (J1 or J2), which is thermally attached to the 1st stage of GM cryocooler, at the temperature range of ~ 40K and another joint (J3 or J4) between BSCCO (HTS) current lead and NbTi wire of solenoid magnet, which is thermally attached to the 2nd stage of GM cryocooler, at the temperature range of ~ 4K, as shown in Figure 4.3. When NbTi solenoid magnet is energized through hybrid current lead then heat load generated from hybrid current lead transfer to the respective stages of cryocooler through the inter-lead electrical joints, as shown in Figure 4.3.

These joints are perfectly electrically insulated and thermally conductive with their respective stages of the GM cryocooler. Heat load contribution from hybrid current leads to the conduction cooled magnet system is much more than that of coming from other sources of the system. The thermal stability of the NbTi magnet is greatly dependent on the performance of the inter-lead joints of hybrid current leads. Thermal contact resistance occurs when two dissimilar materials or similar material make contact to each other. In actual condition, it is impossible to make a perfect joint due to surface irregularities and when heat flows through these contacts the thermal interface resistance arises. Every surface which is appearing smooth shows the non-flatness characteristic, this non-flatness in the form of macroscopic level (voids, concavity, and convexity) or microscopic level (irregular rough contact). Surface finish of any of the material is not absolute as result of this, irregularities occur between contact surface. These contacts have very few discrete spots separated by much larger gaps. In the contact area heat flow occurs through irregularities in the vacuum conditions as shown in Figure 4.7.

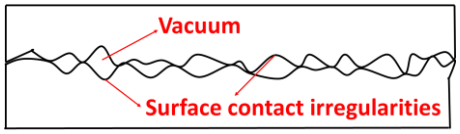

Figure 4.7. Surface contact irregularities with vacuum voids.

The inter-lead joints of the hybrid current leads have thermal contact impedance which is one of the causes of thermal instabilities in NbTi solenoid magnet system. To characterize the thermal behavior of the inter-lead joints, a thermal anchoring block has been designed and developed. Experimental measurement has been carried out at different thermal load conditions in a test cryostat. This thermal anchoring block is electrically insulated with their respective stages of the GM cryocooler by the means of different interlayer electrically insulating but thermally conductive material like Kapton (polymide) and Aluminium nitride (AlN). To enhance the surface contact area and avoid irregularities for better heat flow, some of soft interlayer materials like Indium and Apiezon N-grease can be added [42]. Thermal characteristics of the joint over the certain load and temperature range, under low temperature

and vacuum have been demonstrated in this section, and for this heat flow mechanism the thermal contact impedance of the joints is found out experimentally, between hybrid current lead and respective stages of GM cryocooler [43].

4.3.1 Test of thermal properties at the joint with different interlayer material

The thermal characteristic of the joints is the mechanism of heat flow through them. Thermal resistance developed when flow of heat occur through a thermally conductive material and it is because of the temperature differences between the two extreme surfaces of the joint. When these bodies are in contact to each other and due to their different and variable thermal conductivities, temperatures at the both ends are not same.

4.3.1.1 Insulating material characteristic

Aluminium Nitride (AlN): [44]

- Material type- Ceramic
- Chemical formula & name- AlN (Aluminium nitride)
- AlN (disc-2.5mm) Properties-

1. Thermal conductivity- 140-177 W/m-K @ 273K and 25 W/m-K @ 45K (High thermal conductivity for a ceramic material, second only to Beryllia (330 W/m-K @ 273K).
2. Specific heat- 780 J.kg/K
3. Volume resistivity- 1010 ohm.cm
4. Dielectric strength- >20 kV/mm
5. Dielectric constant- 8.6

Kapton: [45]

- Material type- Polymide
- Chemical name- poly-oxydiphenylene-pyromellitimide
- Kapton (film- 25μm) Properties-

1. Thermal conductivity- 0.12 W/mK @ 296K (ASTM F-433-77 (1987)
2. Specific heat- 1090 J.kg/K (Differential Calorimetry)
3. Dielectric strength- 7000 V (ASTM D149)

4.3.1.2 Experimental setup

Thermal impedance measurement test of the hybrid current lead joint has been conducted under temperature range of 4K-40K in a small test rig integrated with two stage GM cryocooler. In the cryostat, vacuum up to the order of 10^{-05} mbar is generated using turbo molecular pump and then GM cryocooler started. The vacuum improved up to 10^{-08} mbar due to the cryopumping by the GM cryocooler. At the 1st stage of GM cryocooler, a radiation shield of

electrolyte tough pitch (ETP) copper is attached and at the 2nd stage of GM cryocooler, other required test components are installed.

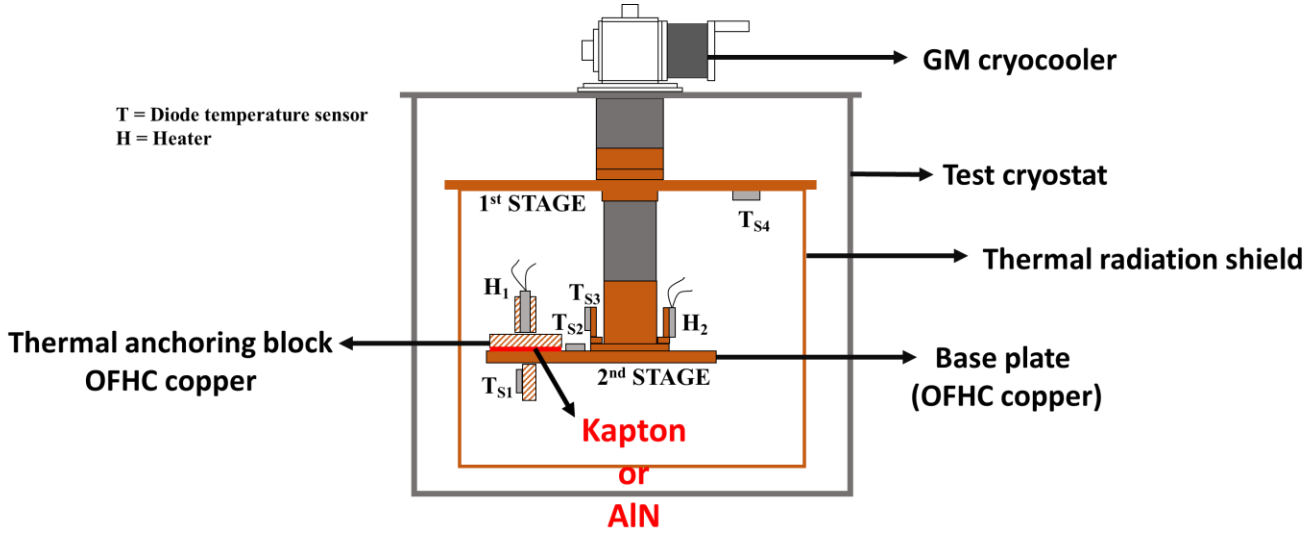

Figure 4.8. Schematic diagram of test setup.

For the thermal contact impedance measurement, a thermal anchoring block of OFHC copper over which gap is allowed for a cartridge heater (H1) of maximum capacity of 50 W and a calibrated silicon diode temperature sensor (TS1; DT-670 of Lake Shore Cryotronics) are mounted on the thermal anchoring block [46]. This thermal anchoring block is attached with the OFHC copper base plate which is directly attached with the 2nd stage of GM cryocooler. The H1 heater would simulate the heat flow, coming from the hybrid current lead, passing through the inter-lead thermal joints. Another calibrated silicon diode temperature sensor (TS2) is attached on the base plate. This base plate and the thermal anchoring block are separated to each other by the mean of interlayer electrically insulated but thermally conductive materials, as shown in Figure 4.8. AlN and Kapton have been used as electrical insulator. Hence there are two types of thermal joints under consideration. One would be copper-AlN-copper or Cu-AlN-Cu interface and another would be Cu-Kapton-Cu interface. In Cu-AlN-Cu joint, Indium is used as soft interface material to fill voids and avoid surface irregularities. Similarly in Cu-Kapton-Cu joint, cryogenic grade Apiezon N- grease is added to fill the voids and avoid irregularities at interface. Apiezon N- grease instead of Indium can also be used in Cu-AIN-Cu interface.

To vary the temperature of the 2nd stage of GM cryocooler in the range of 4K-40K, a heater (H2=50W) is installed directly at 2nd stage along with a calibrated silicon diode temperature sensor (TS3), as shown in Figure 4.8. Current/voltage source meters are used for supplying power to the heaters. Agilent-B2911A source meter and Kepco bipolar operational power supplies are respectively used for H1 and H2 heaters. Figure 4.9 shows the block diagram of experiment with auxiliary test instruments. Figure 4.10 shows the internal view of the test rig where the thermal anchoring block is mounted on the 2nd stage cold head of the GM cryocooler.

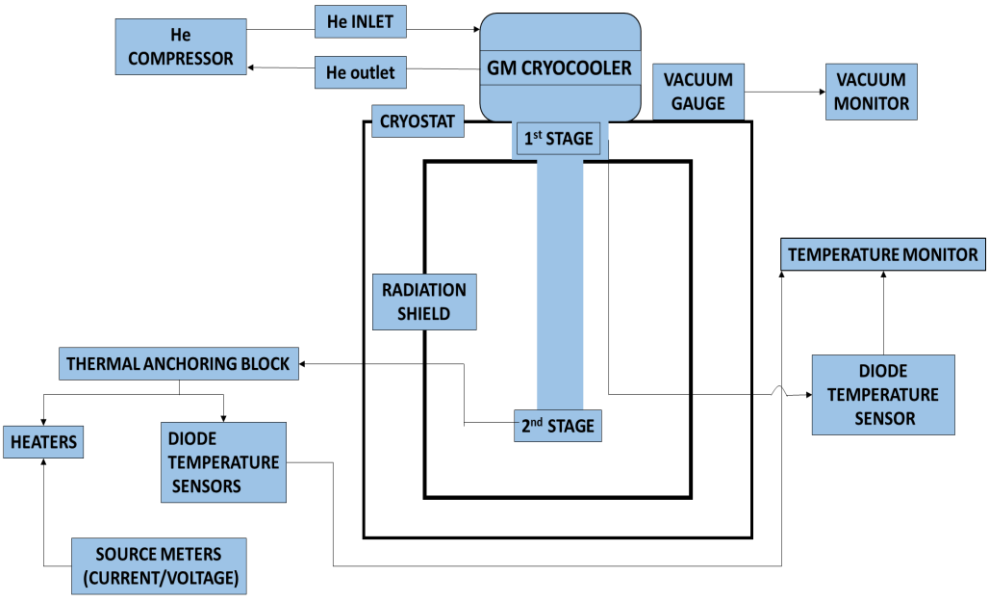

Figure 4.9. Block diagram of test setup.

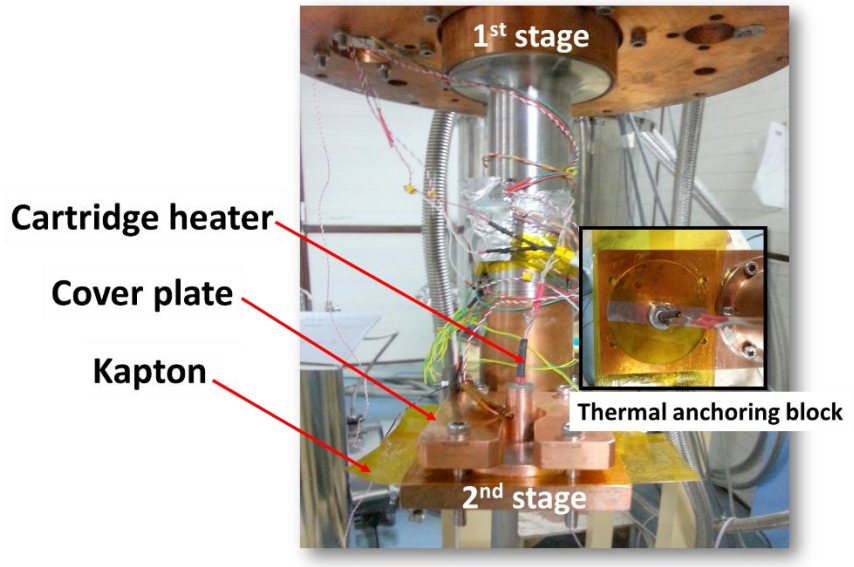

Figure 4.10. Internal view of test set up.

4.3.1.3 Experimental terminology

- *Thermal resistance (R_t)* – Thermal resistance is an empirical property, which is derived from the analogy between electrical and thermal conduction. It is defined as the resistance generated during the heat flow through the contact interface of solid bodies [47-50]. The thermal resistance (R_t) for any thermal joint can be estimated using relation which is given by,

$$R_t = \frac{T_{S1} - T_{S2}}{Q} \tag{4.20}$$

Where Q (W) is the amount of heat flow through the contact interface; T_{S1}-T_{S2} (K) is the temperature difference between two contact surfaces.

- *Thermal impedance (Z_t)* – Thermal impedance is defined as the temperature gradient per unit of heat flux passing through the interface [47]. The thermal impedance (Z_t) for any thermal joint can be estimated using relation which is given by,

$$Z_t = \frac{T_{S1} - T_{S2}}{Q} . A = A . R_t \tag{4.21}$$

Where A (cm^2) is the contact surface area of the joint.

- *Thermal conductance (C_t)* – Reciprocal of the thermal impedance is known as thermal conductance [47-50]. Thermal conductance is given by,

$$C_t = \frac{1}{Z_t} \tag{4.22}$$

4.3.1.4 Test procedure

In this experiment, joints of thermal anchoring block and OFHC copper base plate with different interlayer electrically insulating but thermally conductive materials like Kapton and Aluminium nitride, have been made. For avoiding irregularities, Apiezon N- grease is used with Kapton interlayer joint and Indium is used with Aluminium nitride interlayer joint as shown in Figure 4.11.

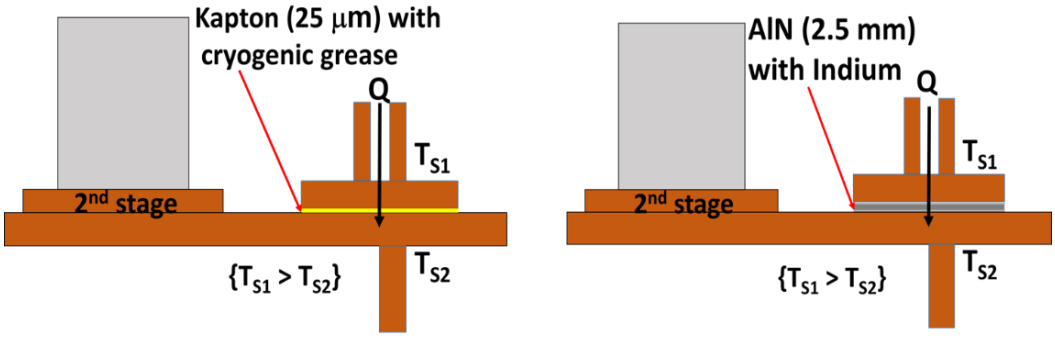

(a) (b)

Figure 4.11. Thermal anchoring block and base plate (a) Cu-Kapton-Cu joint, (b) Cu-AlN-Cu joint.

For the measurement of the thermal contact impedance –

Sample-1: Cu-Kapton-Cu, Thermal anchoring block with Kapton + Apiezon N-grease.

Sample-2: Cu-AlN-Cu, Thermal anchoring block with Aluminium nitride + Indium.

1. Sample-1 has been mounted on the base plate which is attached with 2nd stage of the GM cryocooler. After cool down of the sample-1, once equilibrium temperature reached, then known amount of heat (~100 mW) has been given to the heater H1 to find out the temperature difference between TS1 and TS2 across the sample-1. The corresponding thermal resistance (Eq. 4.20) and thermal impedance (Eq. 4.21) of that base temperature has been estimated using the amount of heat given to the H1 heater and the temperature difference between TS1 and TS2.

2. Temperature of the base plate raised by supplying power through heater H2, once equilibrium temperature reached then repeat the previous step for the thermal resistance and thermal impedance estimation of that raised temperature.

3. This process has been followed till 40K and covered 4K-40K temperature range with intermediate temperatures 4K, 6K, 10K, 15K, 20K, 30K and 40K.

4. Similar process has been followed for sample-2 to estimate the thermal resistance and thermal impedance for same temperature range (4K-40K).

4.3.2 Measurement and analysis

Figure 4.12 shows comparison of the thermal impedance of the sample-1 and sample-2. Thermal impedance of sample-1 and sample-2 is highly dependent on the temperature and it decreases as the interface-temperature increases.

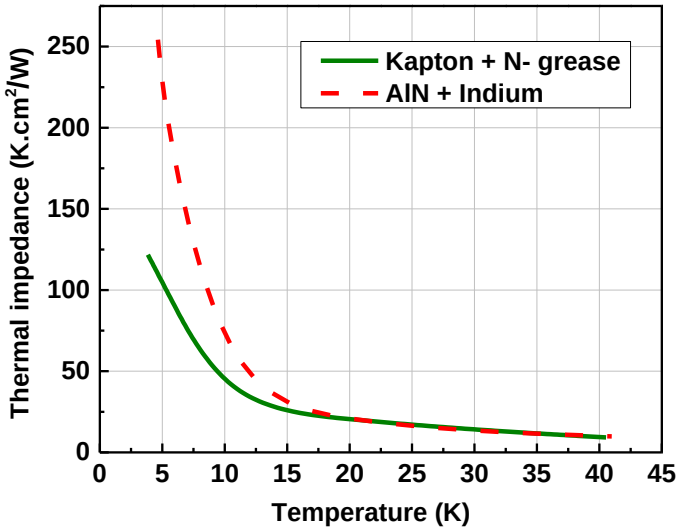

Figure 4.12. Thermal impedance v/s temperature of Cu-Kapton-Cu and Cu-AlN-Cu interface.

At 4 K temperature range, the values of thermal impedance significantly differ from each other for Cu-Kapton-Cu and Cu-AlN-Cu though the surface contact area (~19 cm^2) is same for both

joints. Cu-Kapton-Cu interface shows lower thermal impedance (~122 K.cm^2/W) than that of Cu-AlN-Cu interface (~255 K.cm^2/W). Thermal impedance of both type of interfaces decreases at higher temperature. At the 40K temperature, the thermal impedance for both Cu-Kapton-Cu interface and Cu-AlN-Cu interface become almost equal (~11 K.cm^2/W). Figure 4.13 shows the corresponding variation of thermal resistance for both types of interfaces. The trend shown in Figure 4.13 also indicates that beyond 40K, the thermal resistance of the Cu-AlN-Cu interface may be lower than that of the Cu-Kapton-Cu interface.

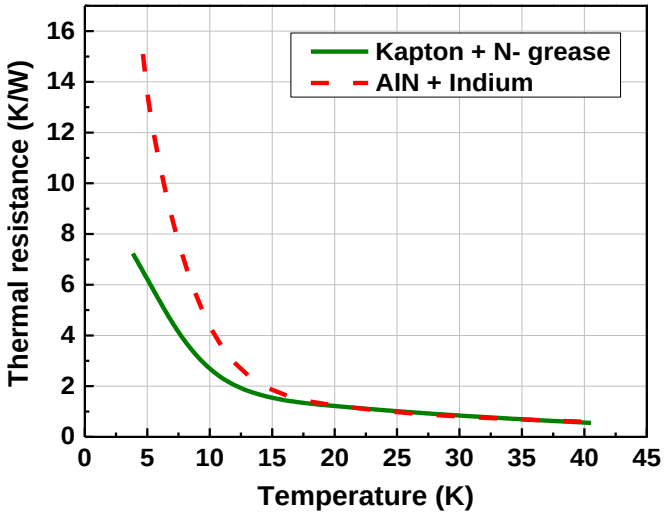

Figure 4.13. Thermal resistance v/s temperature of Cu-Kapton-Cu and Cu-AlN-Cu interface joint.

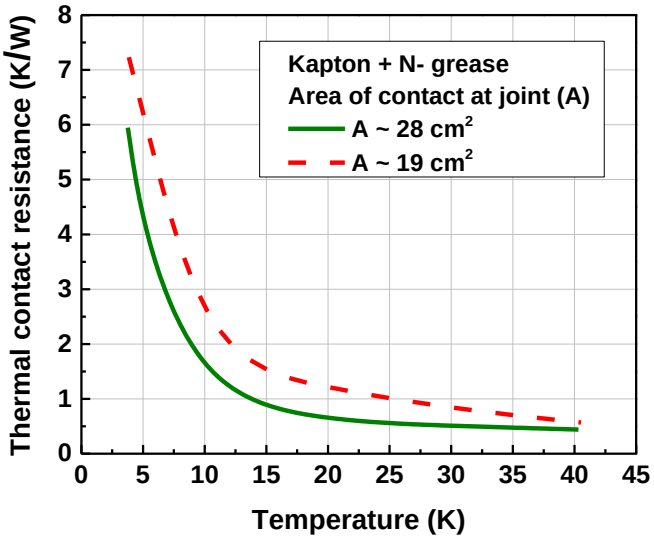

Figure 4.14. Thermal resistance v/s temperature of Cu-Kapton-Cu for two different contact area.

Figure 4.14 shows that the thermal contact resistance of the Cu-Kapton-Cu interface is dependent on surface contact area and decreases with increment of surface contact area. The thermal resistance at 40K is ~ 0.6 K/W whereas it is ~ 6-7 K/W at 4K. At 4K temperature range, thermal resistance is found to be dependent on the contact area but it diminishes at 40K

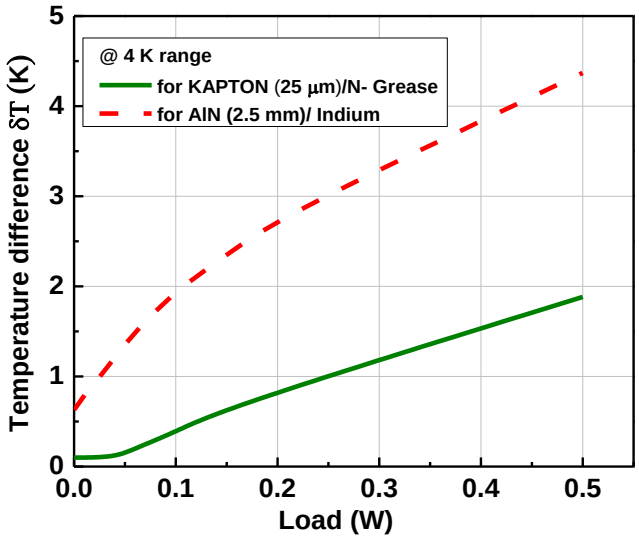

Figure 4.15. Temperature difference (T_{S1}-T_{S2}) v/s heat load of Cu-Kapton-Cu and Cu-AlN-Cu interface at 4K temperature.

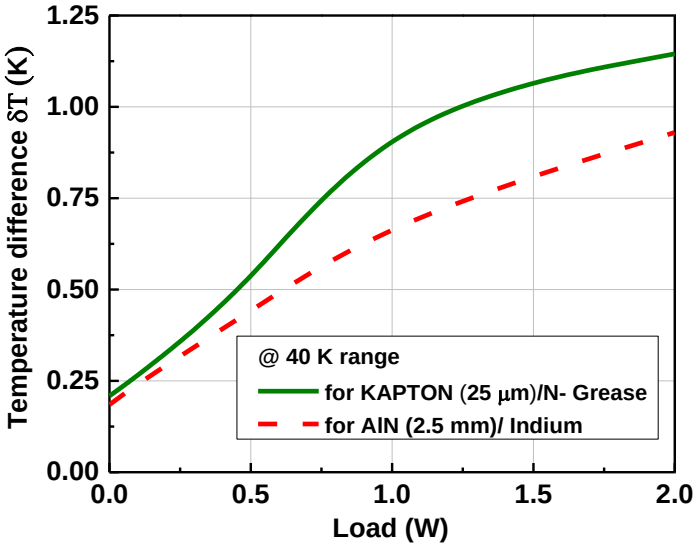

Figure 4.16. Temperature difference (T_{S1}-T_{S2}) v/s heat load of Cu-Kapton-Cu and Cu-AlN-Cu interface at 40K temperature.

temperature range because of Kapton material shows high conductance at 40K temperature range.

Figure 4.15 and 4.16 show, if heat load increases at both of Cu-Kapton-Cu and Cu-AlN-Cu interfaces then temperature difference (T_{S1} – T_{S2}) also increases, which is clear indication of thermal resistance increment, because thermal resistance is directly proportional to the temperature difference. So at the 4K joint with Cu-Kapton-Cu interface shows the lower values of thermal resistance compare to 4K joint with Cu-AlN-Cu interface. Similarly in the 40K joint with Cu-Kapton-Cu interface shows the higher values of thermal resistance compare to 40K joint with Cu-AlN-Cu interface.

This experiment is conducted with Kapton and Aluminium nitride (AlN) as interlayer electrically insulated but thermally conductive material and found out that Cu-Kapton-Cu interface have lower thermal impedance values then Cu-AlN-Cu interface. Hence Kapton may be better at 4K thermal joint but at 40K or beyond, AlN would be better. Contact surface area of the inter-lead joint also affect the thermal resistance and thermal resistance decreases with increment of contact surface area.

4.4 ANSYS heat flow analysis of hybrid current lead

As discussed in the section 4.2 that for the optimized current leads, alloys have lower shape parameter for the particular temperature range than metals. This section is based on discussion over the thermal behavior of the metallic/alloy lead at their operating current, over-current and under-current operation. To find out this characteristic, having lower thermal conductivity and enough electrical resistivity, phosphor de-oxidized copper is selected. This section also explained a brief discussion over the maximum temperature for different metals/alloys during over-current operation.

4.4.1 Thermal profile of the optimized phosphor de-oxidized copper current lead

The operation of the conduction-cooled optimized metal/alloy current leads for the cryogen free superconducting magnet is based over the temperatures of the cooling stages of the cryocooler. As discussed earlier that phosphor de-oxidized copper has lower thermal conductivity at lower temperature so it allows lower thermal load to the system. Phosphor de-oxidized copper is an alloy of phosphorous and copper (0.027% P, 99% Cu, commercial hard temper) and over it thermal analysis has been done on the ANSYS thermal-electrical simulation software [51], for finding out under-current and over- current behavior when current lead has been chosen for its optimized length for the fixed operating current and cross section area. Shape parameter; $\{I.L/A\}$, of the phosphor de-oxidized copper current lead when the operating temperature range is 40K at 1st stage temperature of the GM cryocooler, to 300K at room temperature is 1.71037E06 A.m/m^2. So for the cross section area (A) 15 mm^2 and 102A operating current (I_{op}) optimized length (L_{opt}) of the current lead is 0.25m. Figure 4.17 shows that the under, over and optimum current operation results for the phosphor de-oxidized copper current lead. In this figure the ratio of conductor current to the operating current $\left\{I/I_{op}\right\}$ is set at different values like; 0, 0.3, 0.5, 0.7 and 0.9 for the under-current operation and 1.1, 1.2, 1.3, 1.4 and 1.5 for the over-current operation, to analyze the behavior of the current lead. X- co-ordinate of the Figure 4.17 shows the ratio of length of the point of interest in x-direction to the optimized length of the current lead i.e. $\left\{x/L_{opt}\right\}$. When current lead is carrying zero current then there is no electrical load but temperatures of the current lead at both the sides are not same so this temperature difference allows to flow heat through current lead and due to this thermal conduction maximum heat flux of the order of 2.05E05 W/m^2 is there at the minimum temperature side of the current lead i.e. 40K end. At operating current 102A operation, both electrical as well as thermal loads are there in the current leads but as optimized condition described that temperature gradient $\left\{dT/dx\right\}$, at the hot end side of the current lead, become zero so there is no conduction heat load at the hot end side which means $Q_h = 0$, so the remaining heat loads are only because of resistive heating. Maximum heat flux for the

optimized condition comes out around 3.416E05 W/m^2 at 40K end. Figure 4.17 also indicates that when current lead is operating at under-current and optimized current operation then the maximum temperature is always equal or lower than the room temperature. But when current lead is operating at over-current range then overheating occurs at certain position of the current lead which is in between the cold end and hot end of the current lead. This thermal peak comes in picture because of over-current operation and this over-current causes excessive joule heating. At 153A current which is 1.5 times the optimized current, the maximum temperature comes around 339.04K at the 0.07m away from the 300K end side and maximum heat flux at 40K is 5.48E05 W/m^2.

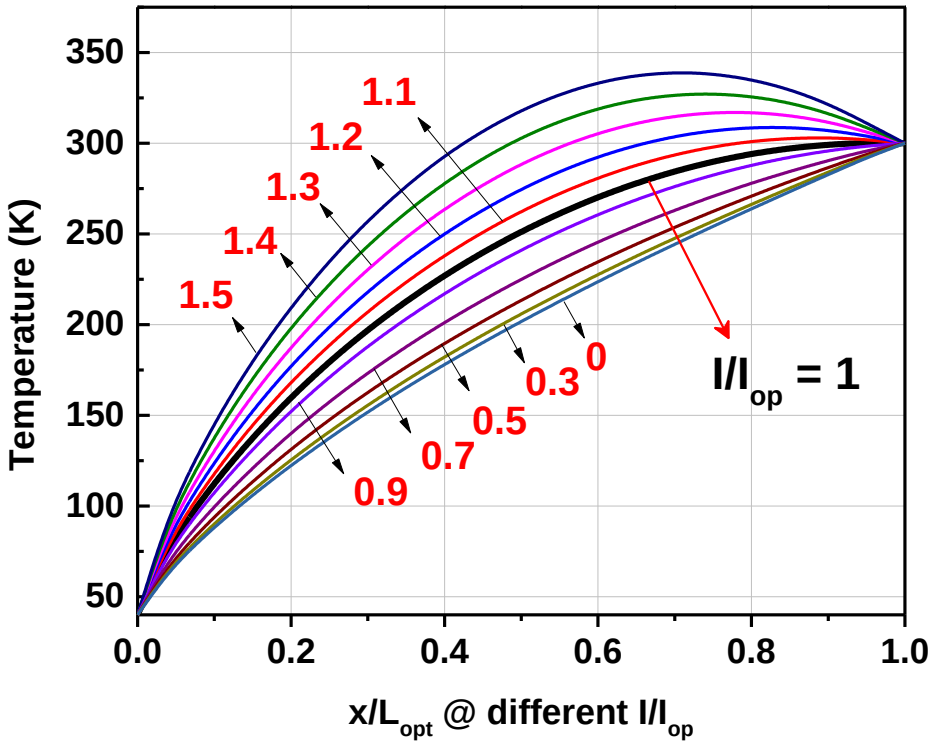

Figure 4.17. Thermal profile of the optimized phosphor de-oxidized copper lead for under-current, optimized current and over-current operation.

As mentioned earlier that if there will be an intermediate thermal peak at over-current operation, there will be reverse heat flow from thermal peak to the ambient. The heat would flow to both side of the lead from the thermal peak where heat flux is zero. This zero heat flux zone is the indication of the overheat loads at this zone. As the value of current increases, the shifting pattern of the zero heat flux zone is towards cold end temperature side (40K) of the current lead. Figure 4.17 also shows that as the operating current increases beyond optimized current, the temperature of the intermediate peak also increases which effectively increases the heat flow to the cold end of the lead. Figure 4.18 shows the ANSYS 3D graphics of heat flux and temperature distribution simulation of the optimized current lead, operating at different currents. It also shows the heat flux shifting pattern at under-current and over-current operation and temperature profile with maximum temperature point in the current lead.

❖ $I/I_{op} = 0$

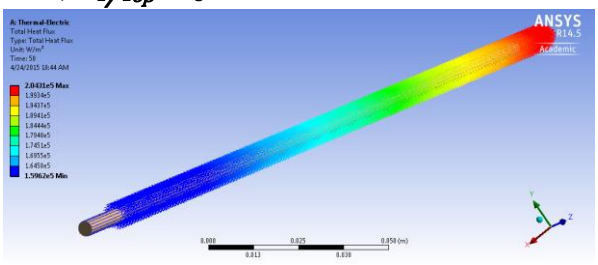

(a)

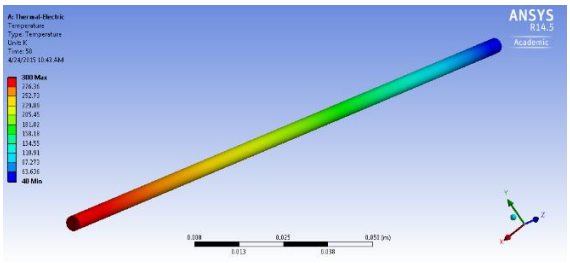

(b)

❖ $I/I_{op} = 0.3$

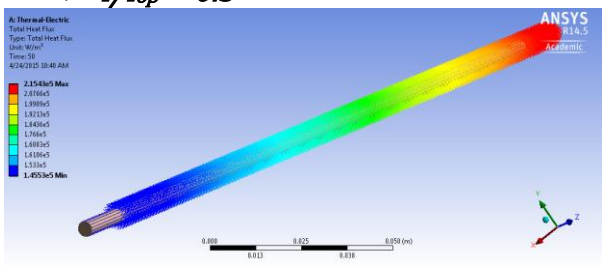

(a)

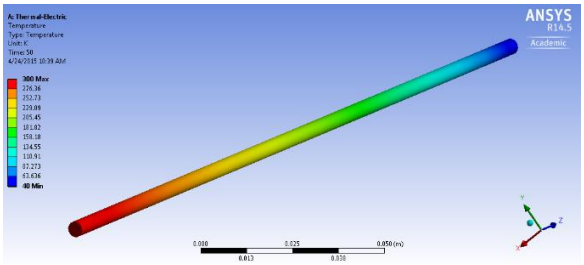

(b)

❖ $I/I_{op} = 0.9$

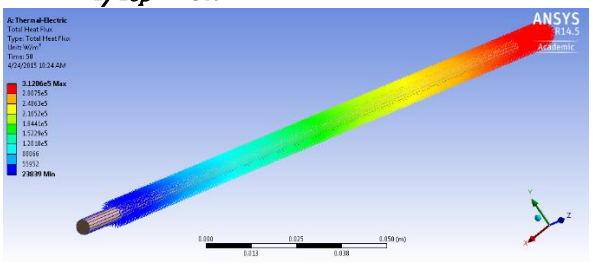

(a)

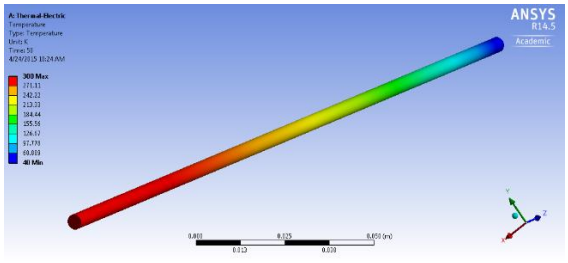

(b)

❖ $I/I_{op} = 1$

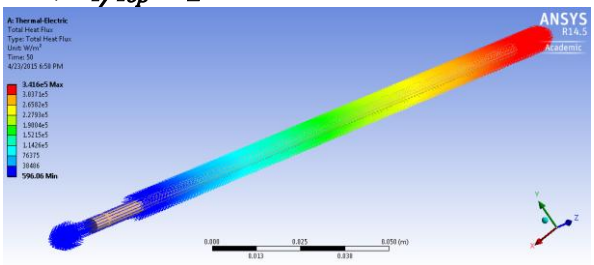

(a)

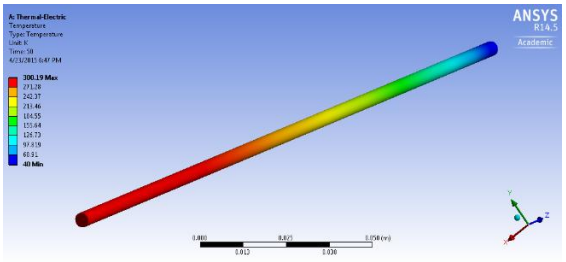

(b)

❖ $I/I_{op} = 1.1$

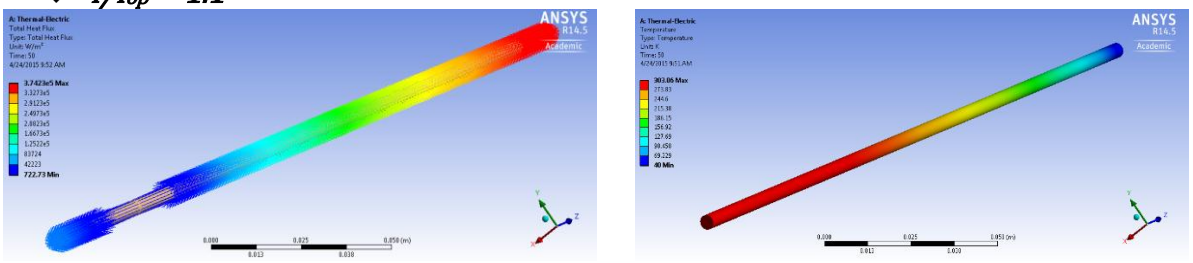

(a) (b)

❖ $I/I_{op} = 1.3$

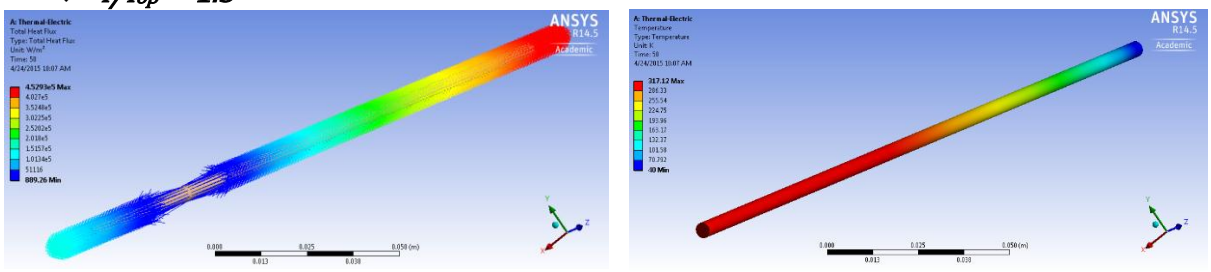

(a) (b)

❖ $I/I_{op} = 1.5$

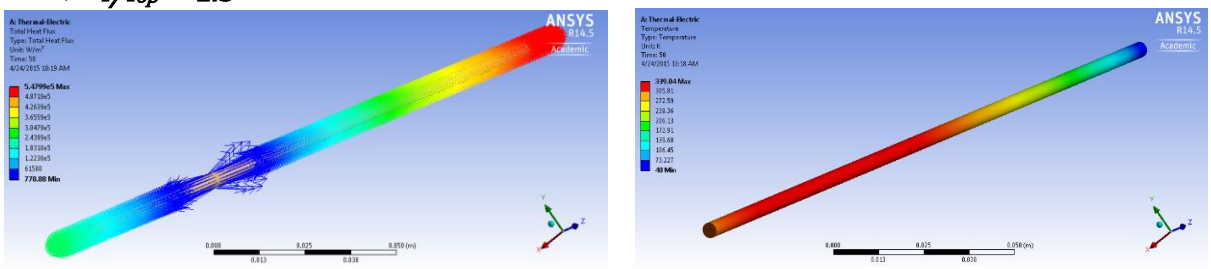

(a) (b)

Figure 4.18. ANSYS 3D graphics of optimized current lead operating at under, over and optimized current (a) represent heat flux graphics and (b) represent temperature distribution graphics.

When current lead is operated at its operating current value $\left\{I/I_{op} = 1\right\}$ then as per optimization condition of current lead the maximum temperature is the room temperature only so that zero thermal gradient allows zero heat flux from ambient. But in simulation results maximum temperature overshoot the value i.e. 300.2 K at the distance 0.01m from the 300K end, as shown in Figure 4.18. It indicates that the operating current value is little less for this optimization condition or this error comes in results because of material property data has taken for simulation.

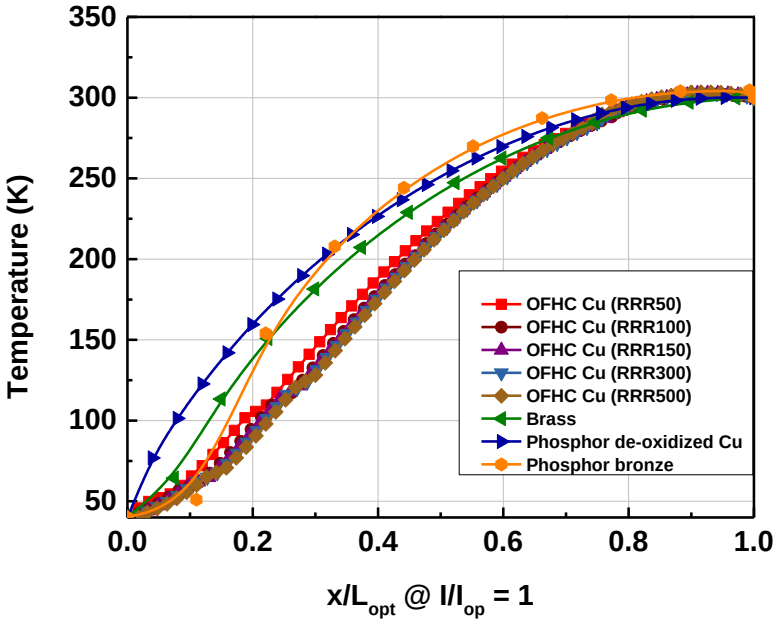

Figure 4.19. Thermal profile of the current leads made with different materials with respect to their optimized length at operating current (I_{op} = 102A).

Figure 4.19 shows the temperature distribution for the optimized length of current lead operating at $\frac{I}{I_{op}} = 1$. For the same length parameter $\left\{\frac{x}{L_{opt}}\right\}$ alloy shows higher temperature distribution as compare to the metals. There are different shape parameters for the current leads made with different materials for the fixed operating temperature range i.e. 40K – 300K, so they have different optimized lengths as mentioned below in Table 4.1.

Table 4.1 Shape parameter of current lead for the different material with optimized length.

No.	Material used	$\left\{I.L/A\right\}_{opt}$ (A-m/m^2)	L_{opt} (m) @ $I_{op} = 102$A; $A = 15$mm^2
1	OFHC Copper (RRR50)	3.8858591E06	0.586
2	OFHC Copper (RRR100)	4.13557E06	0.608
3	OFHC Copper (RRR150)	4.183757E06	0.615
4	OFHC Copper (RRR300)	4.26384E06	0.627
5	OFHC Copper (RRR500)	4.30817E06	0.633
6	Phosphor de-oxidized copper	1.71037E06	0.251
7	Brass	0.9101817E06	0.134
8	Phosphor bronze	0.616388E06	0.090

As Table 4.1 shows that shape parameter reduces as impurity content increase in the material. For phosphor bronze shape parameter is 0.616388E06 where as for OFHC Cu (RRR500), shape

parameter is 4.30817E06 that means phosphor bronze material current lead require less length (0.090m) as compare to OFHC Cu (RRR500) current lead length (0.633m), when the cross section area (15mm^2) and operating current (102A) are fixed.

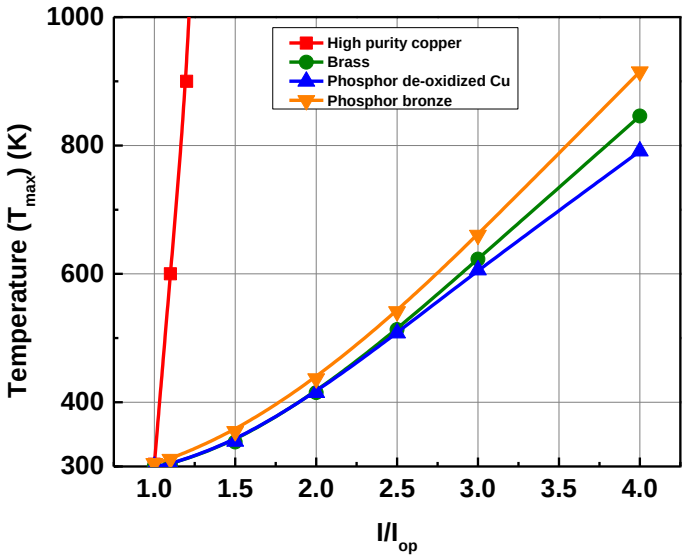

Figure 4.20. Maximum temperature as a function of over- current for different materials for current lead [18].

Temperature of the optimized length current leads overshoot from room temperature (300K; hot end side of current leads), when they operate at over-current. Figure 4.20 shows the maximum temperature rise for different materials with respect to different over-current operation. If the pure material current lead which is optimized for known operating current then very small amount of excess current can cause severe damage to the system. In Figure 4.20 high purity copper current lead has maximum temperature rise above 1000K when it operates around 1.2 times of the operating current [18] whereas other materials have lower temperature rise as compare to pure OFHC copper (RRR500). The maximum temperature rise for the phosphor bronze, phosphor de-oxidized copper and brass are 915K, 790K and 850K respectively, when the $^{I}/_{I_{op}} = 4$.

5.

QUENCH ANALYSIS OF 6T CONDUCTION COOLED NbTi MAGNET

5.1 Introduction

5.2 Temperature and current margin for quench

5.3 Classification of quench

5.4 Causes of quench

5.5 Quench protection

5.6 Finite element quench analysis using OPERA electromagnetic 3-D simulation software

5.7 Experimental quench study of 6T NbTi solenoid magnet

5.1 Introduction

Quench is an event which is originated in superconducting coil, and due to its propagation, normal zone causes current decay in the coil. Basically quench is a superconducting to normal transition specifically rapid irreversible process in which magnet is driven fully normal. Any of the current carrying conductor the stored electromagnetic energy in the form of $^1/_2 LI^2$. During quench process, all stored electromagnetic energy converted into the form of heat. Heat generated during quench never spread uniformly in the coil and it can lead to destruction of the device, if it is not properly protected. Quench initiation occur in the form of point source generally and then spread to all around the coil by the process of ohmic heating and thermal conduction. At the same time, resistance of the normal zone grows sufficiently high that causes current decay in the conductor. At the point source where quench has been initiated, the temperature at that particular region goes very high. Figure 5.1 shows the sequence of events in case of quench.

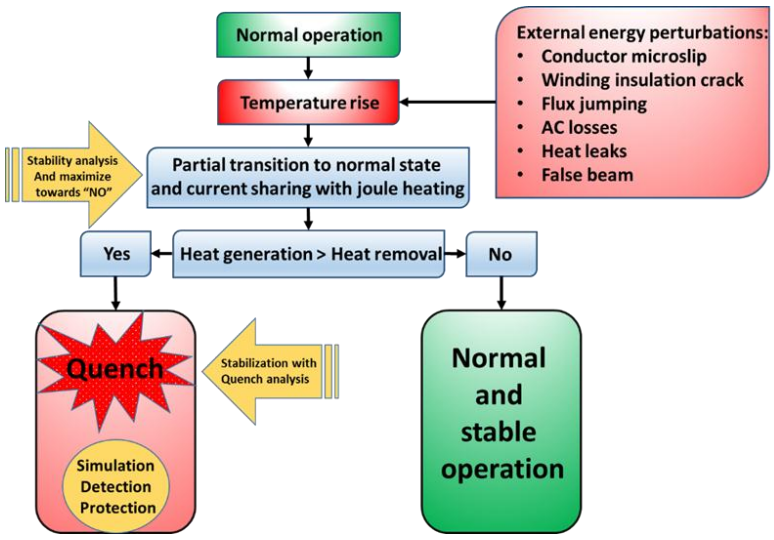

Figure 5.1. Flow chart of quench.

Magnetic stored energy density of a magnet is,

$$E' = \frac{B^2}{2.\mu_0} \tag{5.1}$$

So if there is a 5T magnet then the stored energy density is equal to ~ 10^7 J/m^3 and for 10T magnet ~ 4×10^7 J/m^3. Magnetic stored energy is,

$$\int_v E'.dv = E = \frac{1}{2} LI^2 \tag{5.2}$$

This stored energy is converted to heat through Joule heating (RI^2). If this process happened uniformly in the coil then there is no harm. For an example, Cu melting point temperature is 1356 K and corresponding magnetic stored energy density is,

$$E' = \rho C_p dT = h_{Cu}(1356K) - h_{Cu}(4K) \tag{5.3}$$
$$= 5.2 \times 10^9 \text{ J/m}^3$$

so the value of magnetic field is about 115T and the limit is about $B_{max} \leq 115$T, which means no problem but the process does not happen uniformly and as little as 1 % of mass can absorb almost total energy.

There are three types of catastrophic failures occur during quench; 1) overheating of the conductor, 2) overstressing of the coil magnet, 3) high voltage arcing. Temperature rise at the time of quench may be sufficient to harm the insulation or even melt the conductor because sometime it cross the melting point temperature of the conductor material. Energy concentration is very high at particular location of the coil during quench and recovery period allows to generate stresses and deform the magnet coil. If temperature rise did not harm the conductor much, then large potential difference of thousands of volts developed at the normal zone and may cause arcing between the turns and even burnt out the current leads or coil.

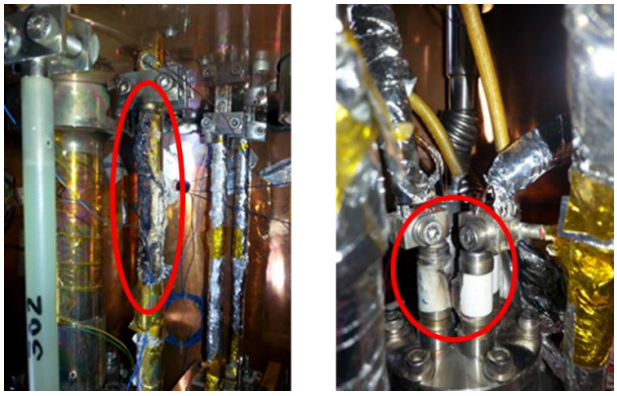

Figure 5.2. (a) Burnt HTS current lead of superconducting quadrupole magnet system (IUAC, New Delhi) due to quench. (b) Arcing at the current lead terminals of superconducting quadrupole magnet system (IUAC, New Delhi) due to high voltage during quench.

Generally, superconducting magnets are operated at the temperature range which is well below the critical temperature of the superconductor and related to its critical field and critical current density of the conductor. If there are some disturbances during operation then operation becomes instable and these instabilities can generate nasty effects. At low temperature range the specific heat of the superconductors is very low so they can't sustain energy, ultimately temperature rises. During the superconducting magnet operation, energy of the order of mJ or μJ level can able to rise the temperature of the magnet. Specific heat of NbTi at 4.2K is nearly about 10^{-4} J/g-K and if this heat remain within the hot region and do not flow out of it, then for 1g of NbTi with 1mJ of energy, the temperature rises to 14.2K, which is higher than the critical temperature of NbTi. In typical applications, this temperature rise is considerably over the maximum temperature margin and the magnet will eventually quench. If the heat is distributed in the whole magnet and assume the mass is equal to 1000g, the temperature rises to just 4.21K which is much less than the critical temperature of NbTi, hence there will be no quench. But non-uniform distribution of heat happens and quench begins at a

point and then spreads in the conductor by the process of ohmic heating and thermal conduction [17, 18, 52, 53].

5.2 Temperature and current Margin for quench

Superconducting magnets are operated with certain temperature and current margin. These margins are basically evolved from the 3-dimensional critical surfaces of the superconductors. During quench process, superconductor overcome these temperature and current margins and allow itself to become normal.

Figure 5.3 and 5.4 indicate the temperature and current margin for superconductor operation for a desired field value. There are limiting values of temperature and current for field value, so for superconducting magnet operation, we provide operating parameters which ensure some level of margin under which device works normally. If devise crosses margin due to some reasons then operation becomes instable.

Here I_c = Critical current, I_{op} = Operating current, B_c = Critical field at given temperature, B_{op} = Maximum operating field at operating current, B_{max} = Maximum field at critical current, T_{op} = Operating temperature, T_{cs} = Current sharing temperature and T_c = Critical temperature at given field.

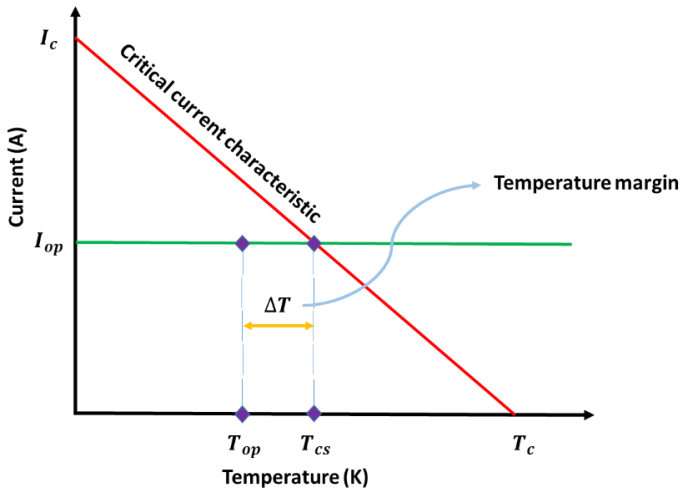

Figure 5.3. Temperature margin to quench.

If temperature rise is caused by any of the disturbances then temperature margin is provided by cooling modes. These cooling modes maintains the magnet temperature as low as possible to raise the temperature margin $\Delta T = T_{cs} - T_{op}$, as shown in Figure 5.3 and if temperature crosses this margin then magnet will quench. For the desired field value, critical current density of the superconductor decreases almost linearly with increment of temperature. Here, if magnet operates at operating current less than critical so temperature margin is generated.

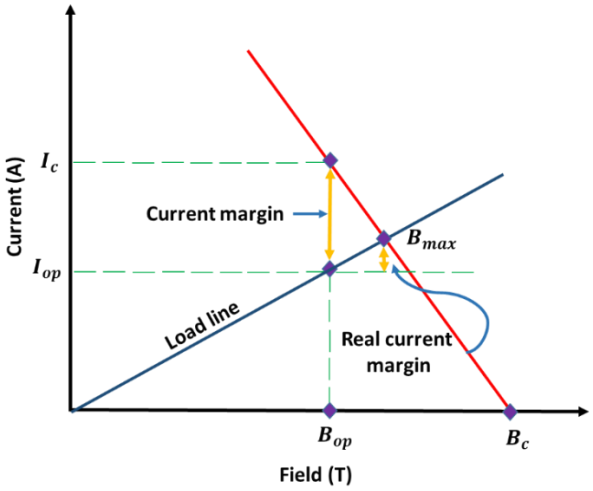

Figure 5.4. Current margin for quench.

Figure 5.4 shows that operating current value is much lower than the critical current value and this gap provides current margin. To ensure the safe operation of the devise, the peak field load line can't cross the critical current margin otherwise magnet will quench.

Practical operation always requires margin. In general critical current margin: $I_{op}/I_{quench} \approx 50-70\%$, critical field margin: $B_{op}/B_{quench} \approx 75\ to\ 85\ \%$, margin along the load line: $I_{op}/I_{max} \approx 85\ \%$ and temperature margin: $T_{cs} - T_{op} \approx 1\ to\ 2\ K$ [52, 54, 55].

5.3 Classification of quench

5.3.1 Based on the operating current limitation

At operating temperature T_{op} of the conductor reaches at maximum current i.e. $I_{max} = I_c\ (B_{max}, T_{op})$, then magnet quenches either at $I_{quench} = I_{max}$ or $I_{quench} < I_{max}$. If $I_{quench} = I_{max}$ then it is known as conductor-limited quench. Then if I_{max} is $I_c\ (B_{max}, T_{op})$ then short-sample quench occur. If $I_{max} < I_c\ (B_{max}, T_{op})$, degradation is said to have taken place. If a quench occur at $I_{quench} < I_{max}$, it is due to an energy release within the coil which increases the conductor temperature enough for quench. This kind of a quench is called as energy-deposited quench or premature quench (schematic diagram represented at Figure 5.5) [52, 53].

5.3.2 Based on disturbance spectrum and concentrated on quench origin [18]

		Space	
Time		Point	Distributed
	Transient	Joules	Joules/m^3
	Continuous	Watts	Watts/m^3

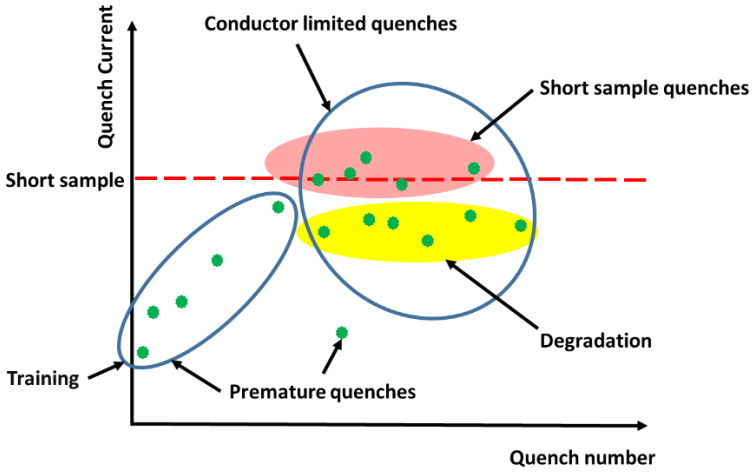

Figure 5.5. Schematic represantation of various types of quench.

5.4 Causes of quench

5.4.1 Mechanical events

5.4.1.1 Wire motion under Lorentz force

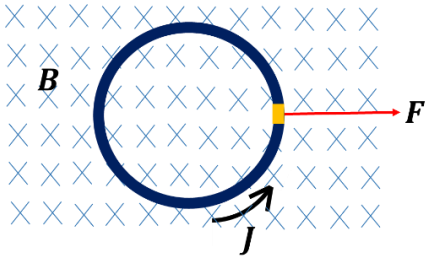

Figure 5.6. A single turn of solenoid magnet with a current density J exposed to the field B of the magnet. The resulting Lorentz force F, is directed outward.

For superconducting magnets, current density J and the magnetic field B are extremely high, so magnetic forces become also very high $(F = J \times B)$, as shown in Figure 5.6. Magnet behaves like a pressurized cylinder under these forces. Due to these induced forces, movement of the conductor, known as micro slip of winding and deformations failures happen. These processes release frictional energy and as discussed earlier that specific heat of NbTi at 4.2K is very low that can raise the temperature of the NbTi magnet beyond its critical temperature at that magnetic field. Thus to restrict the movement of winding the magnet is impregnated with epoxy resin [17].

5.4.1.2 Winding deformations and failures (at insulation bonding, material yield)

Winding of the superconducting magnet is a tricky task and it is quite impossible to make it up to the standard micron level accuracy. Problem related to micro slip has been tackled by the impregnation of the coil with some resin or wax material, these filling materials allow to cover the winding voids and help to successfully reduce the wire movement. Filler materials are in contact with the metal body and cracks are generated in these organic materials because of

stored elastic strain energy. When cracks occur then this strain energy dissipated heat which is one of the cause of temperature rise [18].

5.4.2 Electromagnetic events

5.4.2.1 Flux-jumping

The thermal disturbance in the superconductors which is caused by the flux motion. These flux motion causes heat generation and at a certain level when flux density becomes unstable then these additional magnetic flux causes flux jumping. Flux jumping now a days is a solved problem by making the conductors in fine filament form embedded in to the metal matrix, as shown in Figure 5.7.

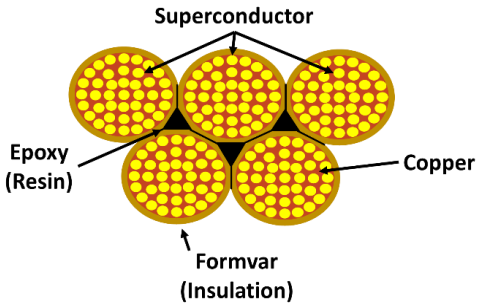

Figure 5.7. Filaments of superconductor are embedded in matrix of normal metal.

Commercial superconductors are therefore manufactured in the form of filamentary composites. The fine filaments of superconductor are embedded in a matrix of normal metal; copper is usually prefer because copper have high thermal conductivity and electrical conductivity and also have good ductility. The environment of the superconductor influences the stability especially if they are embedded in copper matrix which acts as perfect heat sink.

5.4.2.2 AC loss (most magnet types)

When conductor is subjected to changing magnetic field then electromotive force is generated within the conductor which induce current density beyond its critical value and also allow to flow flux in resistive zone and create the losses so AC losses are simply resistive heating losses. When carrying dc currents below critical current superconductors have no loss but, in AC fields, all superconductors suffer losses.

5.4.3 Thermal events

Current leads, instrumentation wires heat leaks through thermal insulation, degraded cooling

During charging of the magnet current leads contribute huge amount of load through joule heating as well as thermal conduction, which in simply one of the cause of thermal disturbances. Also instrumentation wiring and thermal insulation can able to generate heat through thermal conduction. To avoid these events proper calculated heat load distribution is carried out with optimized current lead design, critical thickness of thermal insulation and conductive heat load through wires [55].

5.4.5 Concept of minimum propagating zone (MPZ)

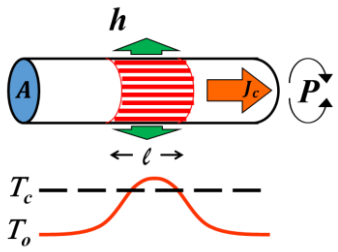

Figure 5.8. A current carring conductor heated at small length ℓ.

Quench propagation in the superconducting adiabatic magnet coil generally have two processes, which are electrical and thermal. The moving source for the normal zone is joule heating that is controlled by the electrical circuit of the magnet system. Once the magnet quenched then resistance occur in the electrical circuit is controlled by the thermal circuit of the winding. So for the propagation zone a small length l has been considered of superconductor wire, which is in adiabatic condition (thermal insulation). The wire is heated by some disturbances from its original temperature to value above T_c. The Figure 5.8 shows the schematic arrangement of minimum propagation zone and corresponding temperature profile of the superconductor. The heat generated at the particular point and propagate longitudinally in both the direction. If heat is conducted out of the resistive zone faster than it is generated, the zone will shrink otherwise vice versa it will grow and This means that the conductor quenches. The boundary between these two conditions is known as the minimum propagating zone (MPZ). So for better conduction of the generated heat, make MPZ as large as possible [17, 18].

5.5 Quench Protection

Protection is always necessary for safe and controlled operation of the superconducting magnet otherwise it suffers with multiple threats like insulation breakdown, melting of the superconductor wire and also mechanical strains in coil. So for the safety of the superconducting magnet, a protection system is required. Quench Protection arrangement takes care of magnet in all possible quenches. Quenching of superconducting magnet cannot be stopped completely whatever precaution one takes during magnet designing and fabrication. If quench happens, the magnet needs to be protected using efficient protection system.

5.5.1 External dump resistor

One of common protection systems is to provide a parallel by pass path of the magnet to decay the current. A dump resistor parallel to the magnet provide by pass path for the current. So when magnet quenches some part of stored magnetic energy will dump in to the resistor instead of fully dumping in to the magnet. Figure 5.9 shows the schematic of a simplest quench protection circuit.

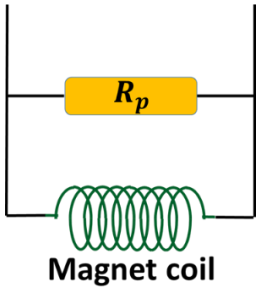

Figure 5.9. Magnet coil with parallel external dump resistor.

The limitation of the dump resistor protection method is that there is continuous dissipation of heat on the dump resistor during magnet charging and discharging because of the charging/discharging voltage $(-L.dI/dt)$. In bath cooled magnet system, the heat dissipation on dump resistor will evaporate liquid helium. To reduce this heat dissipation, back to back diodes are placed in series with the dump resistor, as shown in Figure 5.10. The forward voltage of the diode restricts the unwanted heat dissipation during charging or discharging of the magnet. In back-to-back diode scheme, the current will start flowing through the bypass resistor only when the voltage across resistor crosses the threshold level of voltage determined by the forward voltage of the diode.

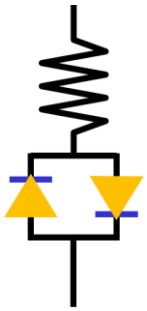

Figure 5.10. Back to back diode scheme.

5.6 Finite element quench analysis using OPERA

5.6.1 Definition

Finite element discretization process allows to form the simulation environment and *QUENCH* program (transient thermal analysis program) in OPERA electromagnetic 3-D simulation software simulates quench in a superconducting magnet. It gives model for transient thermal and electromagnetic fields. It also adds heat sources and magnetic fields produced by conductors driven by time varying circuit currents. *QUENCH* program is designed specifically for quench condition of the superconducting magnet coil when it became resistive.

QUENCH program able to solve three systems simultaneously-

• Thermal analysis, which uses heat generated from joule heating by operating current. This estimation given by electromagnetic analysis and critical current in the superconducting coil which depends on the magnetic field.

• Electromagnetic analysis which uses thermal conductivities which vary as a function of the temperature and estimated by the thermal analysis.

• Current flow in the circuit path.

QUENCH program is used for finding out the temperature distribution in a superconducting magnet during "quench". As discussed earlier quenching is the term applied to the behavior of a superconductor when it converts from its superconducting state to its resistive state. Quench can happen for one or more of the following reasons-

• The temperature of the superconductor rises beyond its critical temperature.

• The superconductor experiences a high magnetic field, above its critical magnetic field.

• The current density in the superconductor exceeds its critical value.

Superconducting materials are bad electrical conductor when they are in the normal state. For this reason, the wire in a superconducting coil is generally made of superconducting filaments embedded in a metallic matrix. This allows a low electrical resistance path for current that was being carried by the zero resistance superconductor which is tends to the quench [27].

In this section, quench analysis of 6T cryogen free superconducting magnet developed by IUAC, New Delhi, has been discussed, which consists a solenoidal magnet made with NbTi superconducting wire embedded into copper matrix. This coil is connected to an external resistor protection circuit. The temperature rise and quench is initiated by an intentionally provided heat source to the coil magnet then resistive heating will start in coil magnet [15].

5.6.2 Physical model

5.6.2.1 6T Superconducting solenoid Coil

The 6T superconducting solenoid coil can be modelled using the pre-defined conductor primitives. Thermal modelling of the magnet requires a finite element mesh. Further conductor primitives can be converted in to the meshable volumes for this circuit element. *QUENCH* program is a thermal solver which allow to solve only solid bodies. The solenoid coil is used in three ways:

• Transient thermal analysis can be found out with meshed volumes.

• The magnetic field of the coil can be found out by defining the magnet as the Biot-Savart conductor.

• The transient currents can be found out for coil winding in a circuit.

5.6.2.2 6T superconducting solenoid coil design parameter

Table 5.1. Solenoid coil parameter.

Inside radius (cm)	Outside radius (cm)	Half length (cm)	Mesh size	Size factor
5.2	**6.83**	**10**	**1**	**0.2**

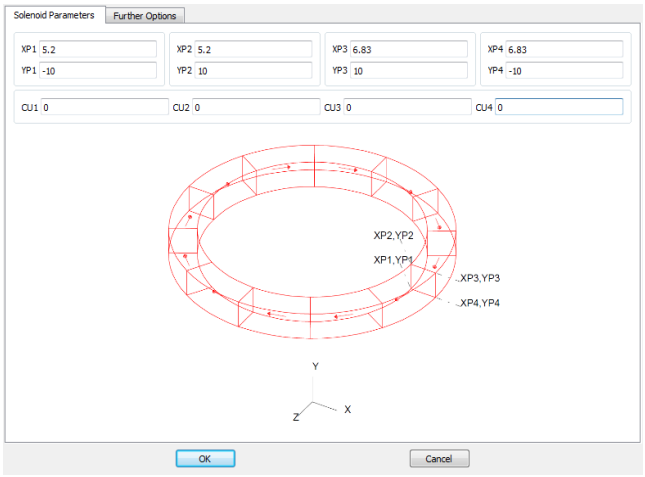

(a)

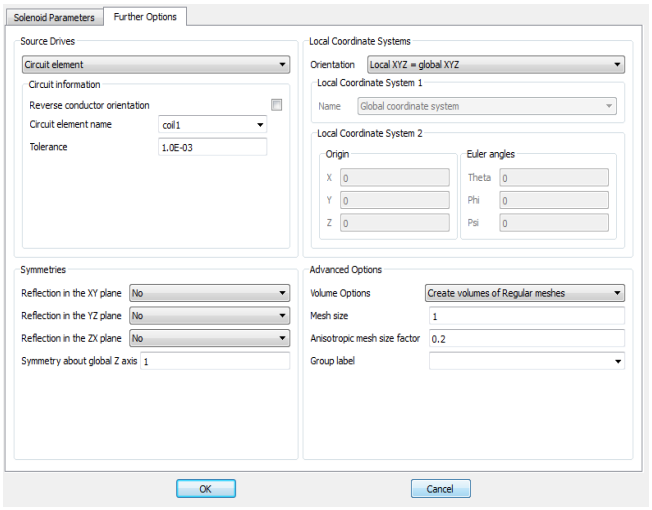

(b)

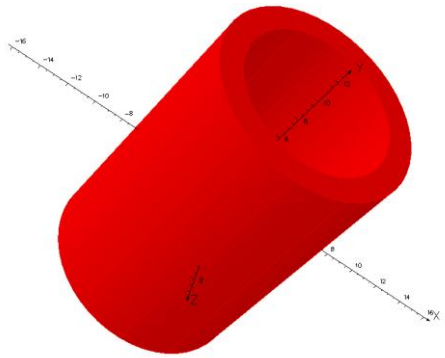

(c)

Figure 5.11. (a) Solenoid conductor dimentions, (b) Circuit element defination with co-ordinate system and advance mesh options, (c) 6T solenoid magnet coil.

Figure 5.11 shows the coil parameters. Once conductor modelling has been completed then set the analysis type to be *QUENCH*. This will configure the dialogs of the *model* menu (symmetry, material properties, boundary conditions etc.).

Finite element analysis provides great degree of freedom to solve the problem with symmetry, here only a quarter of the coil is modelled to reduce the computation time. Reflections on XY and ZX co-ordinate planes are applied. After creation the model body and view the effect of the symmetry settings. Now only a quarter of the coil remains in the model, as shown in Figure 5.12. The conductor is now have material label of coil1, so that material properties can be applied to the conductor.

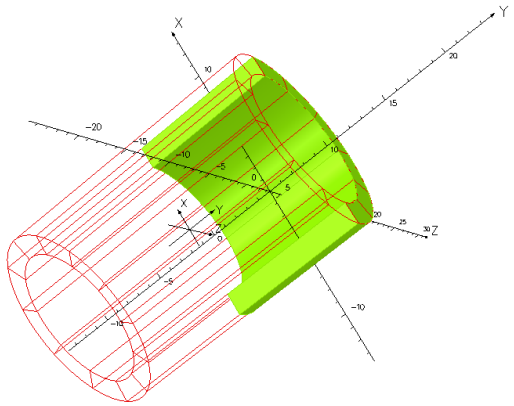

Figure 5.12. Coil model body with symmetry at XY and ZX co-ordinate.

5.6.3 Material property data

Material properties and wire geometry can be submitted to the opera modeler with *user defined variables* and *user defined functions*.

Some of the *user defined functions* are predefined within the *QUENCH* program which are defined both in SI and cgs units. These *user defined functions* are-

Table 5.2. User defined functions.

File name	Function	Description
NbTi_Cpn_v2	NbTi_Cpn(T)	Heat capacity of NbTi in normal state
Cu_Cp_v2	Cu_Cp(T)	Heat capacity of copper
Bulk_Kappa_r_v2	Bulk_Kappa_r(T)	Radial thermal conductivity of bulk materials
Bulk_Kappa_z_v2	Bulk_Kappa_z(T)	Axial thermal conductivity of bulk materials
Cu_Kappa_v2	Cu_Kappa(T)	Thermal conductivity of copper
Cu_Sigma_v2	Cu_Sigma(T)	Electrical conductivity of copper
NbTi_Jc_v2	NbTi_Jc(T;B)	Critical current density of NbTi with respect to temperature and magnetic field.

Material properties are described by *user defined variable*. Some of them are constant and some are in parameter form which depends over *user defined functions* and constant variables.

Table 5.3. User defined variables.

Name	Type	Expression/Value	Description
#NbTiFac	Constant	0.333	NbTi factor
#CuFac	Constant	0.667	Copper factor
#NbTiDen	Constant	8.5	Mass density (NbTi)
#CuDen	Constant	8.92	Mass density (Cu)
#BulkDen	Constant	#NbTiFac * #NbTiDen + #CuFac * #CuDen = 8.78014	Density of bulk materials
#BulkCp	Parameter	(NbTi_Cpn(T) * #NbTiFac * #NbTiDen + Cu_Cp(T) * #CuFac * #CuDen) / #BulkDen = 5.978×10^{-5}	Bulk heat capacity

5.6.3.1 Quench material properties

- Thermal conductivity

Nonlinear *anisotropic thermal conductivity* properties are defined by three expressions which dependent over the functions Cu_Kappa(T), Bulk_Kappa_r(T) and Bulk_Kappa_z(T). Thermal conductivity of the bulk material at radial direction is mainly decided by the copper factor. It is assumed that copper thermal conductivity is significantly higher than NbTi in this direction.

- Mass density

The mass density of the bulk material is defined in *transient thermal property* section, where copper and superconductor ratio is described. Mass densities are put in constant form and this is expressed as #BulkDen = #NbTiFac * #NbTiDen + #CuFac * #CuDen.

- Specific heat capacity

The nonlinear heat capacity of the bulk material is described by the *user defined variable*, #BulkCp, which is developed with functions, Cu_Cpn(T) and NbTi_Cp(T) and expressed as-

#BulkCp = (NbTi_Cpn(T) * #NbTiFac * #NbTiDen + Cu_Cp(T) * #CuFac * #CuDen) / #BulkDen

- Electrical conductivity

Electrical conductivity of the wire is defined in nonlinear form with tabulated function and *user-defined variable* and expressed as Cu_Sigma(T) * #Cufac.

- Wire cross-section

The wire has a cross-sectional area of 1.9625E-07 m^2.

- Critical current

The critical current is expressed in the form of, NbTi_Jc_v2 (T;B) * 1.9625E-07 * #NbTiFac.

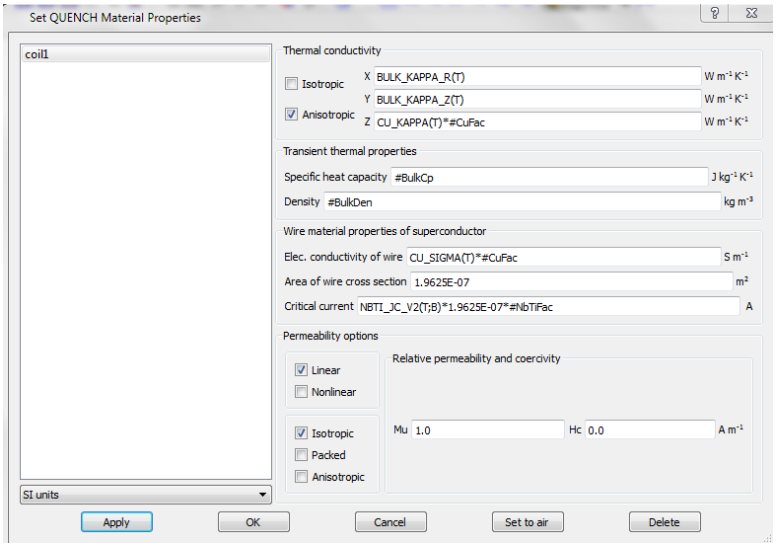

Figure 5.13. Quench material properties for the conductor.

5.6.4 Boundary conditions and protection circuit

5.6.4.1 Quench heat source

Quench initiation is done with the *heat flux* boundary condition. For the quench a heat source model is defined within a range which cover a small area over which heat is concentrated for a appropriate period of time and due to this heat flux thermal disturbance occur in the coil structure. In this study, three functional ranges are multiplied together in order to limit the extent of the heat source by time (between 0 and 0.1 second) and position (X axis at -5.2 and -5.4; Y axis at 0 and 0.2). The 4W heat source is applied for 0.1 second at the start of the analysis to initiate the quench (100 W/cm^2 over 0.04 cm^2). In the heat flux definition, negative sign indicates that the heat is entering in to the solenoid. For the heat source, one of the face is selected with *Face Properties* and define the Boundary condition label is *filmheater*. Then boundary condition is defined in *QUENCH boundary condition data* i.e.,

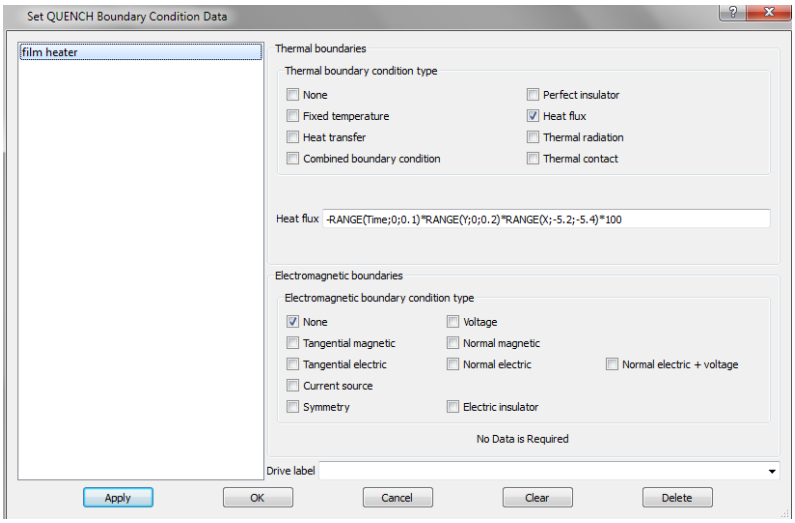

Figure 5.14. Quench heat source definition in OPERA.

5.6.4.2 Magnet protection system

The quench protection circuit needs to be modelled to start analysis . This circuit define the path of current flow during quench. For 6T cryogen free superconducting magnet system a dump resistor is added parallel to the coil, as shown in Figure 5.15.

Table 5.4. Quench protection circuit (CKT1) parameters for the magnet coil.

Name	Initial Current	Resistance	Turns	Inductance	Symmetry
R1		**5 (Ω)**			
coil1	**102 (A)**		**10700**		**4**
coil1:coil1				**5.5 (H)**	

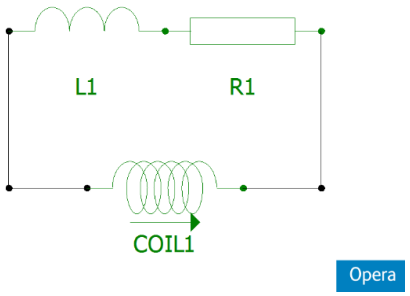

Figure 5.15. Quench protection circuit -CKT1.

5.6.5 Quench simulation environment

5.6.5.1 Quench analysis data

QUENCH program provide flexibility to start quench initiation. During quench analysis nonlinear material properties are updated at each and every time-step.

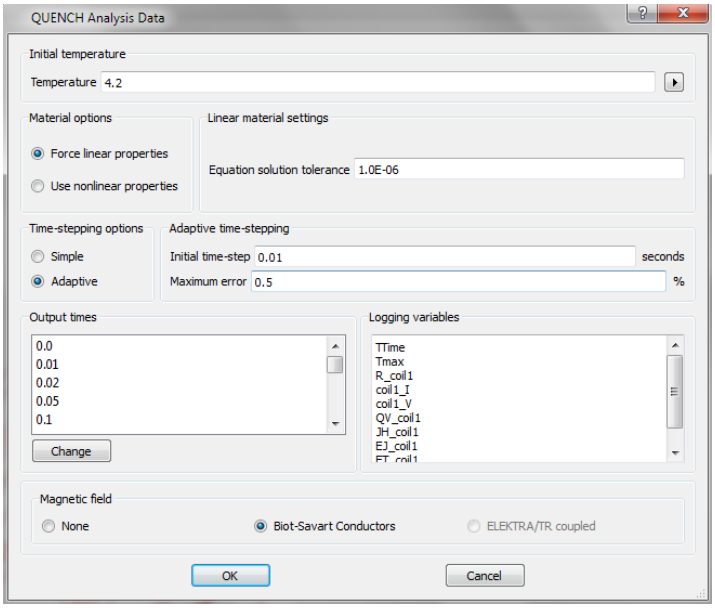

Figure 5.16. Quench analysis data definition with adaptive time stepping.

For this problem, adaptive time stepping with initial time step is 0.01 seconds with maximum error 0.5 percent. Logging variables give output characteristic of the system. Quench analysis data definition with adaptive time stepping is mentioned in Figure 5.16.

5.6.5.2 Analysis database

6T quench analysis database has been created with defining the surface meshing with mosaic form and volume meshing with absolute tolerance level of the order of 1.0E-06. Linear surface elements follow adaptive time stepping and after iteration give thermal characteristic of the magnet system.

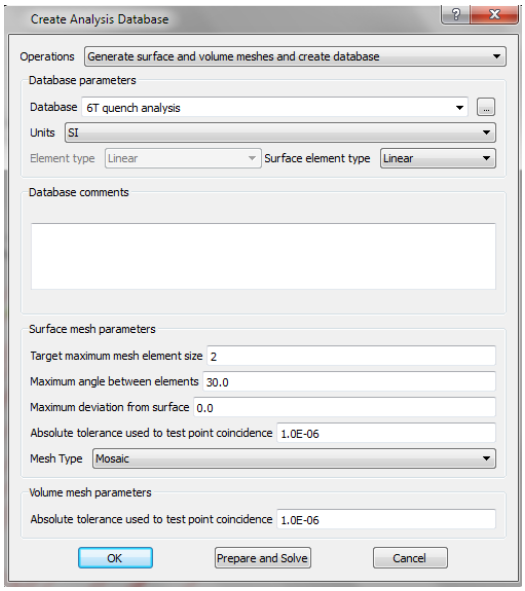

Figure 5.17. Quench analysis database.

5.6.6 *QUENCH* program post processor, results and discussion

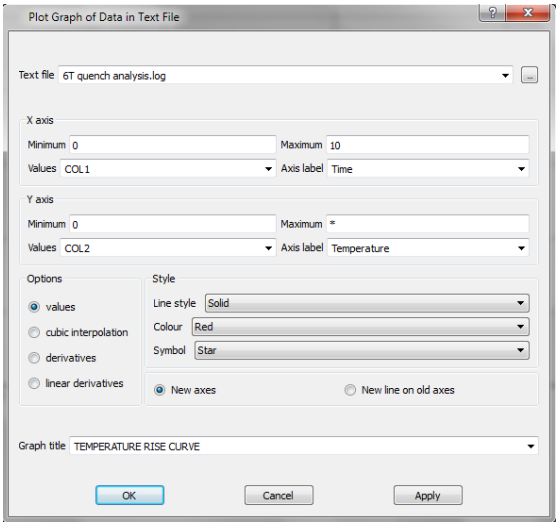

Figure 5.18. Window for the quench result data presentation through graphs.

QUENCH program post processor starts from the opera manager or through the solver window. Then select operation menu with surface label, full model symmetry is selected, this operation will display full geometry of the coil with a selected time simulation data. Then after it 3D display menu is selected.

5.6.6.1 Resistance rise, Temperature rise, current decay and internal voltage during quench

Quench is started intentionally by applying heat flux which evolves normal zone and it expands with time. The temperature rising pattern is ranging from 4.2K to the maximum temperature, which is at quench initiating point. For this simulation adiabatic approximation is concerned. Heat balance for unit volume of the winding by Maddock and James is [18, 56]-

$$J^2(t)\rho(T)dt = \gamma C(T)dT \tag{5.4}$$

Here all quantities are averaged over the winding cross section, J is current density, ρ is resistivity, γ is density, C is specific heat and t and T indicate as time and temperature respectively. After rearrangement of Eq. (5.4)

$$\int_0^\infty J^2(t)dt = \int_{T_0}^{T_m} \frac{\gamma C(T)}{\rho(T)} dT = U_{T_m} \tag{5.5}$$

There is a single function $U(T_m)$ that is containing material properties of winding material and use to calculate the maximum temperature T_m. There are some of the approximate assumptions are considered for calculation.

1. Current density remains constant at J_0 (initial current density) until energy of the magnet dissipated then after it falls.
2. Temperature rise is given as

$$\int_0^\infty J^2(t)dt = J_0^2 t_d = U_{T_m} \text{ and } U_{T_m} \sim U_0 \left(\frac{T_m}{T_0}\right)^{1/2}. \tag{5.6}$$

3. Resistivity rises linearly with the temperature.

Here t_d indicates characteristic time and $U_T \sim U_0 \left(\frac{T_m}{T_0}\right)^{1/2}$ is found out by winding material property data and curve fit [3].

Normal zone is developed during quench and if cross section of the conductor is A then resistance per unit volume is $\frac{\rho(T)}{A^2}$. Here ρ is average value over the winding cross section.

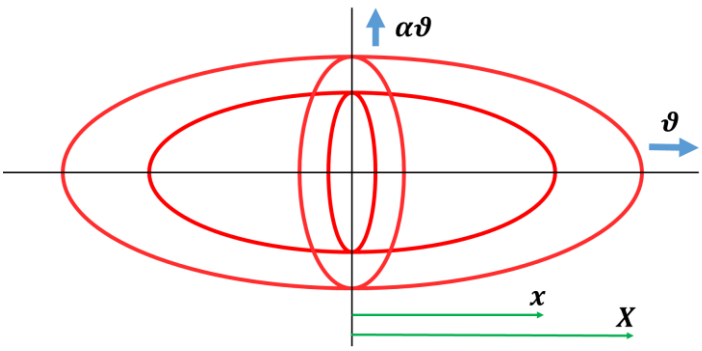

Figure 5.19. 3-D representation of growing normal zone.

So the zone resistance is

$$R = \int_0^X \frac{4\pi x^2 \alpha^2 \rho_T dx}{A^2} \tag{5.7}$$

Here α is dimensionless parameter which indicates ratio of quench propagation velocity in transverse direction ($\upsilon_{transverse}$) to quench propagation velocity in longitudinal direction ($\upsilon_{longitudinal}$).

$$\alpha = \frac{\upsilon_{transverse}}{\upsilon_{longitudinal}} = \left\{\frac{k_t}{k_l}\right\}^{1/2} \tag{5.8}$$

k_t and k_l are the thermal conductivities in transverse and longitudinal direction respectively.

$$\rho_T = \rho_0 \langle \theta/\theta_0 \rangle = \rho_0 \langle U/U_0 \rangle^2 = \rho_0 J_0^2 t^2 / U_0^2 \tag{5.9}$$

The maximum temperature rise is

$$J_0^2 t_d = U_{T_m} \sim U_0 \left(\frac{T_m}{T_0}\right)^{1/2} \tag{5.10}$$

$$T_m = J_0^4 t_d^4 T_0 / U_0^2 \tag{5.11}$$

Resistance growth pattern used to find out current decay, i.e.

$$I = I_o e^{-\left(\frac{R_p t_d}{L}\right)} \tag{5.12}$$

And

$$\tau = \frac{L}{R_p} \tag{5.13}$$

Where I is decaying current, I_o is the initial current, L is the inductance and R_p is the protection resistance. The time constant τ is $\frac{L}{R_p}$.

Then

$$\int J^2(t) dt = \frac{L I_0^2}{2A^2 R_p} = \frac{\tau I_0^2}{2A^2} = U_{T_m} \sim U_0 \left(\frac{T_m}{T_0}\right)^{1/2} \tag{5.14}$$

So if the value of τ is small then temperature rise is also small i.e. keep the inductance of the magnet as low as possible with proper design with the moderate value of dump resistor.
Maximum internal voltage (within coil during quench) is calculated by

$$V = IR = I_o e^{-\left(\frac{R_p t_d}{L}\right)} \left\{ \int_0^X \frac{4\pi x^2 \alpha^2 \rho_T dx}{A^2} \right\} \tag{5.15}$$

If time constant is small then both maximum temperature and maximum voltage can minimized.

OPERA quench simulation resultant graphs for the 6T magnet coil are shown below in Figure 5.20.

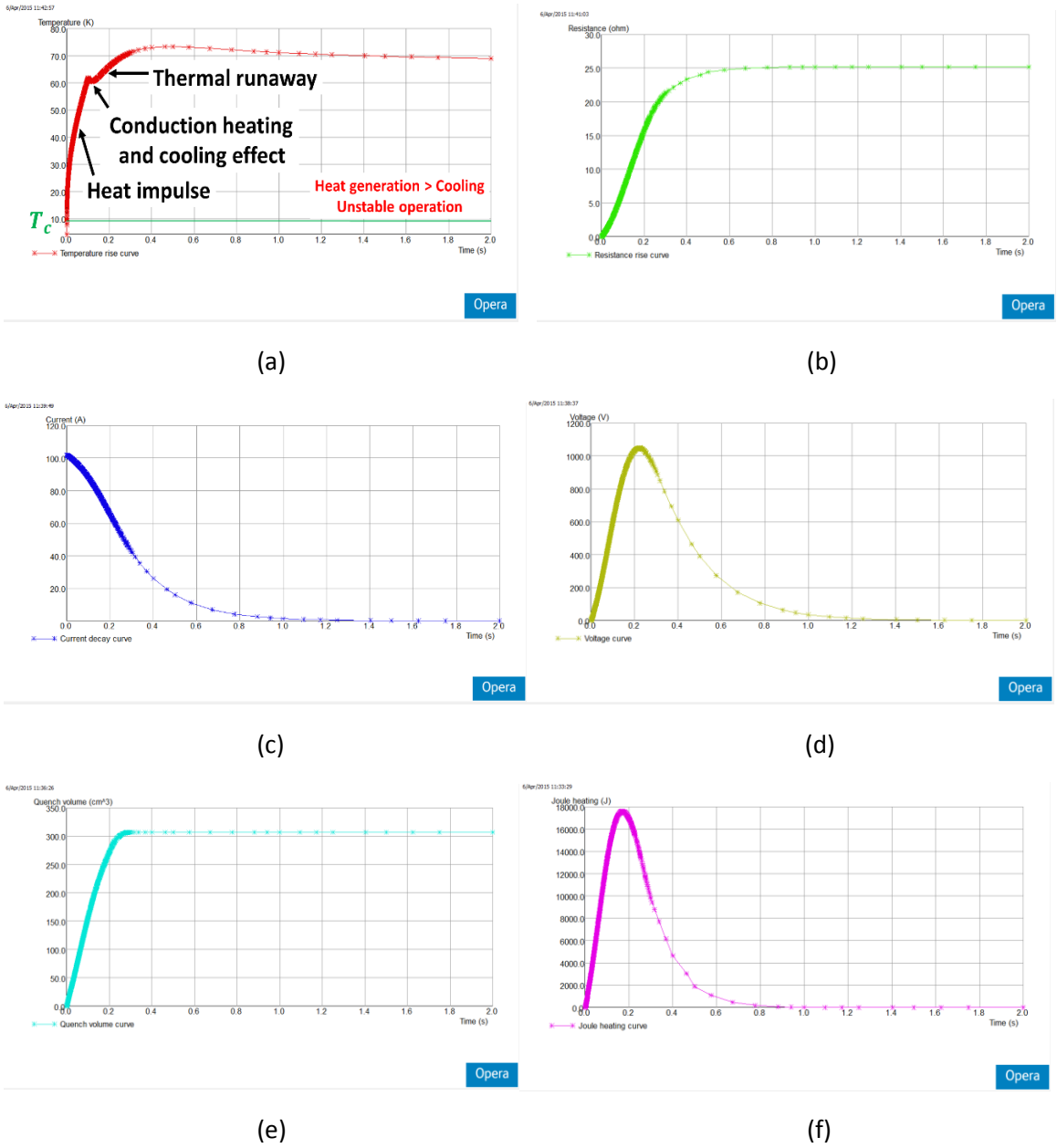

Figure 5.20. (a) Temperature rise curve, (b) Resistance growth curve, (c) Current decay curve, (d) Internal voltage curve, (e) Quench volume curve and (f) Joule heating curve.

Figure 5.20 (a) shows that the hot spot temperature is appoxiamtely 73.36 K, whereas the resistance in the coils grows upto 25Ω, as shown in Figure 5.20 (c). The dump resistor along with the resistance grown in the magnet determines the time constant of the current decay which is shown in the Figure 5.20 (c). It shows that the current decays to zero in 1sec. Figure 5.20 (d) shows the internal voltage inside the coil. The internal voltage of the coil grows upto ~ 1.1 kV. Figure 5.20 (e) and Figure (f) show the corresponding quench volume and the joule

heat generation. Almost ~310 cm^3, full volume of the coil gets quenched around 250 milli seconds. Maximum joule heating 17800 J, happens nearby at 180 milli second.

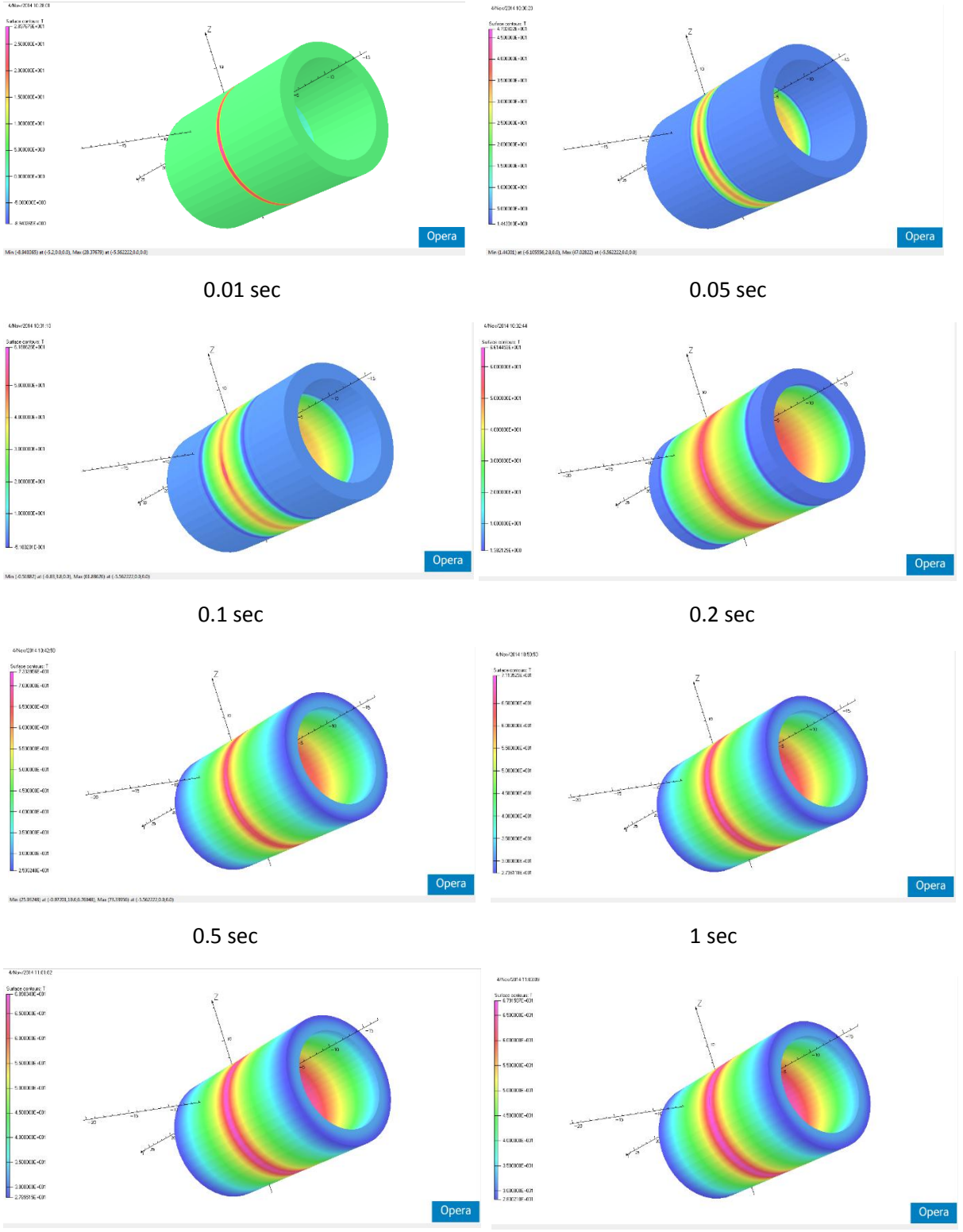

Figure 5.21. 3-Dimentional temperature rise graphics of quenched solenoid magnet coil.

Figure 5.21 shows the transient thermal profile of solenoid magnet. During quench, at 0.01 second the maximum hot spot temperature is 29K, whereas it reaches up to 62K at 0.1 second. The maximum coil temperature occurs after 0.5 seconds i.e. 74K. After it starts decreasing and at 1 second time period maximum temperature becomes 71K. The maximum temperature of coil after 3 seconds is 68K.

5.6.7 Quench Simulation

Quench analysis of 6T NbTi solenoid magnet has been simulated using different operating conditions in OPERA. This simulation will help us to understand the quench phenomenon at different operating condition. These conditions are-

1. *Variation of heat pulse-*

A certain amount of heat pulse needs to be given to the NbTi coil to simulate different types of thermal perturbation which eventually initiate quench.

2. *Dump resistor of different values-*

The values of dump resistance will be varied to understand the significance of the dump resistor in determining the hot spot temperature in the coil and current decay for safe operation of the magnet.

3. *Changing the location of quench initiation-*

During operation of any NbTi magnet, the quench can be initiated at any parts of the winding. During quench simulation, we have given the heat pulse to initiate quench at different locations of the coil.

4. *Different Quench protection configuration-*

There can be different configurations of the protection system. We have simulated the Quench with different configuration of the protection system.

1. *Variation in heat pulse*

Case-1: 4W heat input for the time duration of 0.1 second with CKT1 protection circuit as shown in Figure 5.15.

The detailed analysis of Case-1 is briefly described in section 5.6. Figure 5.20 and Figure 5.21 show the graphical representation of the simulation for case-1. Figure 5.22 summarizes the analysis of case-1.

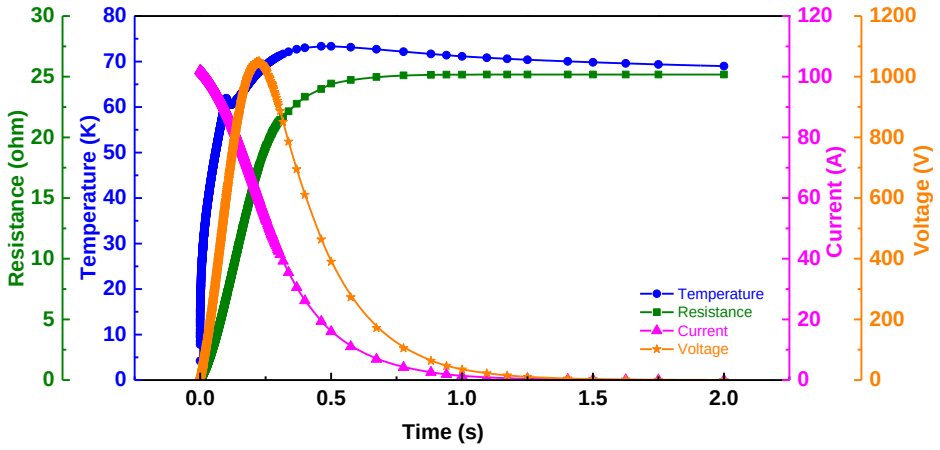

Figure 5.22. Resistance, temperature, current and internal voltage of the magnet coil v/s time curve for case-1.

Case-2: 3W heat input for the time duration of 0.1 second with CKT1 protection circuit.

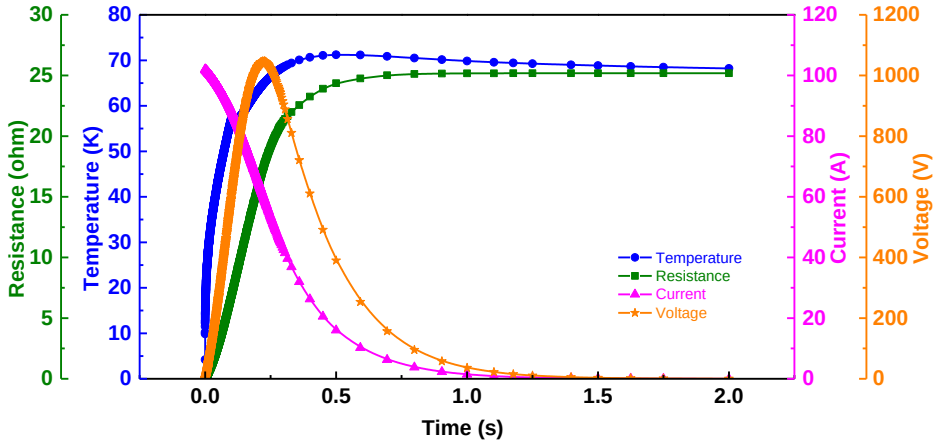

Figure 5.23. Resistance, temperature, current and internal voltage of the magnet coil v/s time curve for case-2.

In Figure 5.22 and Figure 5.23, applied heats are different, which are 4W and 3W respectively. It is clear from the simulation shown in Figure 5.22 and Figure 5.23 that there are not any significant change in peak temperature or hot spot temperature. With 4W of heat pulse, the temperature of hot spot reaches to 73.36 K, as shown in Figure 5.22. Whereas in Figure 5.23, the hot spot temperature is 71.22 K with 3W heat pulse. The current decay profiles in both case are almost similar. The corresponding resistance growths for case-1 and case-2 are 23.9Ω and 24.4Ω with the maximum internal voltages of 1050V and 1046V respectively.

Case-3: 4W heat input for the time duration of 0.05 second with CKT1 protection circuit.

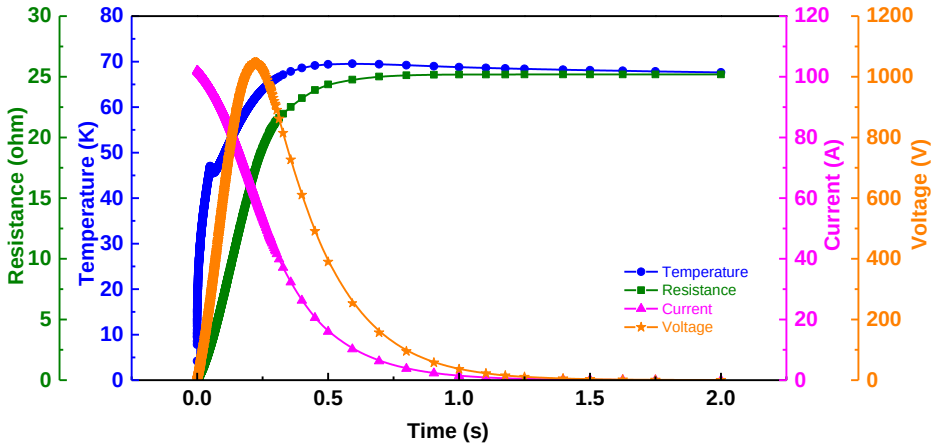

Figure 5.24. Resistance, temperature, current and internal voltage of the magnet coil v/s time curve for case-3.

Case-4: 40W heat input for the time duration of 0.01 second with CKT1 protection circuit.

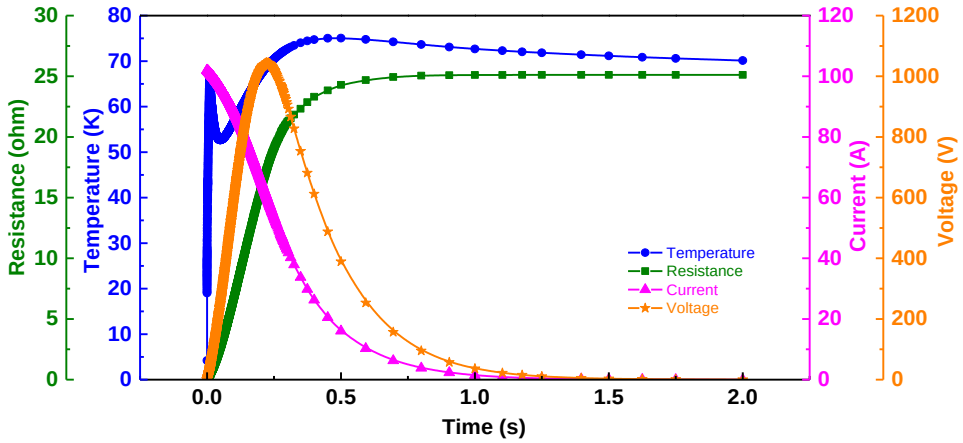

Figure 5.25. Resistance, temperature, current and internal voltage of the magnet coil v/s time curve for case-4.

Figure 5.24 and 5.25 show the simulated result for the quench in which variation of the time duration of the heat application is carried out with applied energy variation i.e. 0.2J and 0.4J respectively. In Figure 5.24, time duration of heat input is 0.05 sec so heat is equal to 4W and in Figure 5.25, heating time is 0.01 sec with 40W heat. Figure 5.24 shows that due to the less amount of input energy, the maximum temperature rise is also less which is 69.54K but at the same case internal voltage is 1047.1V which is high. In Figure 5.25, due to higher heat input for smaller time, temperature rises sharply and the maximum temperature goes up to 75.04K. Though, the current decay patterns are almost similar as the current decay is determined by the effective resistance growth which in fact almost same for both cases. Hence it can be concluded

that the amount of input heat energy does not play very significant role in determining the hot spot temperature. Once the quench has been initiated may be by small amount of heat dissipation, the normal zone of the magnet will grow and decay the current.

Table 5.5. Quench analysis data for case-1 to case- 4.

CASE No	Heat source description in OPERA	Heat (W)	Energy (J)	Heat Flux (W/cm^2)	Time duration of heating (sec)	Dump resistance (Ω)	Time at which max. Temp. occur (s)	Max. Temp. at coil (K)	Resistance at max. Temp. time at coil (Ω)	Current at max. Temp. time (A)	Max. internal Voltage (V)	Circuit type
1	-RANGE(Time;0;0.1)*RANGE(Y;0;0.2)*RANGE(X;-5.2;-5.4)*100	4	0.4	100	0.1	5	0.4624	73.359	23.991	19.316	1050.4	1
2	-RANGE(Time;0;0.1)*RANGE(Y;0;0.2)*RANGE(X;-5.2;-5.4)*75	3	0.3	75	0.1	5	0.5	71.218	24.367	15.998	1046.4	1
3	-RANGE(Time;0;0.05)*RANGE(Y;0;0.2)*RANGE(X;-5.2;-5.4)*100	4	0.2	100	0.05	5	0.592810	69.549	24.767	10.237	1047.1	1
4	-RANGE(Time;0;0.01)*RANGE(Y;0;0.2)*RANGE(X;-5.2;-5.4)*1000	40	0.4	1000	0.01	5	0.5	75.046	24.297	16.022	1044.2	1

2. *Dump resistor of different values*

Case-5: 4W heat input for the time duration of 0.1 second with CKT1 protection circuit having dump resistance of 0.001Ω.

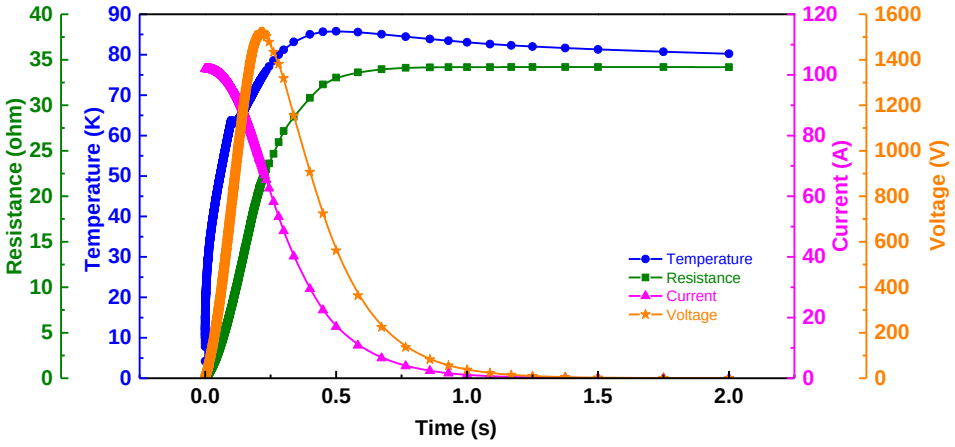

Figure 5.26. Resistance, temperature, current and internal voltage of the magnet coil v/s time curve for case-5.

Case-6: 4W heat input for the time duration of 0.1 second with CKT1 protection circuit having dump resistance of 1MΩ.

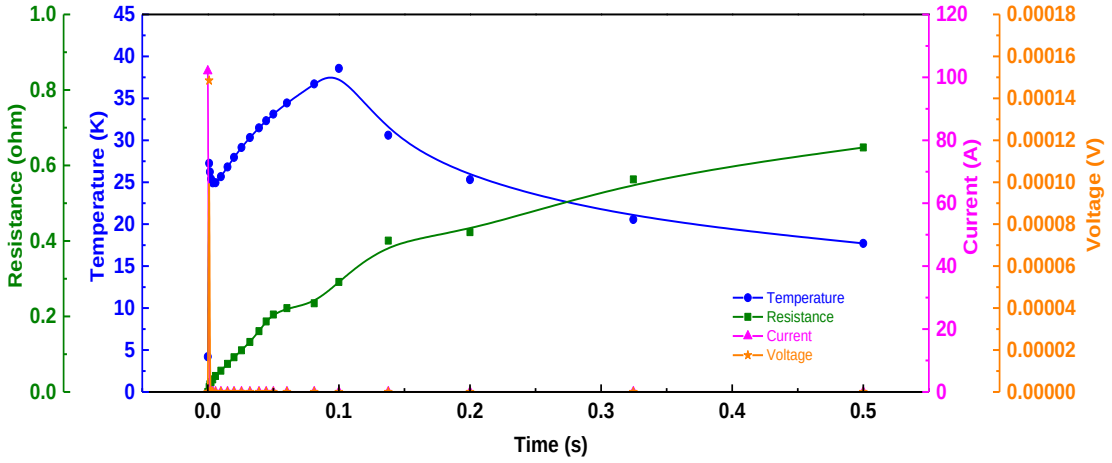

.

Figure 5.27. Resistance, temperature, current and internal voltage of the magnet coil v/s time curve for case-6.

As earlier discussed that the time constant is $\tau = \frac{L}{R_p}$ where L is the coil inductance and R_p is dump resistance, which are 5.5H and 5Ω respectively for the 6T cryogen free superconducting magnet, so the time constant is 1.1 second. The value of dump resistance effects the external voltage across the dump resistor and time constant. If dump resistance is small then time constant is large and external voltage is small and vice versa. The external voltage is $V_{ext} = I_0.R_p$, across the dump resistor for the initial current 102A, is calculated to be 510V.

Figure 5.26 and 5.27 represent the quench simulation with 0.001Ω dump resistor (case-5) and 1MΩ dump resistor (case-6). Figure 5.26 indicates that if dump resistance is small (0.001Ω) as in case-5, the decay time does not change significantly as the resistance growth in the coil is almost same i.e. 33Ω. The resistance grown in the coil play the major role in determining the decay time. Though in case-5, the hot spot temperature is found to be little higher (85.75K) than that of the earlier cases. When the value of dump resistor is too high (1MΩ), which is almost like open circuit the decay time will be determined by the high value of the dump resistor. The time constant in this case will be very short because of the higher resistance value of dump resistor. Hence the current will decay very fast as shown in the Figure 5.27. But in this case, the external voltage would be very large which is around 1.02E08V with time constant equal to 5.5E-06. Internal voltage within coil is 0.000148V which is very small value. The high external voltage will eventually induce arcing in the magnet which may destroy the coil. The external voltage developed across dump resistor necessarily kept at the moderate level so as time constant, so always prefer for the moderate value of dump resistor.

Table 5.6. Quench analysis data for case-5 to case- 6.

CASE No	Heat source description in OPERA	Heat (W)	Energy (J)	Heat Flux (W/cm²)	Time duration of heating (sec)	Dump resistance (Ω)	Time at which max. Temp. occur (s)	Max. Temp. at coil (K)	Resistance at max. Temp. time at coil (Ω)	Current at max. Temp. time (A)	Max. internal Voltage (V)	Circuit type
5	-RANGE(Time;0;0.1)*RANGE (Y;0;0.2)*RANGE (X;-5.2;-5.4)*100	4	0.4	100	0.1	0.001	0.5	85.7990	33.04591	16.974	1522.1	1
6	-RANGE(Time;0;0.1)*RANGE (Y;0;0.2)*RANGE (X;-5.2;-5.4)*100	4	0.4	100	0.1	1.00E+06	0.1	38.5733	0.291316	7.4E-81	0.000148	1

3. *Changing the location of quench initiation*

Case-7: 4W heat input for the time duration of 0.1 second with CKT1 protection circuit. The heat input is given at different surface of the coil; Y-coordinate (9.8 to10.0) and X-coordinate (-5.2 to -5.4).

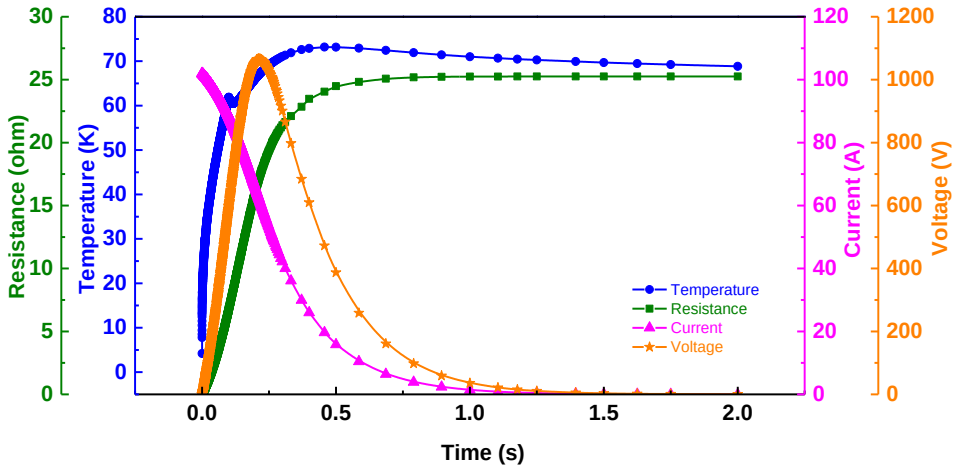

Figure 5.28. Resistance, temperature, current and internal voltage of the magnet coil v/s time curve for case-7.

Figure 5.28 shows the graphs for the quench simulation of case-7. The result shown in Figure 5.28 is almost similar to the result shown in Figure 5.22 for case-1. The only difference in both the cases (case-1 and case-7) is the surface, where the heat pulse is given to initiate quench. Hence, it is concluded that the location of the heat input is immaterial for post-quench behavior of the magnet. This signifies that the location of quench initiation is not important for the post quench behavior.

Table 5.7. Quench analysis data for case-7.

CASE No	Heat source description in OPERA	Heat (W)	Energy (J)	Heat Flux (W/cm²)	Time duration of heating (sec)	Dump resistance (Ω)	Time at which max. Temp. occur (s)	Max. Temp. at coil (K)	Resistance at max. Temp. time at coil (Ω)	Current at max. Temp. time (A)	Max. Voltage (V)	Circuit type
7	- RANGE(Time;0;0.1)*RANGE (Y;9.8;10.0) *RANGE(X;-5.2;-5.4)*100	4	0.4	100	0.1	5	0.457080	73.18176	24.05015	19.653	1065.9	1

4. *Different Quench protection configuration*

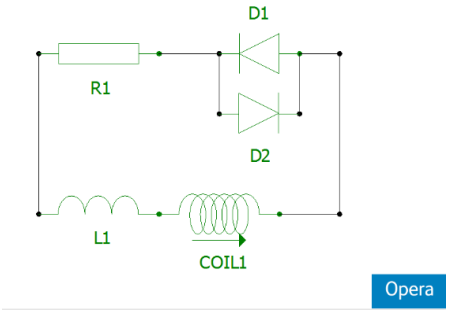

Figure 5.29. Quench protection circuit -CKT2.

Figure 5.29 shows new configuration of quench protection circuit (CKT2), where back to back diodes of forward voltage of 1V are attached in series with the dump resistor (5Ω).

Case-8: 4W heat input for the time duration of 0.1 second with CKT2 protection circuit.

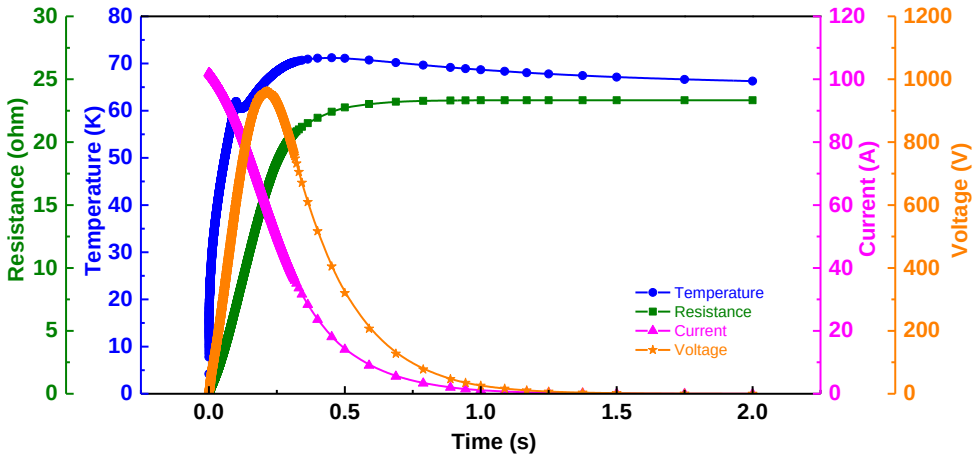

Figure 5.30. Resistance, temperature, current and internal voltage of the magnet coil v/s time curve for case-8.

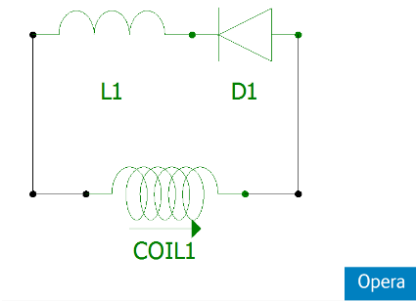

Figure 5.31. Quench protection circuit -CKT3.

Figure 5.31 shows a quench protection circuit in which a single diode of forward voltage of 1V is attached parallel with the magnet coil.

Case-9: 4W heat input for the time duration of 0.1 second with CKT3 protection circuit.

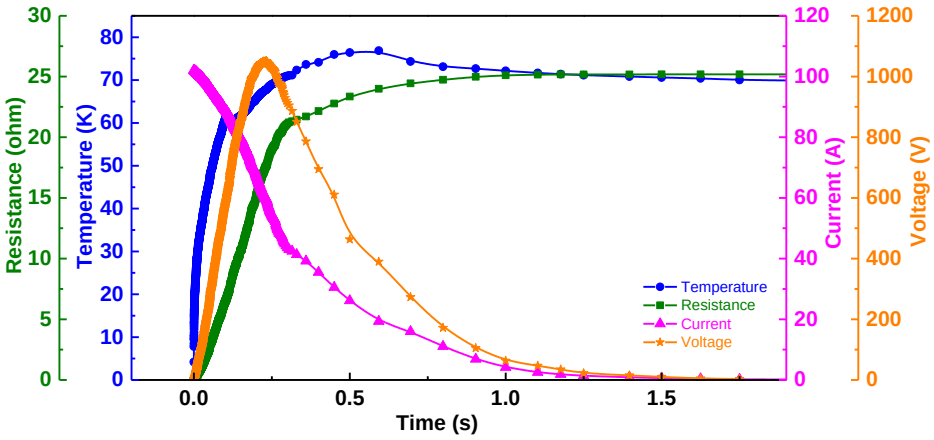

Figure 5.32. Resistance, temperature, current and internal voltage of the magnet coil v/s time curve for case-9.

Table 5.8. Quench analysis data for case-8 to case- 9.

CASE No	Heat source description in OPERA	Heat (W)	Energy (J)	Heat Flux (W/cm^2)	Time duration of heating (sec)	Dump resistance (Ω)	Time at which max. Temp. occur (s)	Max. Temp. at coil (K)	Resistance at max. Temp. time at coil (Ω)	Current at max. Temp. time (A)	Max. internal Voltage (V)	Circuit type
8	-RANGE(Time;0;0.1)*RANGE(Y;0;0.2)*RANGE(X;-5.2;-5.4)*100	4	0.4	100	0.1	5 (With back to back diode)	0.451955	71.21602	22.41664	18.063	960.54	2
9	-RANGE(Time;0;0.1)*RANGE(Y;0;0.2)*RANGE(X;-5.2;-5.4)*100	4	0.4	100	0.1	not applied (only with diode)	0.592828	76.8595	23.99193	19.316	1050.4	3

Figure 5.30 shows the result of the quench simulation of magnet, when protected with CKT2 protection circuit. Simulated results show that when back to back diodes are fixed in series with dump resistor then the internal voltage generated within coil is reduced i.e. 960.54V but

in the same case, the maximum temperature rise is similar to the case-1, where in both cases, same energy is applied for same time duration. So back to back diode arrangement help to low down the voltage for some extent.

Figure 5.32 indicates simulated results for quench with CKT3 quench protection circuit. Here the diode is attached with the magnet in parallel but without any dump resistor in the circuit. Result shows that the maximum temperature rise is the only parameter which is little higher i.e. 76.85K otherwise it is almost similar to case-1.

5.7 Experimental quench study of 6T NbTi solenoid magnet

The schematic of the quench protection system used for the 6T CFMS developed at IUAC is shown in Figure 5.33 (a). Figure 5.33 (b) shows the internal view of the CFMS. It shows the dump resistor of 5Ω is mounted across the NbTi magnet. The dump resistor is mounted at the magnet cooling plate. The reason, for mounting the dump resistor in the cold section of the CFMS, is to protect the magnet or to provide parallel by pass path in case of HTS lead fails.

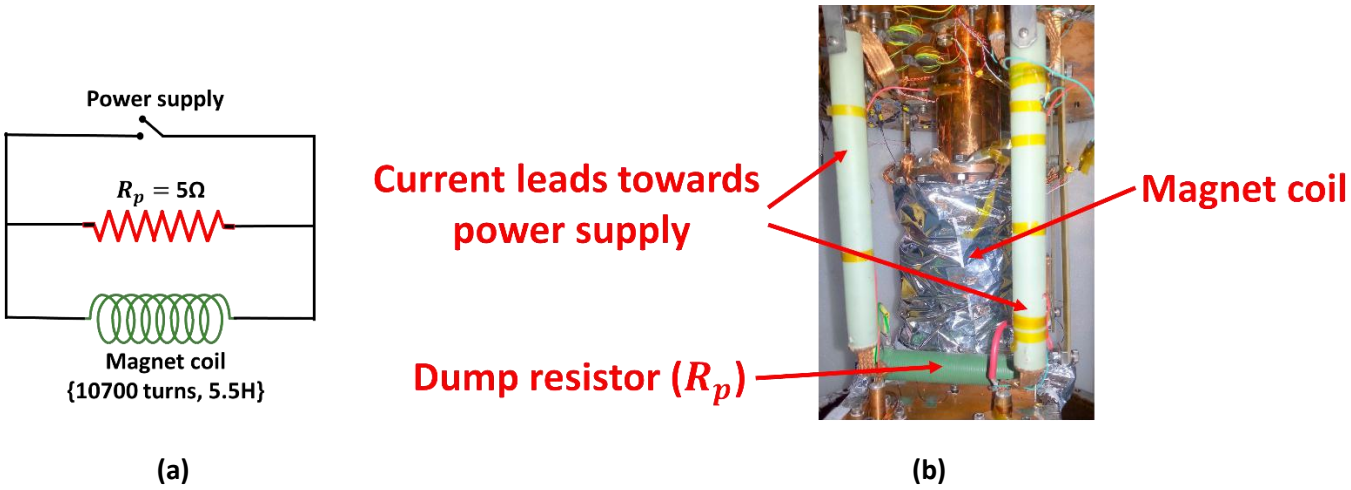

Figure 5.33. Quench protection circuit for 6T cryogen free superconducting magnet system.

In this protection circuit a dump resistor of 5Ω resistance is fixed parallel with the magnet coil. Since solenoid coil has 5.5H inductance, so the time constant $\tau = \left\{\frac{L}{R_p}\right\}$ for the 6T NbTi solenoid magnet is 1.1 sec, so if quench will happen then current decay time for the magnet coil is ≈ 1 sec.

5.7.1 Experimental results of quench for 6T NbTi solenoid magnet

The thermal profile of the magnet system after the quench at 101.1A is shown in the Figure 5.34. This figure shows adiabatic rise in temperature of the various components of the magnet system after the quench. The temperature at the magnet reaches to 53.25 K whereas the 4 K lead joint, magnet cooling plate and the CCR-plate reach respectively to 33.5 K, 15.5 K and 15.87 K. The temperature at the magnet-cooling plate and the bobbin interestingly remains more or less stable for nearly 18 minutes before starting to drop and finally reaching 3 K. The adiabatic temperature rise signifies the dumping of the magnetic stored energy at different components of the magnet system. Figure 5.34 also shows the thermal behaviour of the radiation shield and the 1st stage of the CCR after the quench. Initially, there is a sudden drop of temperature of the thermal shield and the 1st stage of the CCR by about 0.5 K from their respective temperatures of 39.6 K and 37.3 K. Thereafter the two temperatures start rising slowly till the 2nd stage temperature drops from 15.89 K to the 3 K. This increase in the temperature of the thermal shield is due to the sudden reduction in the refrigeration capacity of the 1st stage of the CCR after adiabatic transition in the load map.

The rise of the temperature of the radiation shield is of the order of 5 K in 40 minutes. The post-quench thermal profile, shown in the Figure 5.34, signifies that the magnet is safe in case of a quench. The passive quench protection system shown in Figure 5.15 is able to take care of the quenching of the 6 T magnet.

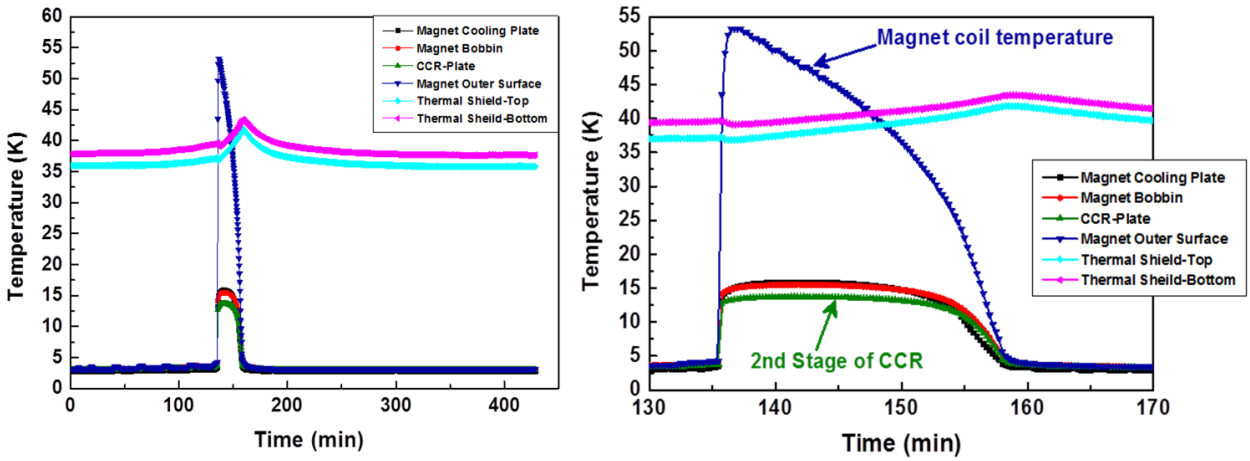

(a) (b)

Figure 5.34. (a) Temperature characteristic of different parts of the magnet system with respect to time, during quench of magnet at 6T magnetic field and (b) Enlarge time section view of the Figure 5.34 (a).

6.

VARIABLE TEMPERATURE INSERT FOR 6T CFMS

6.1 Introduction

6.2 Variable temperature insert (VTI) using gas gap heat switch

6.1 Introduction

High magnetic field is possible now a days due to development of superconducting magnets. Superconducting magnets can be developed by using low temperature superconductor (LTS) or high temperature superconductor (HTS) materials. NbTi and Nb3Sn are the commonly used LTS materials for superconducting magnet manufacturing. Variable magnetic field can be achieved by using these superconducting magnets but the researcher of low temperature physics also require variable temperature at the sample. The sample temperature can be varied by using cryocooler based variable temperature inserts (VTI) to be integrated with the CFMS. In typical NbTi magnet system, the magnet is operated at 4K by using either liquid helium or cryocoolers. Conduction cooled superconducting magnet system are basically based on the use of two stage cryocooler with its available refrigeration capacity at 2nd stage. The properties of material can simultaneously be studied in the effect of low temperature and higher magnetic field in CFMS integrated with VTI. In this chapter two types of variable temperature inserts are discussed which are able to integrate and operate with 6T cryogen free superconducting magnet system (IUAC).

6.1.1 Types of the variable temperature inserts (VTI)

1. VTI using gas gap heat switch (GGHS).

2. VTI using GM cryocooler based helium gas circulation.

1. *VTI using GGHS-*

Heat switch or thermal switch is a device which allows adjusted tuning between good thermal conductance as well as thermal resistance, so using this tuning this device can able to generate the required thermal environment. Thermal conductance ability allows thermal connectivity between two systems and when thermal connections are not required then good thermal resistance allows to cut off the thermal link. One of the type of heat switch is GGHS in which thermal connectivity of the two system depends on the presence or absence of the inert gas conduction medium. These presence and absence of the conduction medium is controlled by the pressurized inert gas inside the very small annular gap between two concentric high thermal conductive metal blocks. These metal blocks are physically connected with each other with a very thin metal tube, which has very poor thermal conductivity. One side of the GGHS attached with the cold finger of the GM cryocooler and another side with the sample space. The absence of gas conduction medium makes it possible to vary the temperature at the sample space. A cryopumping system is attached with the cold section of the GGHS which regulate the operation of the inert gas insertion and rejection, inside the annular space via its activation and deactivation [57-60].

2. *VTI using GM cryocooler based helium gas circulation-*

Helium gas circulation through the heat exchangers connected to two stages of GM cryocooler allows cool down of the circulatory helium gas. The two stage GM cryocooler (4.2K @ 0.8W) generates 4K temperature at 2nd stage, so using this refrigeration capacity circulated helium gas can reach 4K temperature and further this cooled helium gas cools the sample space. The thermal environment of the sample space can be changed with the use of a heating source which help to cover the variable temperature range.

6.2 VTI using gas gap heat switch (GGHS)

In cryogenic engineering applications heat switches are used to minimize thermal loads on cooling systems by decoupling the different components. Heat switch becomes necessary component, when cooling is not required for the attached component or that component causes over-heating, which can reduce the cooling capacity. The thermal toggling between the ON and OFF thermal states is the main work of the heat switch. This thermal toggling or tuning is dependent over the thermal conductance by the heat switch in between two distinguish system. When thermal conductance is there then switch is said to be ON state otherwise OFF state. Heat switches can actively control the temperature of the attached components, so power requirement to operate the heat switches is very less. The GGHS can be used to generate the variable temperature environment when it attached with the CFMS. This section describe the use of GGHS as VTI integrated with CFMS. Magneto-thermal profile of the CFMS when variable temperature generation is taken place, is also mentioned in this section.

6.2.1 Gas gap heat switch (GGHS)

The gas gap heat switch is a component which is used in several low temperature applications basically related to cryogenics. In the gas gap heat switch the thermal coupling of the two systems is regulated with turned ON and turned OFF state. The thermal ON state resembles for the presence of inert gas inside the concentric annular space and OFF state is vice versa of it. A cryogenic gas gap heat switch has an application, for instance that when a two stage GM cryocooler is used for the cooling purpose of 6T NbTi magnet, operating at particular refrigeration capacity, heat switch allows thermal disconnection/connection between sample space and GM cryocooler, so variable temperature operation can perform at sample space. The gas gap heat switch has an ability to make or break the thermal contact between two systems that allows further heat load reduction on the cold finger of the GM cryocooler. The gas gap heat switch has an advantage that having no moving parts, if controlled by a cryopump. A small cryopump works on the principle of gas adsorption by the adsorption media i.e. activated charcoal. Cryopump operates at silence with its activation for inert gas releasing by the application of certain amount of heat on it and deactivation is achieved with cooling through GM cryocooler. Due to inert gas adsorption properties when the temperature of the cryopump goes down below 25K, due to charcoal activation, all the available inert gas adsorbed and then other side of the gas gap heat switch thermally disconnected through the cryocooler. So the temperature of the other side of the gas gap heat switch stabilized at particular limit which resembles the temperature limit of ON state and OFF state. Above this temperature limit gas gap heat switch at it's OFF state. For further reduction of the temperature of the other side of the gas gap heat switch, it needs to be turned ON condition by raising the temperature of the cryopump and set it to about 25K then releasing of the adsorbed inert gas occurs at annular space which allows gas conduction, through which temperature reduced and reached up to the 2^{nd} stage of GM cryocooler temperature range. Figure 6.1 represents the general schematic diagram of the gas gap heat switch [57-60].

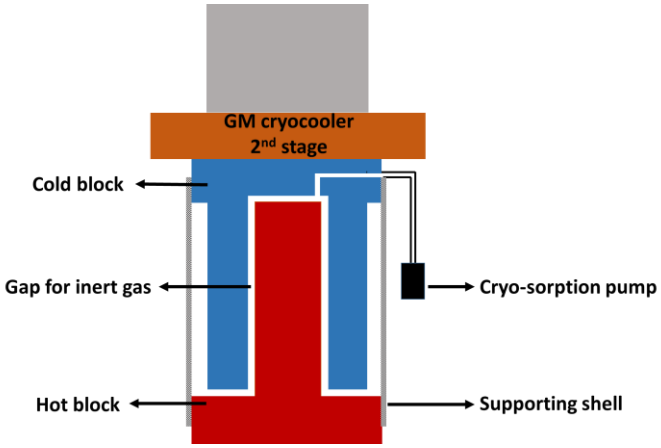

Figure 6.1. Schematic diagram of the gas gap heat switch.

A simplest and most common form of the GGHS is developed in Universidade Nova de Lisboa, Portugal [61]. This GGHS have been developed to study the feasibility of using as VTI for the 6T cryogen free superconducting magnet system (IUAC, New Delhi). In the conventional VTI system, which are integrated with cryocooler based superconducting magnet system, are totally dependent over the helium gas circulation. The cooling of the helium gas is achieved by the cold finger of the GM cryocooler, then Joule-Thompson expansion valve which allows to liquefy the circulatory helium gas and then by the application of heat variable temperature range can be achieved in the sample space. By using GGHS in the any conduction-cooled superconducting magnet system, whole system becomes completely cryogen free because there is no use of helium, which is directly contact with the sample space. The primary purpose of the cryocooler is to cool the superconducting magnet and maintain its temperature well below to the current sharing temperature limit, so that superconducting magnet will not lose its superconducting state and will not quench. Superconducting magnet system operates at certain amount of load which is maintained by the two stage 1.5W @ 4.2K GM cryocooler. The estimated load of this 6T superconducting magnet system is around 1W with considering all the safety factors. So the remaining free 500mW power could be used for GGHS based VTI. Figure 6.2 shows the solid works design of gas gap heat switch. Figure 6.3 shows the built up copper blocks with thin SS tube.

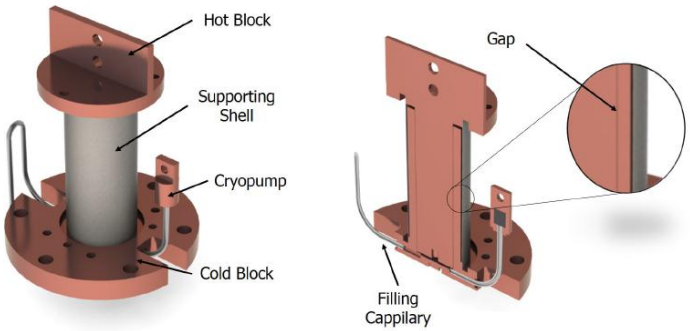

Figure 6.2. Gas gap heat switch design (Solid Works) [61].

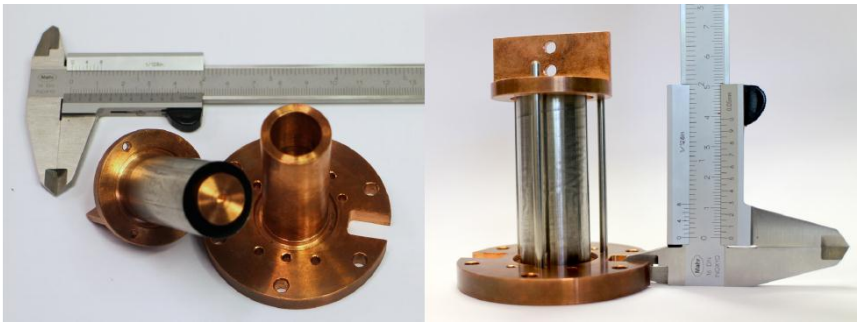

Figure 6.3. Two copper blocks with thin SS tube [61].

The helium GGHS is developed to fulfill the VTI purpose with integrated operation with 6T conduction cooled superconducting magnet system. The GGHS uses helium inert gas to provide conductive medium between two systems. The GGHS has two concentric cylindrical copper blocks, which are separated by a small gap (80 μm), and held together by a thin-walled (100 μm) stainless steel tube. This stainless steel tube which has very poor thermal conductivity provides the thermal isolation in the OFF state. A sorption pump controls the presence (ON state) or absence of gas (OFF state) inside the heat switch. The activated charcoal of the cryopump has ability to adsorb great quantity of inert gas having inner solid surface area of 3000 m^2/g. In the OFF state of the heat switch thermal conduction through the gas is negligible and all the thermal conduction occurs through the stainless steel shell. In OFF state molecular flow is there in the annular space which occurs, when mean free path is higher than the length of the gap. OFF state of the heat switch is obtained when gas thermal conductance is 10 time smaller than the stainless steel shell. On the other side, ON state is obtained when there is sufficient pressure inside the annular space that ensure viscous flow of gases. ON state is achieved when mean free path of gas is at least 100 times smaller than the dimension of the gap. To maintain the gap between two copper blocks and attachment with the stainless steel tube, always avoid any of the mechanical constraints on the heat switch ends, for this purpose one common solution is, use highly flexible copper braids at the ends of the heat switch for attachment purpose [15, 61-66].

6.2.2 Solid and gas conduction

The heat transfer in the solids occur due to conductive electrons and lattice vibrations (phonons). In pure metals heat transfer is dominated by the electron on the other side in impure metals, alloys and semiconductors, majority of thermal conduction occur due to phonons. The solid conduction in the body is,

$$Q = \frac{A.\int_{T_c}^{T_h} k.dT}{L} \tag{6.1}$$

Where A is the cross sectional area, T_h and T_c are the hot end and cold end temperatures respectively, k is the thermal conductivity of material and L is the length of the body.

The conductive heat transfer in gases is dependent over the viscous and molecular flow regimes of the gases. If there is viscous flow, in which mean free path (λ) is very less than length between two walls (L), then according to kinetic theory of gases thermal conductivity of the gas is,

$$k = \frac{1}{3N_A\sigma}\sqrt{\frac{3RT}{M}}C_{mol} \tag{6.2}$$

Where N_A is avagrado number, M is the molar mass of the gas, R is the gas constant, T is temperature in kelvin, σ is collisional cross section area and C_{mol} is the molar heat capacity.

Molecular flow of the gases is achieved when the mean free path (λ) is larger than the distance between the walls (L). Heat flow rate in the molecular regime is,

$$Q' = \alpha S\left(\frac{\gamma+1}{\gamma-1}\right)\sqrt{\frac{R}{8\pi MT}}P\Delta T \tag{6.3}$$

Where α is the accommodation constant, γ is the heat capacity ratio $\left[\gamma = \frac{c_p}{c_v}\right]$ and P is the gas pressure.

The combined or intermediate flow is described by the mentioned effective heat conductance equation.

$$\frac{1}{C_{eff}} = \frac{1}{C_m} + \frac{1}{C_v} \tag{6.4}$$

Where C_{eff} is the effective conductance in intermediate flow regime, C_m is conductance in molecular flow regime and C_v is the conductance in viscous flow regime. Figure 6.4 represents dependency of pressure in viscous and molecular flow [61].

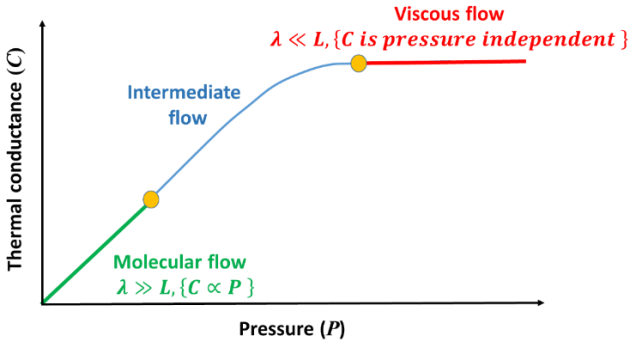

Figure 6.4. Thermal conductance v/s pressure in different gas flow regimes.

6.2.3 Heat flow mechanism for the GGHS

The GGHS is directly coupled with the 2nd stage of the GM cryocooler with its cold block. The only physical contact in between hot and cold block is thin (100 µm) stainless steel tube. These concentric copper blocks are separated to each other with a small gap of 80 µm. During the OFF state of the heat switch there is no helium gas, so only heat from the cold block is extracted by the 2nd stage. When heat switch is ON, then 2nd stage carry the thermal load of cold block as well as hot block and other attached components (sample space) with hot block. ON state of the heat switch is achieved by the release of the adsorbed helium gas from the cryopump through a small stainless steel capillary. The OFF condition of the heat switch is obtained at helium gas pressure (maximum) 5.3E-06 mbar at 4K and ON state is gained when helium gas pressure is 1.3 mbar (minimum) at 4K. The charge pressure of the helium gas is 98 mbar at

room temperature. The cryopump is filled with 45mg of type-C activated charcoal. The adsorbing medium volume or mass is decided with help of the charged pressure and maximum OFF state pressure then this mass of activated charcoal can provide ON and OFF state by adsorbing action. At 4K the ON thermal conductance is 285 mW/K which is achieved with helium-4 and OFF state thermal conductance is 0.09 mW/K, so ON to OFF ratio of this gas gap heat switch is 3167. Figure 6.5 shows the heat flow arrangement of GGHS [61].

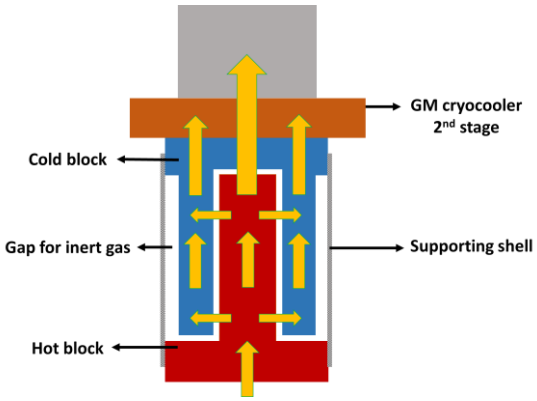

Figure 6.5. Heat flow mechanism of gas gap heat switch.

6.2.4 Testing of GGHS in Cryogen Free Superconducting Magnet System

The GGHS has been integrated with the 6T conduction cooled superconducting magnet system. Both systems are dependent on a single, two-stage GM cryocooler. The primary aim of the system is to maintain the magnet temperature nearly 4K and then using GGHS vary the sample space temperature as wide range as possible (4K-300K). For VTI, a sample probe assembly has been designed and assembled with the 6T superconducting magnet system. Sample space/sample probe is located nearby to the superconducting magnet because of magnet system has been developed prior to the GGHS development.

The cold block of the GGHS is directly attached with the 2nd stage of GM cryocooler. For the operation of heat switch a 1Ω resistor is attached with the cryopump with a calibrated silicon diode sensor. This resistor permits to raise the temperature of cryopump up to 25K with the help of Lakeshore temperature controller to make it ON state of heat switch from OFF state. Figure 6.6 shows the integration of the gas gap heat switch with the CFMS. To measure the temperature of hot block of the GGHS, a calibrated silicon diode sensor is fixed with it. Hot block and sample base is thermally connected through the four copper braids. The length of each copper braid is about 35 cm and cross sectional area is 20 mm^2. A sample base is the part of sample probe assembly which allows space for sample probe. Sample base is made of OFHC copper and a calibrated silicon diode is fixed with it. Sample base is mechanically supported with the 1st stage lid with the help of G10 strips. An OFHC copper sample probe is brazed with a stainless steel tube and a 20Ω resistor is attached with the sample probe along with a calibrated silicon diode temperature sensor. For the temperature variation of the sample probe, Lakeshore temperature controller is fixed with it. These sample probe and sample base are connected to each other by the mean of mechanical push contact only and to avoid surface irregularities Apiezon N-grease is provided in between them. To ensure good thermal contact a spring bolted mechanism is attached with the sample tube.

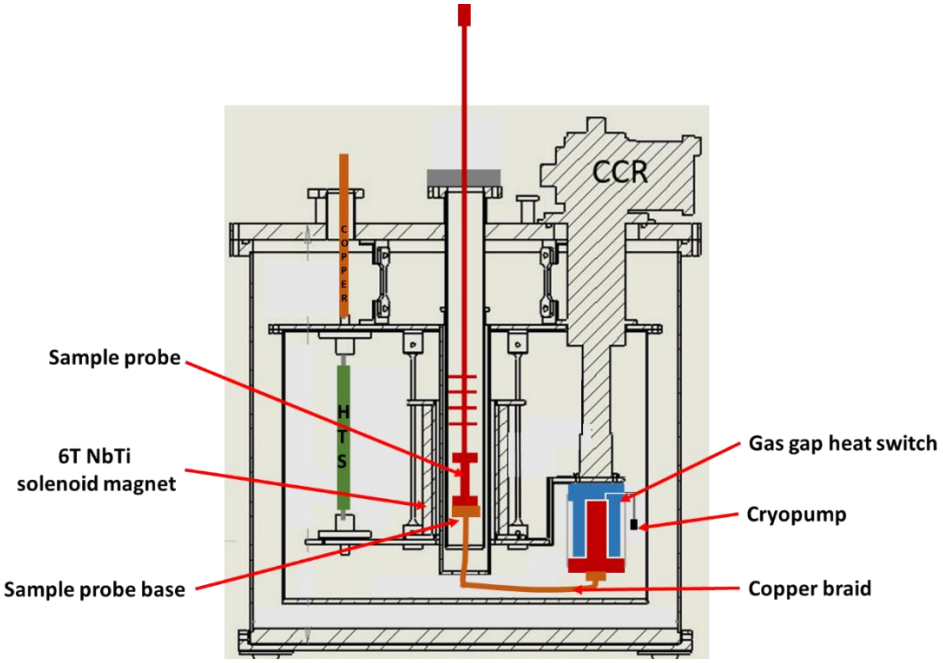

Figure 6.6. Schematic representation of integrated gas gap heat switch with CFMS.

There are cernox temperature sensors are already fixed with the magnet surface, magnet cooling plates, 2nd stage of the GM cryocooler and thermal radiation shield of the magnet system. Here 2nd stage of the GM cryocooler temperature also represent the temperature of the cold block because cold block is directly attached to it. To allow the better thermal conditioning, all the sensor wires are perfectly thermal anchored with the neck section of the GM cryocooler. For the monitoring of temperature sensors, Lakeshore temperature monitors are connected with them. A Bayard Alpert full range vacuum gauge is attached with the system for vacuum measurement. Figure 6.7 shows the test arrangements for GGHS based VTI operation.

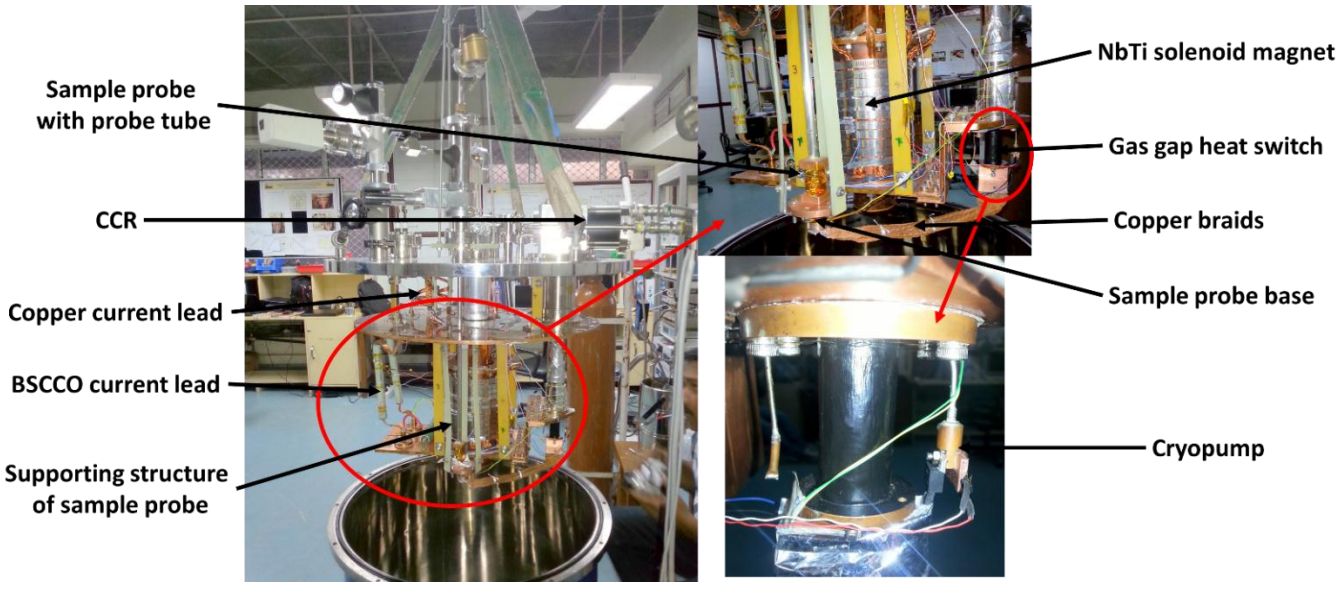

Figure 6.7. Test setup for the GGHS based VTI operation in CFMS.

6.2.4.1 Thermal profile of GGHS integrated with CFMS

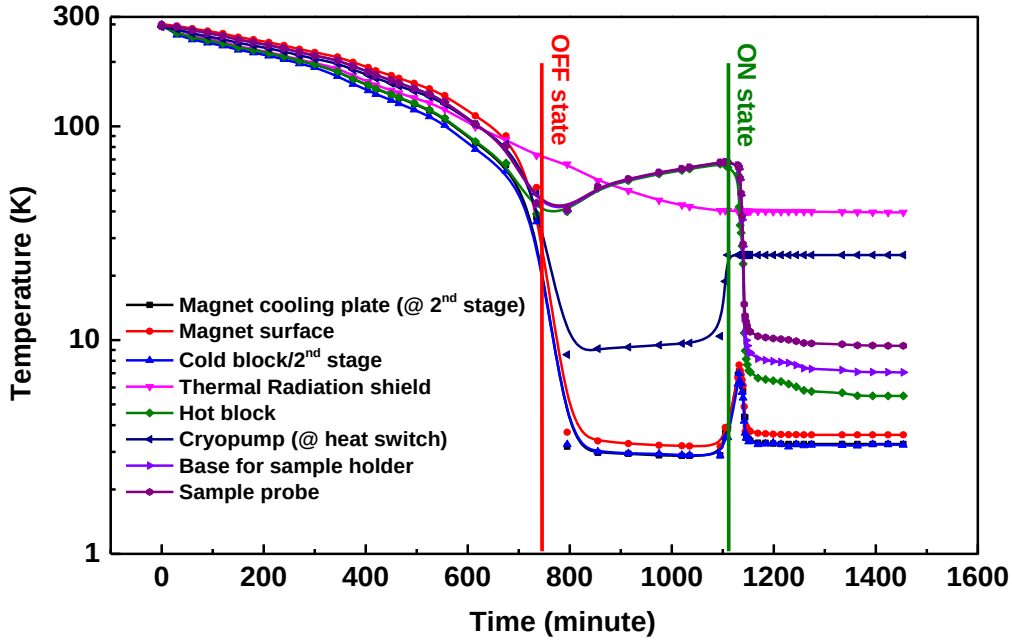

Figure 6.8. The cool down curve for CFMS with ON and OFF state of GGHS.

The 6T superconducting magnet system is cooled down from room temperature (300K) to the 3.2K magnet temperature in 16 hours. The steady state temperatures of the 2nd stage of the CCR is 2.9K and the thermal radiation shield is 39K, as shown in Figure 6.8. It also shows that when the cryopump temperature reaches below 25K then heat switch goes to OFF state that means the hot block and rest of the components after the hot block, like sample base and sample probe are thermally detached to the cold block. After the disconnection, hot block, sample base and sample probe temperatures rise and slowly reach to the steady state temperature in the range of 60-70 K whereas the cryopump temperature remains steady at 8K. The rising pattern of the hot block temperature happens due to the thermal load coming from the sample probe tube which has its one end at room temperature. To make the switch ON, the temperature of the switch is raised to 25K by applying heat to the cryopump. Cryopump then release the helium gas inside the annular space of the switch which eventually makes the switch conducting between cold block and hot block. Once the switch starts conducting, the temperature of hot block, sample base and sample probe start decreasing, as shown in Figure 6.8. When cryopump is powered to raise its temperature to make switch ON, the temperature of the NbTi magnet also initially rises up to 7K and then reaches to steady state at 3.58K. The temperature of the sample probe reaches to 9.6 K after four and half hour. The steady state temperature of the sample probe is higher than the expected temperature which is 4.5K. At the same time the steady state temperature of the hot block is about 5.9K and the sample base temperature is about 7.4K. Hence, there is a temperature drop of 1.5K between hot block and the sample base. Similarly there is a temperature drop of 2.2 K between sample base and sample probe. The temperature difference in between hot block and sample base is due to the poor thermal conduction through the copper braids or due to heat load comes from the sample probe tube. The temperature difference in sample probe and the sample base is because of the poor thermal

contact between two surfaces which is due to surface irregularities. This poor thermal contact causes the thermal contact resistance which reduces the conduction and generates the temperature difference. The parasitic heat load like conduction heat, radiation heat to the sample probe needs to minimize to reduce its steady state temperature.

The steady state temperature of the 2nd stage of CCR is 3.22 K which is 0.32K higher than the steady state temperature (2.9K) of 2nd stage achieved prior to the installation of GGHS. Similarly, the steady state magnet temperature (3.58K) is 0.4K higher than the steady state temperature (3.18K) of the magnet prior to the installation of GGHS. Hence it is concluded that the conduction heat flow through the sample probe and the radiation heat flow on the sample base give excess heat load to the 2nd stage which eventually raise the temperature of the magnet.

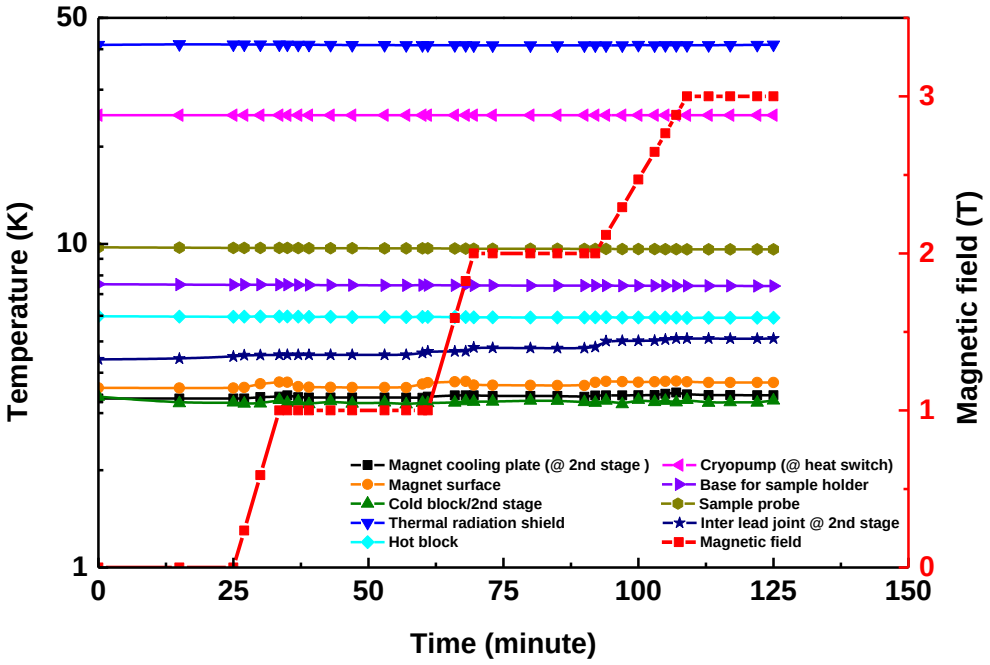

Figure 6.9. Temperature profile of different above mentioned parts during magnetic field variation when gas gap heat switch is in ON state.

At On state, when the temperatures of all the components reach to the steady state the magnet is started energizing. The magnet is energized up to 3T in steps of 1T. Figure 6.9 shows the dynamic thermal profile of the different components during magnet energizing with 2A/min sweep rate. The superconducting magnet achieves its 1T magnetic field in 8.30 minutes. Figure 6.9 shows that the temperature of magnet initially rises as long as the charging of the magnet going on. The magnet reaches to the steady state temperature when charging is stopped at certain magnetic field. During energization up to 1T, the temperature of the magnet reaches to maximum temperature of 3.74K before reaching to the steady state value of 3.6K as shown in Figure 6.9. The corresponding steady state temperatures of the magnet at 2 T and 3T field are 3.65K and 3.73 K respectively. There was no significant change in steady state temperatures of the 2nd stage cold head up to 3T field. During the magnet charging inter-lead joint temperature at the 2nd stage also increases which shows the higher joule heating loads through the current leads. This temperature rising pattern of the magnet and inter-lead joint, during the

ON state of the heat switch indicates that if magnet will charge further to achieve its designed peak field then probably magnet will cross its current sharing temperature and will finally quench.

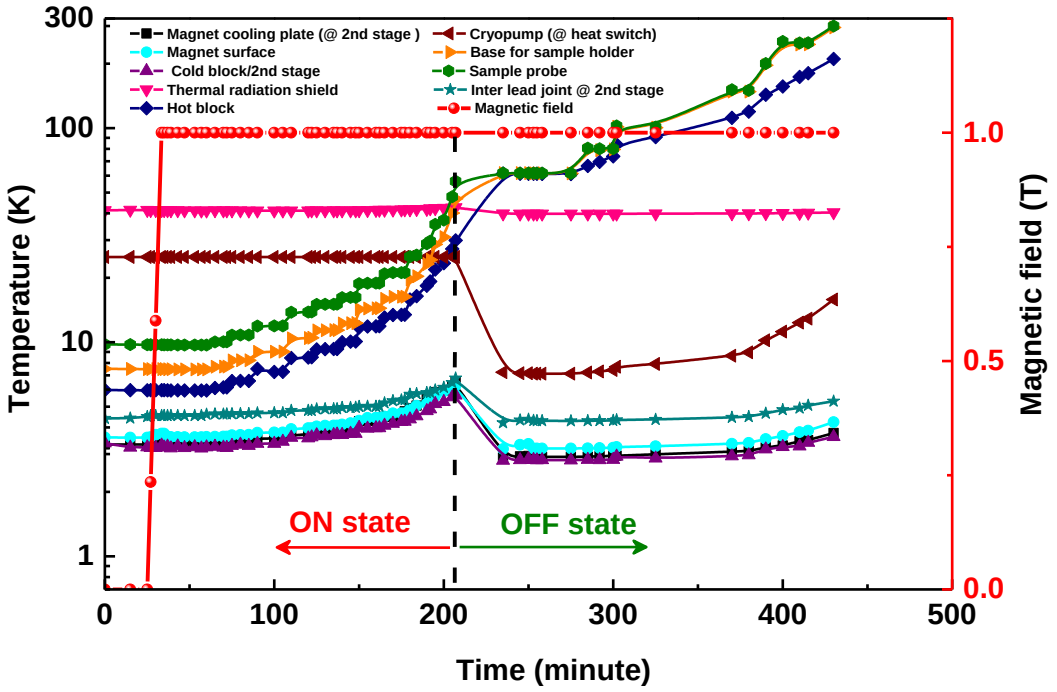

Figure 6.10. Sample space temperature variation up to 300K at 1T magnetic field.

Figure 6.10 shows the temperature profile of the sample probe from 9.6K to 300K at 1T magnetic field. In this experimental run heat switch is in ON state when temperature of the sample probe is 9.6K. Magnet is ramped with 2A/min to reach 1T magnetic field. Once the 1T field is reached, the temperature of the sample probe is raised using Lakeshore Temperature controller. The sample probe temperature is raised up to 60K, when switch is in ON state. The corresponding temperatures of other components are also rising slowly, as shown in Figure 6.10. When the sample probe temperature is 60K, the temperatures of 2nd stage/cold block and magnet surface are 5.64K and 6.06K respectively. After reaching the temperature of sample probe at 60K, put the heat switch at OFF state by cut off the power supply to the resistor of the cryopump. Once the GGHS is reached its OFF state, the temperatures of the 2nd stage/cold block and magnet surface start decreasing and get stabilize nearby at 2.9K and 3.18K respectively, as shown in Figure 6.10. At OFF state, the temperature of the sample probe has been raised up to 300K by using Lakeshore temperature controller. When the temperature of the sample space is 300K, the temperatures of 2nd stage/cold block, and magnet surface are 3.76K and 4.23K respectively. This temperature rising pattern is not desired because if the system will follow similar trend then at higher magnetic field, most probably the magnet will quench [11, 13, 67, 68].

After testing the heat switch at 1T magnetic field with 9.6K to 300K temperature variation, this experiment is stopped for further improvement in reduction of the thermal loads over the system. We did not vary the sample probe temperature up to 300 K at higher than 1T

magnetic field. We planned to reduce the parasitic heat flow to the GGHS and sample base to achieve lower steady state temperature. We also planned to improve the thermal contact between the 2nd stage cold head and GGHS, hot block of GGHS and the sample base. After warming up the cryostat, few layers of multi-layer insulation has been wrapped on the GGHS, thermal links and sample base to reduce the radiation heat flow. Thermal anchoring has been provided on the sample probe tube. After cool down of the system once the heat switch is gone to its OFF state then rest of the system after hot block, cut off with cold block and for reaching the temperature of the sample probe around 4.5K, when heat switch is set to ON state by setting the cryopump temperature at 25K, unfortunately heat switch is not set to ON state. The most probable reason behind this is the leakage of the inert helium gas from the heat switch. Probably this leakage is occurred due to mechanical or thermal stresses over the heat switch. Refilling of the helium gas in the GGHS is under process.

7.

CONCLUSION

Conclusion

The design of the 6T NbTi solenoid magnet has been discussed. This two stage GM cryocooler based conduction cooled magnet is able to generate 6T magnetic field in 10 mm DSV with 0.07% field homogeneity when it operates at 102A (68% of $I_c = 151$A) operating current. The NbTi magnet operates at 3.2K temperature range with 4.3K current sharing temperature with 1.1K of temperature margin. The cool-down time for the NbTi from ambient to the 4K is 14 hrs but the thermal shield takes 18 hrs to reach the equilibrium temperature of 39K. The cool-down time for the thermal shield can be reduced by optimizing its thermal mass. The cool-down time of the copper shield might be reduced by using Aluminium thermal shield. The steady state temperature of the magnet is 3.9K at 6T field whereas the temperature of the 2nd stage is 3.12K. The temperature drop between the magnet and the 2nd stage of the cryocooler can be minimized by improving thermal contact between them.

The optimization of the conduction cooled current lead has been provided shape parameter value for the different materials up to 4K temperature range. The thermal contact resistance is measured for inter-lead joint with Kapton and Aluminium nitride (AlN). The experimental results shows that Cu-Kapton-Cu interface has lower thermal contact resistance at 4K joint than that of Cu-AlN-Cu interface. But the Cu-AlN-Cu shows better performance than the Cu-Kapton-Cu at temperature higher than 40K. Hence it can be concluded that the inter-lead joint at the 1st stage (30K-60K) can be made using AIN whereas at 4K, inter-lead joints should be made of Kapton. Thermal contact resistance is found to be greatly dependent on contact surface area of the inter-lead joint. It decreases with the increment of contact surface area. The heat load simulation results are discussed for optimized phosphor de-oxidized copper current lead. The results shows that due to low thermal conductivity, alloys generate lower heat load and require lesser length as compare to pure metals.

The quench simulation results show that the small quantity of heat flux can initiate the quench. Different simulation case studies have been done with *QUENCH* program (OPERA) with the use of different quench protection circuit, which will help further for the improvement in quench protection circuit design. In experimental quench thermal profile the maximum temperature of the magnet is 54K whereas in simulation results it is around 75K, which indicates that quench protection circuit is well designed, working properly and quench didn't cause severe effect to the system. The designed operating current is decayed with in one second time period during quench, as shown in result graphs because of the value of the time constant is nearby one second.

The variable temperature insert has been developed and tested with the use of helium gas gap heat switch. This gas gap heat switch provides thermal coupling between sample space and 4K stage of GM cryocooler and allow to protect the magnet from overheating coming through the heater of the insert. The minimum sample space temperature has been reached around 9K. The sample space temperature can be reduced by minimizing the parasitic heat load to the sample space.

References-

[1] Hoenig M, "*Design concepts for a mechanically refrigerated 13 K superconducting magnet system*", Magnetics, IEEE Transactions on, vol. 19, issue 3, pp. 880-883, 1983.

[2] Bednorz J. G, and Müller K A, "*Possible high Tc superconductivity in the Ba−La−Cu−O system*", Zeitschrift für Physik B Condensed Matter, vol. 64, Issue 2, pp 189-193, 1986.

[3] Maeda H, Tanaka Y, Fukutomi M and Asano T, "*A new high-T(c) oxide superconductor without a rare earth element*", Japanese Journal of Applied Physics, Part 2 (ISSN 0021-4922), vol. 27, 1988, p. L209, L210.

[4] K Watanabe *et al*, "*Liquid helium-free superconducting magnets and their applications*", Cryogenics, 1994, vol.34, ICEC supplement.

[5] Yokoyama S, Minato T, Imai Y and Inaguchi T, "*Cryogen free conduction cooled NbTi superconducting magnet for a X-band klystron*", Magnetics, IEEE Transactions on, vol. 32, issue 4, pp. 2633 – 2636, 1996.

[6] Watazawa K, Sakuraba J, Hata F and Hasebe T, "*A cryocooler cooled 6 T NbTi superconducting magnet with room temperature bore of 220 mm*", Magnetics, IEEE Transactions on vol. 32, Issue 4, pp. 2594 – 2597, 1996.

[7] K Watanabe et al, "*11 T liquid helium-free superconducting magnet*", Cryogenics, 1996, 36(12), pp. 1019-1025.

[8] Song N H et al, "*A cryocooler directly cooled niobium titanium superconducting magnet system*", Advances in Cryogenic Engineering, vol. 45, pp. 667-674.

[9] Watanabe K, Awaji S, Takahashi K and Nishijima G, "*Construction of the cryogen-free 23 T hybrid magnet*", Applied Superconductivity, IEEE Transactions on vol. 12, Issue 1, pp. 678 – 681, 2002.

[10] Y Dai, L Yan, B Zhao and S Song, "*Tests on a 6 T Conduction-Cooled Superconducting Magnet*", Applied Superconductivity, IEEE Transactions on vol. 16, Issue 2, pp. 961 – 964, 2006.

[11] A.B. Berryhill, D.M. Coffey, R.W. McGhee and E.E. Burkhardt, "*Novel integration of a 6T cryogen-free magneto-optical system with a variable temperature sample using a single cryocooler*", AIP Conference Proceedings. 2008; 985:1523-1528.

[12] Y Dai, Q Wang, H Wang and B Zhao, "*An 8 T Superconducting Split Magnet System with Large Crossing Warm Bore*", Applied Superconductivity, IEEE Transactions on vol. 20 Issue 3, pp. 608 – 611, 2010.

[13] E Demikhov, E Kostrov, V Lysenko, N Piskunov, V Troitskiy, "*8 T Cryogen Free Magnet with Variable Temperature Space*", 9th European Conference on Applied Superconductivity (EUCAS 09), Journal of Physics: Conference Series 234 (2010) 032031.

[14] K Watanabe et al, "*Upgrade design to a cryogen-free 20T superconducting outsert for a 47T hybrid magnet*", Superconductivity, IEEE Transactions on, vol. 23, 3, 2013.

[15] Kar S, Konduru P, Kumar R, Kumar M, Choudhury A, Sharma R. G, and Datta T. S, *"Experimental studies on thermal behavior of 6 Tesla cryogen-free superconducting magnet system",* Advances in Cryogenic Engineering, vol. 57A, 2012, pp.909-917.

[16] "*Chapter 3, Magnetostatics*", http://physics.usask.ca/~hirose/p812/notes/Ch3.pdf.

[17] Iwasa Y. *"Case studies in superconducting magnets",* Plenum Press, New York and London, 1994.

[18] Wilson Martin N., *"Superconducting Magnets",* Clarendon Press. Oxford; 1983.

[19] Agatsuma K, "*Basic design of solenoid superconducting magnet for hands on training*", Physics and engineering of high-performance electron storage rings and application of superconducting technology. Proceedings, Asian Accelerator School, AAS'99, China, p.486-494.

[20] Boom R.W and Livingston R.S, "*Superconducting Solenoids*", proceeding of the IRE, pp 274-285, 1963.

[21] Sharma R.G., *Superconductivity Basics and Applications to Magnets*", Springer, 2015.

[22] Ten Kate H.H.J., "*Practical superconductors*," Proceedings CAS, CERN-89-04, pp. 252-270, 1989.

[23] Lubell M.S., "*Empirical scaling formulas for critical current and critical field for commercial NbTi,"* IEEE Transactions on Applied Magnetics, 19(1), pp. 754-757, 1983.

[24] "*NbTi superconducting wire"*, http://www.supercon-wire.com/content/nbti-superconducting-wires.

[25] "*SRDK- 415D GM cryocooler*", Sumitomo Heavy Industries Limited.

[26] Suman N, Soni V, Kar S, Choudhury A, Sarangi S K and Datta T S, "*Practical load map of two stage 1.5 W at 4.2 K (SRDK - 415D) GM cryocooler*", Presented at NSC-25, 2014.

[27] "*OPERA Electro Magnetic Simulation Software*", User guide book.

[28] https://uspas.fnal.gov/materials/04UW/Current_Leads.pdf, "*Current Lead Design -US Particle Accelerator School*".

[29] Wang Y. "*Fundamental Elements of Applied Superconductivity in Electrical Engineering"*, Wiley, 2013.

[30] http://www.cryogenics.nist.gov/MPropsMAY/OFHC%20Copper/OFHC_Copper_rev1.h

[31] www.nist.gov/data/PDFfiles/jpcrd123.pdf, "*Thermal Conductivity of Ten Selected Binary Alloy Systems".*

[32] www.nist.gov/data/PDFfiles/jpcrd221.pdf, "*Electrical Resistivity of Ten Selected Binary Alloy Systems".*

[33] www.nist.gov/data/PDFfiles/jpcrd155.pdf, "*Electrical Resistivity of Copper, Gold, Palladium, and Silver*".

[34] www.nist.gov/data/nsrds/NSRDS-NBS-8.pdf, *"NSRDS 8 Thermal Conductivity of Selected Materials".*

[35] http://www.can-superconductors.com/uploads/2/1/2/9/21298520/csl_datasheet.pdf.

[36] Tuttle J, Canavan E, and DiPirro M, *"Thermal and electrical conductivity measurements of CDA 510 phosphor bronze"*, NASA Goddard Space Flight Center, Maryland, USA http://ntrs.nasa.gov/archive/nasa/casi.ntrs.nasa.gov/20090032058.pdf.

[37] Mamford J.F., "*Superconducting current leads made from High-Tc superconductor and normal metal conductor"*, Cryogenics, 1989, 29(3): 206-207.

[38] McFee R., *"Optimum Input Leads for Cryogenic Apparatus. Review of Scientific Instruments"*, 1959, 30(2) 98-102.

[39] Hilal M.A, *"Optimization of current leads for superconducting systems"*, IEEE Transactions on Magnetics, 1977, MAG-13(1) 690-693.

[40] Kar S, Konduru P, Kumar R, Kumar M, Choudhury A, Sharma R G and Datta T S, *"Performance test and thermal analysis of conduction-cooled current leads at non-optimum operation",* Advances in Cryogenic Engineering, vol. 57A, 2012, pp.597-604.

[41] Chang Ho-Myung, Steven W. and Van Sciver, *"Thermodynamic optimization of conduction-cooled HTS current leads"*, Cryogenics, volume 38, 1998, Pages 729–736.

[42] Apiezon products, M & I materials ltd, N-grease (cryogenic application).

[43] Kar S, Konduru P, Sharma R.G, Datta T.S, *"Electro-thermal Behavior of the Joint of Binary Current Lead of Conduction-Cooled Magnet"*, Applied Superconductivity, IEEE Transactions on (vol. 23, Issue: 1), ISSN: 1051-8223.

[44] http://www.azom.com/article.aspx?ArticleID=610, Aluminium Nitride / Aluminum Nitride (AlN) - Properties and Applications.

[45] http://www.dupont.com.

[46] Lakeshore Cryotronics, Sensor model: DT-470, Sensor Type: Silicon Diode.

[47] 3M Technical Bulletin, *"Characteristics of thermal interface materials".*

[48] B. Schumann, F. Nitsche and G. Paasch, *"Thermal conductance of metal interfaces at low temperatures", Journal of Low Temperature Physics,* January 1980, Volume 38, Issue 1-2, pp 167-189.

[49] Y Xiao, H Sun, L Xu, H Feng and H Zhu, *"Thermal contact conductance between solid interfaces under low temperature and vacuum",* Review of Scientific Instruments, vol. 75, no. 9, 3074 (2004).

[50] J. Wang and H. Wang, *"Thermal contact conductance of ceramic AlN and oxygen-free high-conductivity copper interfaces under low temperature and vacuum for high temperature superconducting cryocooler cooling",* Review of scientific instruments, vol. 77. 2006. pp.024901-1-5.

[51] ANSYS, Finite element simulation software, ANSYS Inc.

[52] Stenvall A, "*Stability and Quench*", European Summer School on Superconductivity 2008, Pori, Finland, June, 2008.

[53] DEVRED A, "*Quench Origins"*, NATIONAL LABORATORY FOR HIGH ENERGY PHYSICS, KEK Report 89-25, March 1990.

[54] Bottura, "*Introduction to Accelerator Physics Superconducting Magnets*", CERN accelerator school, 2012.

[55] Weisend II J. G, "*Superconducting Magnets for Accelerators*", US Department of Energy Office of Science, National Science Foundation, Michigan State University.

[56] Maddock B J and James, G.B., proceedings of IEEE 115 (4), 543, (1968).

[57] Gilmore D.G, "*Spacecraft Thermal Control Handbook: Fundamental technologies*", 2002, ISBN: 1-884989-11-X.

[58] Kashani A, Helvensteijn B. P. M, McCormack F. J, and Spivak A. L, *"Helium Liquid and Gas-Gap Heat Switches for Applications at 2 K"*, Proc. of 1993 CEC, 39:1657 (1994).

[59] Lankford K, *"Thin Plate Heat Switches Development Performance and Applications"*, 10th Spacecraft Thermal Control Technology Workshop (March 1999).

[60] Frank D. J and Nast T. C, *"Getter-Activated Cryogenic Thermal Switch"*, Advances in Cryogenic Engineering, Vol. 31m, 1991 Cryogenic Engineering Conference (Cambridge, MA, 12-16 August 1985)(A87-50751 22-31). New York, Plenum Press, 1986, pp. 933-940.

[61] Jorge Andre Almeida Barreto, "*Gas gap heat switch for cryofree project*", Faculdade de Ciencias e teccnologia, Universidade Nova de Lisboa.

[62] Duband I, "*A Thermo-Mechanical Heat Switch*", Proceedings of the 15th International Cryocooler Conference, 2008.

[63] Catarino I, Bonfait G and Duband L, "*Neon gas-gap heat switch*", Cryogenics, 48, 2008, 17–25.

[64] Catarino I and Paine C, "*3 He gas gap heat switch*", Cryogenics 48 (2008) 17–25.

[65] Torre J. P and Chanin G, "*Heat switch for liquid-helium temperatures*", Service d'Aéronomie du CNRS, Verrières le Buisson, 91370 France, Review of Scientific Instruments 03/1984; DOI, 10.1063/1.1137726.

[66] J. Franco, D. Martins, I. Catarino, G. Bonfait, "*Sorption characterization and actuation of a gas-gap heat switch*" Sensors and Actuators A: Physical. 171 (2011): 324-331.

[67] Chandratilleke G. R, Ohtani Y, Hatakeyama H, Kuriyama T and Nakagome H, "*Gas-Gap Thermal Switch for Precooling of Cryocooler Cooled Superconducting Magnets*", Advances in Cryogenic Engineering, Vol. 41, pp.139-146,1996.

[68] B Zhao, Q Wang, L Li, H Liu, S Chen, Y Dai, Y Lei, H Wang, and Z Ni, "*Practical Application of Gas-Gap Thermal Switch in Conduction Cooled Superconducting Magnet System*", IEEE transaction on applied superconductivity, vol. 22, No. 3, 2012.